Making of Graphene Fibre Composites using Pressurised Gyration

A thesis submitted in partial fulfilment of the requirements for the degree of

Doctor of Philosophy

May 2019

By

Amalina Amir

Department of Mechanical Engineering

University College London

Torrington Place, London WC1E 7JE, UK

Declaration

I, Amalina Amir, confirm that work presented in this thesis is my own, where information has been derived from other sources, I confirm that this has been indicated.

Signature:

Date:

Impact Statement

In this work, a new method is introduced to produce graphene fibre composites that can be optimised for mass production. Many researchers have produced graphene fibres using electrospinning. However, this project utilizes pressurized gyration using polymer binder solution incorporation with sonicated graphene nanoparticle and graphene oxide.

Thermoplastic polyurethane (TPU) and phenolic resin (PR) were used to identify their processability of the mixture using pressurised gyration process. By changing the speed and pressure, the fibre showed different characteristics. Focused ion beam showed that the graphene nanoparticles were imbedded in the fibre and Raman spectroscopy supported the findings by showing the peak of D, G and 2D band.

The graphene nanoparticles with carbon precursor, polyacrylonitrile showed that some conductivity exists in the fibres by using multimeter.

The graphene oxide fibres were used in order to asses if the presence of oxide group gave impact on the fibre production. These showed that the GO-PAN gave better conductivity after pyrolysis, however less conductive than graphene nanoparticles fibre composite.

The melt compounding process improved the starting graphene nanoparticle and produced a more homogeneous solution to help promote dense packing of graphene particles in the fibres. However, some these fibres could not survive

through pyrolysis leaving the conductivity test incomplete. The conductivity of surviving fibre composites were very low after pyrolysis.

To conclude, the pressurised gyration system provides a new method for producing graphene fibre composites. To improve, more parameters can be explored like designing movable pots to produce tubular fibre, meshs and also tubular sheets from the pot wall. It is clear that the knowledge generated so far in the study of graphene-based fibre polymer nanocomposites offers a very valuable tool to facilitate advances valuable to the development of graphene-based smart applications.

ABSTRACT

This work is motivated by the goal to open up new markets and even replace existing technologies or materials using graphene as a disruptive technology. Only when graphene is used both as an improvement to existing material and in a transformational capacity, its true potential can be realised. Therefore, this project seeks to develop graphene fibres in order to utilise the advantages over carbon fibres for application in fibre-based devices including high strength, electrical and thermal conductivities, low cost, lightweight, and ease of functionalization.

A simple and effective process combining pressure and centrifugal spinning has been developed and used to produce composite fibres consisting of graphene nanoplatelets. Thermoplastic polyurethane, phenolic resin and polyvinylpyrrolidone polymers were used as matrices. Precursor of carbon, polyacrylonitrile and graphene oxide were used in combination to study the effect of performing graphene fibre after pyrolysis. Processing parameters such as rotation speed, pressure and polymer concentration had a marked influence on the composite fibre diameter. Focused ion beam milling and etching verified the effective incorporation of the graphene nanoplatelets in the composite fibres. Morphological, rheological, physicochemical and thermal properties of the composite fibres were evaluated to uncover possible applications areas of these products.

Publications and conferences

Journal publications

A. Amir, S. Mahalingam, X. Wu, H. Porwal, P. Colombo, M. J. Reece, M. Edirisinghe, Graphene nanoplatelets loaded Polyurethane and Phenolic Resin Fibres by combination of Pressure and Gyration, Composites Science and Technology, Volume 129, 6 June 2016, Pages 173–182

Xiaowen Wu*, Suntharavathanan Mahalingam*, Amalina Amir*, Harshit Porwal, Mike J. Reece, Valentina Naglieri, Paolo Colombo, and Mohan Edirisinghe, Novel Preparation, Microstructure, and Properties of Polyacrylonitrile-Based Carbon Nanofiber–Graphene Nanoplatelet Materials, ACS Omega, 2016, 1 (2), pp 202–211 DOI: 10.1021/acsomega.6b00063

*These authors made equal contributions

In preparation

Amalina Amir, Suntharavathanan Mahalingam, Harshit Porwal, Tongfei Wu, Biqiong Chen, Mohan Edirisinghe, Preparation and characterisation of melt compounded GNP-TPU nanofibres using pressurised gyration, in preparation.

Conference presentations

Amalina Amir, Prof. Mohan Edirisinghe, Dr. Suntharavathanan Mahalingam, Development of graphene fibre using pressurise gyration, UCL Mechanical

Engineering PhD Students Conference 2016, 31 May 2016, Oral Presentation and Poster

Amalina Amir, Prof. Mohan Edirisinghe, Dr. Suntharavathanan Mahalingam, Development of graphene fibre using pressurise gyration, Materials Science and Technology, Oral presentation, 14-15 Oct. 2018, Ohio, USA

Dedication

Keep your dreams alive. Understand to achieve anything requires faith and belief in yourself, vision, hard work, sacrifice, determination, and dedication. Remember all things are possible for those who believe.

Gail Devers

To

Insyirah, Imran, Ikmal

ACKNOWLEDGEMENTS

I would like to express my heartfelt gratitude, first of all to my supervisors, Professor Mohan Edirisinghe and Dr Suntharavathanan Mahalingam for their immense contribution toward my PhD programme, their supervision and guidance through using some equipment and procedures for my work and this is duly acknowledged.

My sincere appreciation also extends to my sponsor, Ministry of Higher Education (MOHE) Malaysia and Universiti Teknologi MARA (UiTM) Malaysia for funding this study.

Many thanks to Prof MJ Reece, Prof Paolo Colombo, Prof Biqiong Chen, Dr Harshit Porwal and Dr Xiaowen Wu for their help and inputs in making this study possible.

I am also grateful to my parents and parents in law: I owe them huge thanks not only for taking care of my children during my final year, but also for being wonderful grandparents, and for their constant and unwavering support, financially and emotionally.

Much love and enormous thanks to my children Insyirah, Imran and Ikmal who have been very supportive and a great source of encouragement and inspiration. They are the best in Shah Alam, London, and all points between and beyond. Thanks for tolerating my absence and occasional frustration especially during my final year, where we are apart continentally.

As for my husband Lufti, I find it difficult to express my appreciation because it is so boundless. He is my most enthusiastic cheerleader; he is my best friend; and he is an amazing husband and father. I am grateful to my husband not just because he has given up so much to make my study a priority in our lives, but because he has seen me through the ups and downs of the entire PhD process. He has shared this entire amazing journey with me.

All my colleagues, my friends and also staff in Mechanical Engineering Department, supported me in this work in diverse ways and I am grateful for their help. I would also like to extend my thanks to the technicians of the workshops under supervision of Mr Peter Kelly especially Mr Kee and Mr Kevin.

Ever more thanks go to the good friends I made, Ernie, Maryam, Anouska, Jennifer, Keith, Tala, Jubair, Phoebe, Abby, Dato Yunus Rais and fellow Malay sages, who keep this PhD journey pleasant and memorable.

Last but not least, I am very indebted to every individual that helped even with the smallest things throughout this journey. Throughout this PhD study, I was lucky enough to have met many people and gained new experiences. It is impossible to list each and every one that I owe a favour to. Nonetheless, I really appreciate whatever help I have received through it all. Thank you.

TABLE OF CONTENTS

List of Figures

List of Tables

Glossary of Abbreviations

GNP	Graphene nanoparticles
GO	Graphene oxide
rGO	Reduced graphene oxide
DC	Direct current
PAN	Polyacrylonitrile
TPU	Thermoplastic polyurethane
PR	Phenolics resin
DMF	N,N-Dimethylformamide
FTIR	Fourier-transform infrared spectroscopy
SEM	Scanning electron microscopy
TEM	Transmission electron microscopy
FIB	Focussed ion beam
CNT	Carbon nanotube
PANi	Polyaniline
PPy	Polypyrole
PMMA	Poly(methylmethacrylate)

Chapter 1 **Introduction**

1.1 Introduction and background

Modern soldiers carry lots of high technology equipment. That means they are carrying lots of heavy batteries too. Most modern devices run on lithium-ion batteries, which are bulky, inflexible and potentially dangerous if damaged. Extensive research has been carried out to develop supercapacitors that can sustain high power levels with long life cycles. Carbon nanofibres and carbon nanotubes have been grown on carbon fibres thermally at temperatures of 600 - 1000 ^{o}C using chemical vapor deposition (CVD) (Bello et al., 2015; Dong et al., 2011; Li et al., 2013). CVD is a volatile deposition method used to produce solid materials chemically at high temperatures in vacuum chambers. Although they improve the load transfer, shear strength, boost adhesion and electrical contact, growth of nanotubes and nanofibres at temperatures below 650 ^{o}C has scarcely been observed. Plasma enhanced CVD has improved the growth on substrates at temperatures of 120 ^{o}C. Further research has produced carbon nanofibres (CNFs) using electrospinning at room temperature followed by stabilization, carbonization processes thermally.

Electrospinning is a method used to produce nanofibres using an electrostatically repulsive force and an electric field between two electrodes, by applying high voltage to a polymer solution or a melt, so that it can make a web of nanofibres. Considering the high cost, long durations of spinning and low yield, a simple and effective process combining pressure and gyration producing nanofibres was introduced (Mahalingam & Edirisinghe, 2013). Pressurised

gyration is a promising fibre manufacturing method that can be used to overcome the limitations of conventional carbon fibres has risen from striking developments in the nanotechnology of carbon allotropes, particularly from the discovery of carbon nanotubes (CNT) in 1991 and more recently graphene.

Presently, pressurised gyration has shown great promise in forming nano- and micro-assemblies such as nanofibres, composite nanofibres, microbubbles and capsules (Mahalingam, Ren, & Edirisinghe, 2014; Mahalingam & Edirisinghe, 2013; Mahalingam et al., 2015a). This technique offers consistency, reliability and is easy-to scale up (Mahalingam et al., 2014; Mahalingam & Edirisinghe, 2013; Mahalingam et al., 2015b). In typical pressurised gyration using polymer solutions, the centrifugal force and the fluid flow overcomes the withholding surface tension force to initiate the instability in a liquid jet that subsequently breaks up into fibres. The evaporation of the solvent leads to solidification of the fibres formed (Mahalingam & Edirisinghe, 2013). The fibre size distribution and morphology are influenced by process parameters such as rotating speed, working pressure and the physical properties of polymer solution (Mahalingam & Edirisinghe, 2013). In addition, studies of polymer-protein solutions have shown that pressurised gyration is capable of generating microbubbles (Mahalingam et al., 2015a). In a typical parametric plot of rotating speed versus pressure of gyration it has been found that a minimum rotating speed and pressure are required to form a fibrous structure. Below this critical minimum rotating speed and pressure, fibres are not formed due to insufficient forces to initiate an instability (Mahalingam et al., 2015a). Moreover, there is also a

window of rotating speed and pressure required to form fibres and outside of this, microbubbles are produced.

The brilliant properties of graphene derive from the structure of single atom thick sheets of graphite that are self-assembled through Van der Waals forces and consist of sp^2 carbon lattices regarded as a 2D material with superior properties and negligible thickness (Wu et al., 2012). Two dimensional graphene (G) and graphene-based materials have attracted tremendous interest in the past decade owing to their superior surface area and exceptional physical properties such as mechanical strength, good electrical and electrochemical activity (Chen et al., 2013; He et al., 2013; Mattevi et al., 2009; Pàmies, 2014). Graphene is an excellent choice for super-capacitor electrode material, enabling high power density, high energy density and stable cyclic performance (Bose et al., 2012; Yu et al., 2014; Zhou et al., 2013). It has shown great promise in environmental remediation (Chandra & Kim, 2011). In addition, graphene can be an antibacterial material in bioengineering to prevent attachment and proliferation of microbes without the concerns of environmental pollution (Lu et al., 2012).

Graphene must be combined with polymers to form fibres. Manufacturing of graphene-based polymer composites involves finding a suitable blending method to reach a satisfactory dispersion of graphene throughout the polymer matrix. Generally, there are three methods to process graphene-based polymer composites, namely in-situ polymerisation, solution compounding and melt blending (Sengupta et al., 2011). In-situ polymerisation comprises the linking of a monomer and an oligomer in the presence of filler graphene, and

consequently, the in-situ compounding technique confers stronger interactions between the reinforcing graphene and the polymeric phase (Chen et al., 2001). This method exhibits better mechanical properties and lower percolation threshold, where the fibre start to form. However, it needs high electrical energy to disperse the graphene in the polymer matrix and may not be suitable for mass production of composites.

In solution compounding, the polymer is dissolved in a solvent and filler is dispersed in the resulting solution. After mixing, the solvent is removed and the bulk polymer containing the graphene is then used to give shape to the composite (Zheng, Wong, & Sue, 2002). It also has an advantage of lower percolation threshold than the in-situ polymerisation method. Percolation threshold is an important phenomenon for the polymer matrix composites which shows that at which minimum weight percentage of the filler (graphene) the conductivity of the polymer matrix composite increased. However, use of large amounts of solvent and their associated environmental pollution has prevented this method being used to mass produce polymer composites.

Melt blending involves melting of the matrix polymer after which graphene is mixed in with traditional mixing equipment such as an extruder, internal mixer and two-roll mill. It is a preferred industrial technique as it is a direct, cost-effective, and environmentally friendly process, since no solvent is involved (Chen et al., 2007). However, the percolation threshold values attained for this technique are higher than the in-situ polymerisation and solution compounding methods.

The use of graphene in this area, though, presents exciting new possibilities for energy store, with high charge and discharge rates and economical affordability. In conclusion, it should be noted that future work should not only include improved graphene fibres, but also needs to demonstrate how to improve the capacitance to storage energy at low cost.

In this work, thermoplastic polyurethane, phenolic resin and polyacrylonitrile with sonicated graphene and nanoplatelets were used to form hybrid polymer composites by pressurised gyration.

1.2 Aims

The aim of the present work is to identify the various conditions required for optimal production of graphene/graphene oxide-based fibre using different polymers and carbon precursors. The preliminary study of graphene fibres obtained from this project predetermines the fibres to be used in electrical and electronics applications. It begins with some rheological properties to determine the viscosity and surface properties to correlate with fibre production. High viscosity helps polymer solutions to incorporate the graphene nanoparticles into the fibre. Characterisation studies are performed using SEM analysis to investigate the shape of fibre and particle distribution. Raman spectroscopy is used for chemical structure and the identification of compounds using vibrational spectroscopy. Focus ion beam (FIB) milling is used to cut away structures on a surface to observe internal nanostructure of the fibre. Heat treatment is used to

stabilise and carbonise as well as burn out the polymer to promote densification and diffusion of graphene fibres left the structure as in Figure 1.1.

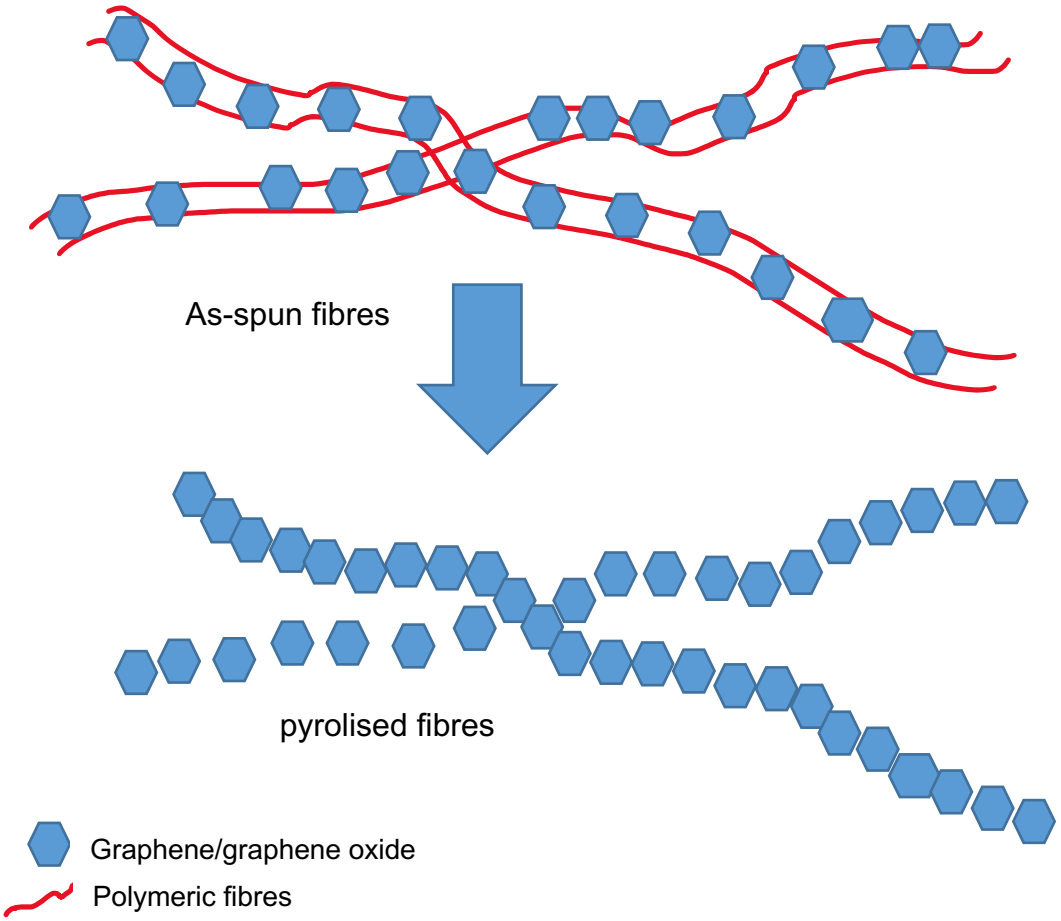

Figure 1.1 The aim of getting graphene fibres

1.3 Objectives

Objectives were set for this work in order to achieve the desired aims of this project.

1.3.1 Identification of suitable materials for nanofibre composites

Graphene fibres cannot be generated by themselves. Therefore, suitable polymer systems that work well with graphene were chosen. Some of the systems use carbon precursor to promote the graphene fibre formation.

1.3.2 Generating nanofibres from selected materials

A few parameters have been used to study the optimisation process which included the composition of graphene, polymer, speed of the motor, and also pressure. All the results were recorded.

1.3.3 Characterisation to identify physical attributes of fibres

After fibre processing and development, the fibre performance was studied. The diameter of the fibres were observed using SEM and the existence of graphene was confirmed by Raman spectroscopy. FIB was used to observe the graphene in cross section.

1.3.4 Investigating electrical properties of fibres

The electrical properties of the fibres were investigated using a multimeter.

1.3.5 Investigating the performance of pyrolyzed fibres

After the as-spun fibres underwent pyrolysis, the final product was tested again to observe the properties of the substance remaining after the sintering. SEM was used to study the dimensions after further processing.

1.4 Structure of thesis

This dissertation investigates the development of graphene fibres. This research intends to improve the understanding of the application of graphene fibres in composite materials. It is ordered in chapters covering different aspects of the research work being reported.

Chapter 1: An introduction providing a brief background on the concepts of pressurised gyration and how it may be adapted for producing material structures for optimal supercapacitors. The aim and objectives of this study are also set out in this chapter.

Chapter 2: Presents a general introduction to graphene fibres and other fibre processing methods. A literature review discusses how pressurised gyration works and the factors that affect outcomes from using this method. Materials used and rationale underlying their selection are also covered in this chapter. The motivation for the choice of the gyration process is discussed. Previous studies on production of fibres using methods such as electrospinning are also discussed. Types of polymers were described and the behavior of different characteristics explained.

Chapter 3: Specifications of materials, equipment and methods used in this work are stated here. The two types of polymers used in this study are described: thermoplastic polyurethane and phenolic resin. The first section of this chapter details the experimental setup for the preparation of polymer-graphene nanoparticle solutions. The solution is then poured into the pot of pressurised

gyration for different working conditions. The second part of this chapter explains the methodology for characterization of the fibres.

Chapter 4: This chapter contains results and discussions from work carried out so far, sectioned as graphene nanoparticle (GNP) characteristics and fibre morphologies of TPU/GNP and PR/GNP. In this work, TPU, PR and PVP polymers were used as matrices in the preliminary work to discover the potential of graphene fibre composite. Processing parameters such as rotational speed, pressure and polymer concentration had a marked influence on the composite fibre diameter. FIB milling and etching verified the effective incorporation of the graphene nanoplatelets in the composite fibres. Morphological, rheological, physico-chemical and thermal properties of the composite fibres were evaluated to assess suitability for these applications. Improvement of the process from work carried out using melt compounding of TPU/GNP is reported.

Chapter 5: This chapter contains results and discussions from work carried out so far, sectioned as GNP characteristics and fibre morphologies of carbon precursor polyacrylonitrile (PAN). PAN fibres containing various concentrations of graphene nanoplatelets (GNPs) have been prepared by pressurised gyration, and carbon nanofibres (CNFs) have been obtained after subsequent heat treatment and spark plasma sintering (SPS), removing polymer matrix. The influence of processing parameters such as rotational speed, working pressure, carbonization and SPS temperatures on the diameter of the nanofibres have been studied. Furthermore, the thermal properties, morphologies, and crystallization properties of the CNFs were investigated using thermogravimetry,

scanning and transmission electron microscopy, and Raman spectroscopy. Also, the electrical conductivity and mechanical properties of these samples were studied.

Chapter 6: This chapter contains results and discussions from work carried out so far, sectioned as graphene oxide (GO) characteristics and fibre morphologies of PAN. Therefore, this project also optimises the processing parameters using pressurised gyration in terms of composition, rotational speed, pressure and GO amount.

Chapter 7: This chapter is on conclusions and future work. Future studies will investigate PAN, as a precursor, ultimately for the elimination of solvents. Furthermore, graphene oxide with natural cellulose and conductive polymers materials will be investigated to find the best formula to produce the nanofibres. Finally, the processing and forming of the pressurised gyration device can be modified to obtain optimum characteristics. In conclusion, this work has demonstrated the possibility of generating future graphene fibre as potential constructs for developing superconductors.

Chapter 2 Literature review

2.1 Introduction

This literature review aims to put the research outcomes reported in this thesis in context by highlighting and exploring relevant theories and concepts within carbon fibres, specifically as applied to graphene fibre composites and their potential applications. This assessment expressed broadly expresses current methods employed to develop graphene fibres. The parameters that influence the structure, performance and properties of the fibres are also discussed.

Table 2.1 An overview of the main themes discussed in the literature review

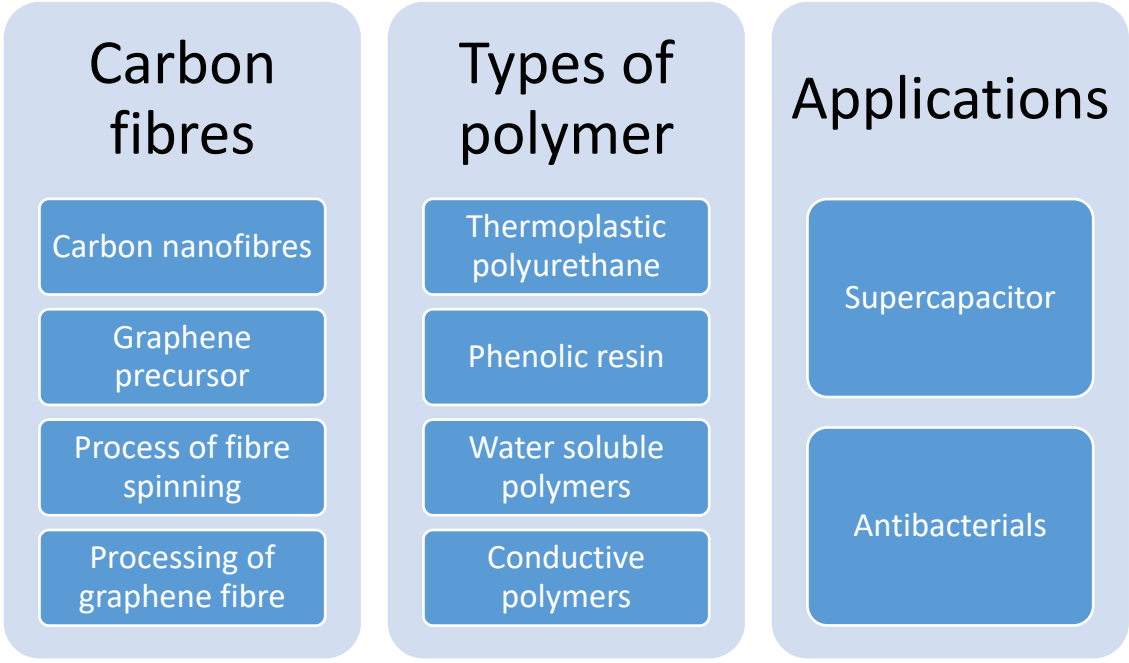

This research is a preliminary study to seek a simple way to develop graphene fibre at lower cost that can be utilised for conducting electricity or in electronics packaging. Therefore, the conductivity and structural analysis of the fibre has been explained briefly. Finally, suggestions for improving the techniques

especially through recent technology and processability demonstrated in this project have also been discussed. The organisation of this review is demonstrated in Table 2.1. The first is carbon fibres, and broad allotropes of carbon explained and the processing of fibres and carbon fibres that lead to this study. Next, the types of polymer that chosen in this study are discussed. The last part involves the potential applications of graphene fibres.

2.2 Carbon Fibres

Carbon or graphite fibres are produced from a variety of precursor materials such as rayon, polyacrylonitrile (PAN), and pitch. Although the term carbon fibre is often applied inter-changeably for both carbon and graphite fibres, technically, carbon fibres are pyrolyzed from their precursor substance at temperatures of 1100 - 1200 ^{o}C and consist of amorphous carbon networks (Mazumder, Chang, & Bond, 1982). In contrast, graphite fibres are produced by heating their precursor at temperatures of 2200 - 2700 ^{o}C, resulting in a crystalline fibre structure (Huang, 2009). Carbon nanofibres (CNF) are recognized as a very promising material in comparison to carbon fibres because of their nanostructure and superior properties. The nanofibrous structure naturally gives it a high surface area to volume ratio. This characteristic makes them very attractive in applications where a large surface area is desirable. CNF are used in many applications, such as electrical devices and sensors, electrode materials for lithium-ion batteries, microbial fuel cells and high-performance supercapacitors, catalysts or catalyst supports, and selective adsorption agents (Dai et al., 1995; Kim, Yang, & Ferraris, 2012; Manickam et al., 2013; Matsumoto et al., 1993;

Pham-Huu et al., 2000; Ramos et al., 2010; Rodriguez, 1993). CNF can also be described as stacked-cup carbon nanotubes (CNT). CNT are made by rolling up one or more layers of sheets of graphene into a cylinder. It is denoted as single-wall (SWNT) or multiwall (MWNT) with open or closed ends. CNT and graphene are two representative nanomaterials comprised of pure element carbon (Iijima, 1991; Novoselov et al., 2004). Graphene is the two-dimensional, hexagonal sp^2-carbon ring network with one atomic layer thickness. Figure 2.1 shows the schematic diagram of structures of graphene, SWCNT and MWCNT. Owing to their exceptional mechanical, electrical, optical and thermal properties, CNTs and graphene have been widely considered as new types of materials with great potential to revolutionalise many of the biological and medical fields (Yang et al., 2010; Yang et al., 2007).

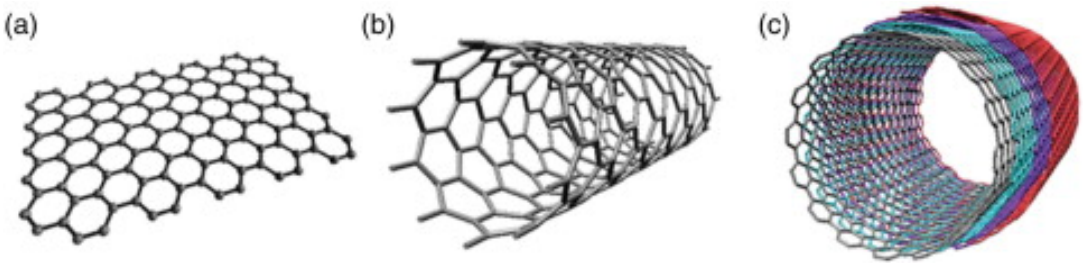

Figure 2.1 Schematic diagram of (a) graphene, (b) SWCNT and (c) MWCNT (Han et al., 2014)

2.3 Properties of graphene

The potential uses for graphene appear almost limitless. Graphene holds great promise for use in next-generation electronic and photonic devices due to its unique high carrier mobility, good optical transparency, large surface area, and biocompatibility (Gurunathan et al., 2012). Applications range from new types of

flexible electronics that could be worn on clothes or folded up into a pocket, to a new generation of very small computers and even hyper-efficient solar panels and super-fast mobile phones. The parent of all graphitic forms, it has emerged as a material of great interest due to its remarkable physical, chemical and electrical properties. It is 100 times stronger than steel by weight, yet incredibly lightweight and flexible. It is electrically and thermally conductive but also transparent. It is the world's first 2D material and is one million times smaller than the diameter of a single human hair. It was discovered in 2004 by Novoselov and Geim (Novoselov et al., 2004) and since then, labs around the world begun studies using graphene. One of the obstacles that needs to be overcome is how to make sheets of graphene large enough and pure enough, by containing just carbon and in one direction, to be useful.

Due to the strength of its carbon bonds, graphene is the strongest material ever discovered, with an ultimate tensile strength of 130,000,000,000 Pascals (or 130 gigapascals), compared to 400,000,000 for A36 structural steel, or 375,700,000 for Aramid (Kevlar). Not only is graphene extraordinarily strong, it is also very light at 0.77 mg^{-1} m^2 (for comparison purposes, 1 m^2 of paper is roughly 1000 times heavier). It is often said that a single sheet of graphene (being only 1 atom thick), sufficient in size enough to cover a whole football field, would weigh under 1 single gram.

Graphene is particularly special because it also contains elastic properties, being able to retain its initial size after strain. In 2007, Atomic force microscopic (AFM) tests were carried out on graphene sheets that were suspended over silicone

dioxide cavities. These tests showed that graphene sheets (with thicknesses of between 2 and 8 Nm) had spring constants in the region of 1-5 N/m and a Young's modulus (different to that of three-dimensional graphite) of 0.5 TPa (Frank et al., 2007). Again, these superlative figures are based on theoretical prospects using graphene that is unflawed containing no imperfections whatsoever and currently very expensive and difficult to artificially reproduce, though production techniques are steadily improving, ultimately reducing costs and complexity.

2.4 Graphene Precursors

Graphene precursors such as graphite sulphate and polyacrylonitrile (PAN), have enabled studies of graphene fibres. A precursor is a compound that participates in a chemical reaction that produces another compound, in this case, graphene. Graphite sulphate was used as a precursor by Eigler (Eigler, 2015) however, the functionality had not been proven with lower yields of graphene. Meanwhile, PAN, a form of acrylic fibre, is the predominant precursor material for the production of carbon fibres. The quality and composition of PAN precursors determine the ultimate performance of carbon fibres. A series of thermal treatments must be carried out to convert the PAN fibres to high tenacity carbon fibres, including thermal stabilization (~300 °C), carbonization (~1000 °C) and graphitization (>2000 °C) (Rahaman, Ismail, & Mustafa, 2007). The PAN fibres are first stretched and simultaneously oxidized in a temperature range of 200 - 300 ^{o}C. This treatment converts thermoplastic PAN to a non-plastic cyclic or ladder compound. After oxidation, the fibres are carbonized at about 1000 ^{o}C

in an inert atmosphere, which is usually nitrogen. Then, in order to improve the ordering and orientation of the crystallites in the direction of the fibre axis, the fibre must be heated at about 1500 - 3000 ^{o}C until the polymer contains 92-100% (Rahaman et al., 2007).

PAN is desirable as a carbon precursor because of its higher melting point and greater carbon yield compared with pitch and rayon, the natural precursors. Some of the key challenges using natural precursors which need further processing and purifying to form fibres, are that it is very expensive compared to PAN-based fibres (Chung, 2001). It has been established that PAN-based carbon fibres are stronger than other types of precursor-based carbon fibres (Cato & Edie, 2003).

There is great potential in using graphene oxide as a precursor as the chemical structure of carbon clusters, enabling better performance and combination to achieve a stable phase.

2.4.1 Properties of Graphene Oxide

One of the advantages of graphene oxide is its easy dispersibility in water and other organic solvents, as well as in different matrices, due to the presence of the oxygen functionalities. The structure consists of a single-layer of graphite oxide and is usually produced by the chemical treatment of graphite through oxidation. This remains as a very important property when mixing the material with ceramic or polymer matrixes when trying to improve their electrical and mechanical properties.

It is also worth noting that graphene oxide is often described as an electrical insulator, in terms of electrical conductivity, due to the disruption of its sp^2 bonding networks. The oxygenated groups in GO can strongly affect its electronic, mechanical, and electrochemical properties. Hence the difference with graphene nanoparticles. In order to recover the honeycomb hexagonal lattice, and with it the electrical conductivity, reduction of the graphene oxide has to be achieved (Mkhoyan et al., 2009). It has to be taken into account that once most of the oxygen groups are removed, the reduced graphene oxide obtained is more difficult to disperse due to its tendency to create aggregates. It tend to be unstable over time due to stacking interaction, and need sonification to disperse.

Functionalization of graphene oxide can fundamentally change graphene oxide's properties by modifying the oxygen functional groups of the structure surface. The resulting chemically modified graphene is then potentially much more adaptable for a lot of applications (Chen, Feng, & Li, 2012). There are many ways in which graphene oxide can be functionalized, depending on the desired application. For optoelectronics, biodevices or as a drug-delivery material, for example, it is possible that the structure bonded to oxygen is substituted with amines, carboxyl, hydroxyl or epoxy groups for the organic covalent functionalization of graphene, to increase the dispersibility of chemically modified graphene in organic solvents (Mkhoyan et al., 2009). It has also been proven that porphyrin-functionalized primary amines and fullerene-functionalized

secondary amines could be attached to graphene oxide platelets, ultimately increasing nonlinear optical performance (Dreyer et al., 2009).

In order for graphene oxide to be usable as an intermediary in the creation of monolayer or few-layer graphene sheets, it is important to develop an oxidization and reduction process that is able to separate individual carbon layers and then isolate them without modifying their structure. So far, while the chemical reduction of graphene oxide is currently seen as the most suitable method of mass production of graphene, it has been difficult to complete the task of producing graphene sheets of the same quality as through mechanical exfoliation, for example, but on a much larger scale. Once this issue is overcome, it is likely we will see graphene become much more widely used in commercial and industrial applications.

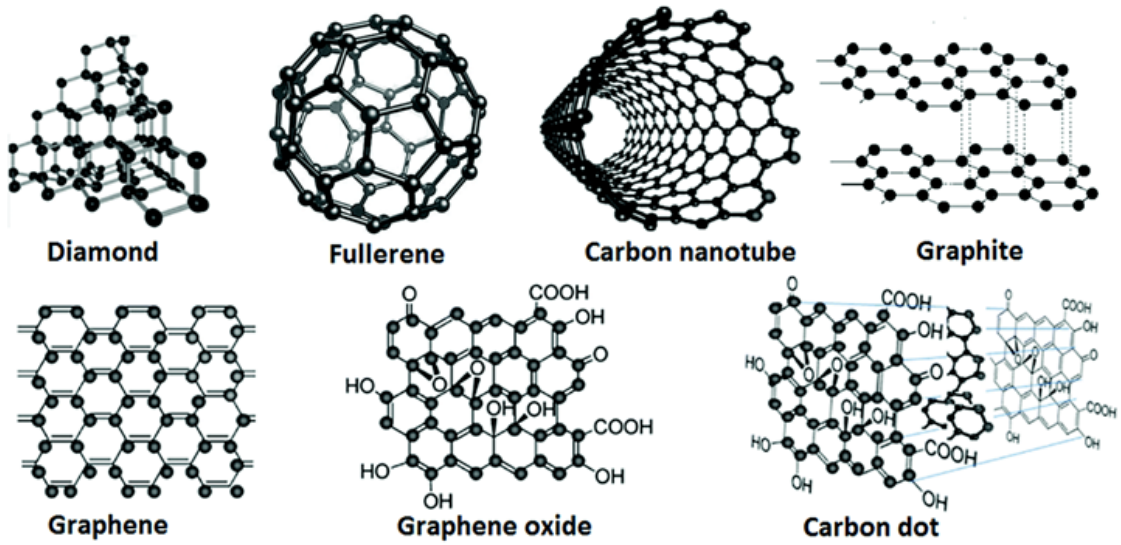

Figure 2.2 Various forms of carbon nanomaterials (Yan **et al.**, 2016)

Graphite is a 3-dimensional carbon-based material made up of millions of layers of graphene-graphite oxide is a little different. Through oxidation of graphite using strong oxidizing agents, oxygenated functionalities are introduced in the graphite structure which not only expand the layer separation, but also make the material hydrophilic (meaning it can be dispersed in water). This property enables the graphite oxide to be exfoliated in water using sonication, ultimately producing single or few layers graphene, known as graphene oxide (GO). The main difference between graphite oxide and graphene oxide is, thus, the number of layers.

While graphite oxide is a multilayer system in a graphene oxide dispersion, a few layers of flakes and monolayer flakes can be found. Synthesis of micron-sized partially oxidized graphene (POG) sheets improved electronic properties dramatically compared to other solution-phase exfoliated graphene (Eda et al., 2011). The electronic quality of reduced GO (rGO) is limited mainly by residual oxygen functional groups (Mattevi et al., 2009) and structural defects that originate from loss of carbon from the basal plane in the form of CO and CO_2 during reduction (Acik et al., 2011; Jung et al., 2009). Thus, efficient removal of oxygen and suppression of defect-forming mechanisms is crucial for achieving the highest electronic quality rGO.

The formation of stable defect species can be avoided in samples with lower initial oxygen content because isolated functional groups such as hydroxyls desorb directly, leaving the graphene basal plane intact. The basal plane is the plane perpendicular to the carbon in these crystal systems. When typical

oxidation processes such as the modified Hummers or Brodie's method are used, GO is fully oxidized with an oxygen content of ~30% (Eda et al., 2011).

Epoxy and hydroxyl functional groups are randomly distributed on both sides of the starting GO sheet, as shown in Figure 2.3. Graphene oxide (GO) is used as a starting material for the preparation of reduced graphene oxide (rGO). Using a thermal annealing process (thermal reduction), some of atoms are removed, resulting in nanopores formed in rGO materials with a variety of sizes. All structures are represented in ball and sticks form with carbon, oxygen and hydrogen atoms in grey, red and white colour, respectively (Lin & Grossman, 2015).

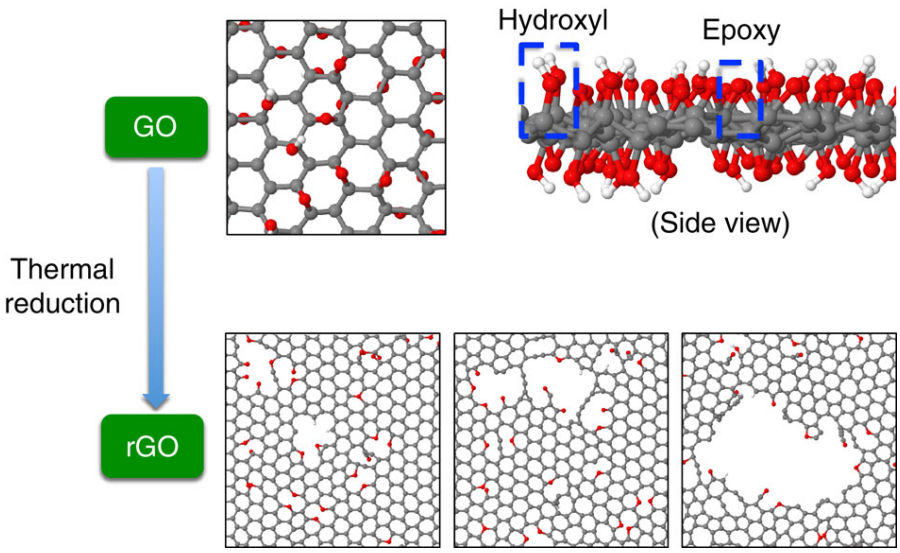

Figure 2.3 Schematic of the rGO formation (Lin & Grossman, 2015).

Figure 2.4 demonstrates further advances in catalytic performance from carbon-based catalysts potentially obtainable by varying the polarity, miscibility, and wetting properties of solvents, as well as by developing new aqueous-free

approaches (Martinez et al., 2016). GO is then subjected to different solvent-rinsing treatments which are chemically functionalized and exfoliated using potassium permanganate and sulfuric acid (modified Hummers method) to produce a GO powder with a d spacing of ~1 nm. Then vacuum drying is used to effectively remove unbound intercalated water as indicated by the decrease in d spacing (8.6 to 5.4 Å, depending on solvent used for rinsing). The resulting dried GO is doped with nitrogen (NH_3 at 850°C), leading to the formation of NrGO catalysts with a final natural graphite d spacing of 3.4 Å. (Martinez et al., 2016).

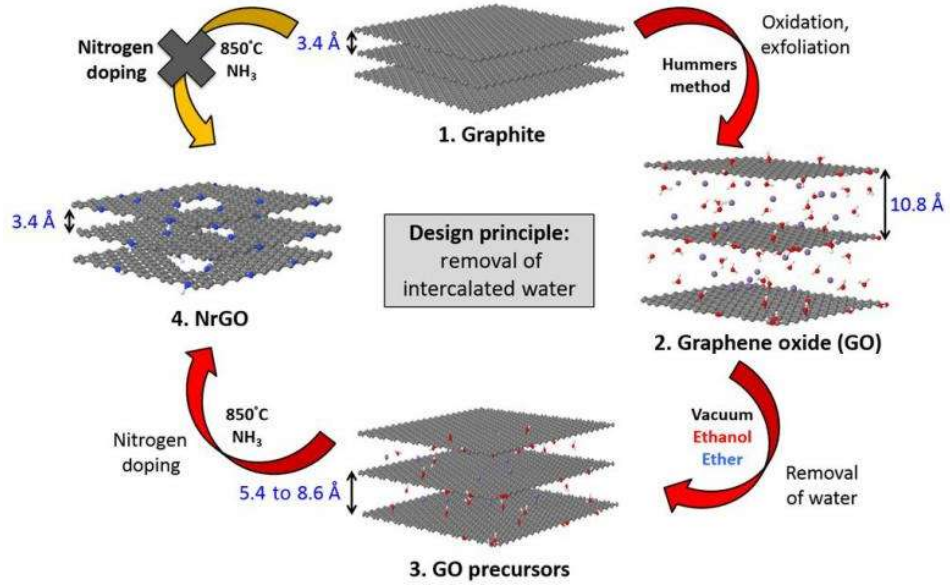

Figure 2.4 Schematic of the process developed to make NrGO catalysts. Atoms: C (gray), Mn from KMnO4 (purple), N (blue), O (red), and H (white) (Martinez et al., 2016).

The introduction of graphene-based smart materials in the market will depend fundamentally on the methodologies developed to incorporate graphene into the devices. In this respect, there has been much research directed toward the fabrication of graphene fibres (Meng et al., 2015; Xu & Gao, 2015), which exhibit very high-electrical conductivities, but have the drawback of poor and unreliable

mechanical performance. Thus, combination of graphene with the polymer fibres is an alternative approach to enhance mechanical strength, toughness and flexibility during use, and deformation.

The advance is part of a broader research effort to make GNP-embedded polymers. Carbon and glass fibres have traditionally been used to strengthen polymers– fiberglass is a common example (Patel, 2008). Unlike with fibres though, a very small amount of nanoparticles – less than 2 percent of the composite's volume–is enough to make the polymer stronger and heat resistant. Because less filler is used, the composite can retain the polymer's stretchability or transparency.

The key breakthrough needed to make the graphene-polymer composite was having the right kind of polymer for the potential applications. The researchers needed one or two layers of graphene with a few hydroxyl groups or oxygen atoms dangling in the solvents to help graphene link to the polymer and disperse evenly.

2.5 Types of polymer

Various polymers have been successfully produced into ultrafine fibres using electrospinning and other fibre production methods mostly in polymer solution and some in melt form. During electrospinning, polymer solutions systems that are subjected to a very high electrostatic force which causes the polymer solutions or melts to eject and spray or spiral rapidly from a nozzle or a spinneret and deposit randomly on an electrically grounded collector as fibres or fibrous

mats (Huang et al., 2003; Luo, Nangrejo, & Edirisinghe, 2010). When a polymer is highly soluble in a solvent, it will form strong polymer–solvent interactions where the polymer chains swell and expand to maximize the intermolecular interactions and when a polymer is less soluble the polymer chains contract and stay closer to each other to minimize the polymer–solvent interactions (Mahalingam et al., 2015a). Similarly, the same polymer systems were incorporated into pressurized gyration. Contrary to expectation, there is a significant difference in composition because the jetting out rate differs with these two processes. It was a challenge to find a suitable polymer system to carry out the process with graphene nanoparticle or nanofibre used in the solvent.

2.5.1 Thermoplastic Polyurethanes (TPU)

TPU is renowned for many things including its: high elongation and tensile strength; its elasticity and toughness; and to varying degrees, its ability to resist oil, grease, solvents, chemicals and abrasion resistance (Badamshina, Estrin, & Gafurova, 2013; Khudyakov, Zopf, & Turro, 2009). This versatile odourless polymer is soft and processable when heated, hard when cooled and capable of being reprocessed multiple times without losing structural integrity. It is used either as a malleable engineering plastic or as a replacement for hard rubber. The incorporation of CNFs into a thermoplastic matrix is receiving increased interest day by day due to manufacturing versatility and considerably improved strength and stiffness. The recyclability of thermoplastics gives them an added advantage because subsequent processing is to be used in this study (pelletizing, extrusion, and/or rheological evaluation). TPU is chosen since it is a

widely used thermoplastic polymer having good versatility in material properties. The broad technological exploitation of polymer nanocomposites is, however, limited due to the lack of effective methods to control nanofibre dispersion. Furthermore, to develop high performance polymer/CNF nanocomposites, a homogeneous dispersion of the fillers in the polymer matrix as well as a strong interfacial interaction between the polymer and the fillers must exist, so as to affect efficient stress transfer from the polymer matrix to the filler (Barick & Tripathy, 2010).

2.5.2 Phenolic resins

Recently, carbon-polymer composites made from the combination of graphite or carbon powder filler and polymeric resin have been investigated as a possible replacement for graphite and metal bipolar plates. The resin is a very dense, viscous substance with a characteristic smell and yellowish colour. These composites are expected to exhibit lower cost, higher flexibility, lighter weight and easier fabrication. The gas flow channels can be moulded directly into the plate, eliminating the requirement for a costly machining step. However, the polymer composites still have the problems of low electrical conductivity. Hence, an excessive amount of conducting filler has to be added into the composite to meet the minimum electrical conductivity requirement.

Unfortunately, high – conducting - filler loading substantially reduced the strength and ductility of the polymer composites (Chunhui, Mu, & Runzhang, 2008). Apparently, there is an urgent need for finding a polymer composite bipolar plate

which can provide high electrical conductivity and good mechanical properties. The motivation of using phenolic resin based on one-step carbonization is that it exhibits high microporosity (Suzuki et al., 2007), good dimensional stability and cost-savings free from activation can increase their application potentials. Porous carbon fibres show great potential in energy storage, gas adsorption and capacitive deionization, owing to their predominant mechanical strength, high specific surface area and developed pore structure (Mingxi et al., 2013). There is a critical minimum concentration of phenolic resin for the formation of bead-free fibres, meaning that when solution viscosity is too low the spinnability is reduced (in Section 4.3.3). In addition, adding electrolytes to the spinning solution can enhance the conductivity and electrostatic repulsion force on the surface of the jet and consequently reduce the diameter of phenolic resin fibres (Matsumoto et al., 2013). Different solvents can also affect the viscosity, conductivity and evaporation rate of the spinning solution (Bai, Huang, & Kang, 2013). However, no information about the preparation of GNP/PR, properties and adsorption performance of phenolic resin loaded graphene nanoplatelets fibre has yet been reported.

2.5.3 Water soluble polymers

Polyvinylpyrrolidone (PVP) is a linear homopolymer of N-vinylpyrrolidone (VP) that is soluble in water and a number of other polar solvents, and prior studies indicate that PVP has a propensity to coat graphite surfaces (Zhu et al., 2007). PVP is inexpensive, biocompatible, and has many applications in various fields such as pharmaceuticals, cosmetics, food, adhesives, polymers, and textiles

(Wang, Zhang, & Tian, 2012). PVP was used as polymer matrix, since it can easily form aqueous dispersion of polymer-coated graphite without worrying about the problem of the removal of organic solvents in solution compounding, and stabilize graphene oxide suspension without the need of surfactants because of its amphiphilic groups (hydrophobic methylene group and hydrophilic amide group).

2.5.4 Conductive Polymers

Conductive polymers have been studied extensively because of their potential applications in light emitting devices, batteries, electromagnetic shielding, anti-static and corrosion resistant coatings, and other functional applications. The supercapacitors have been made using highly conductive, lightweight polymers such as polyanilines (PANIs), polypyrroles (PPy), and polythiophenes (Frackowiak et.al, 2006; Jang, 2006). However, high power supercapacitors are a challenge to build using conducting polymers because they exhibit poor stability during the charge/discharge process. In recent times activated carbon and carbon nanotubes (CNTs), have been used to fabricate supercapacitors due to their good stability but these microstructures limit the value of the capacitance. A conducting polymer nanocomposite capacitor technology was developed using graphene–polyaniline (PANi) nanocomposite film, and could also surpass existing technologies (Gómez et al., 2011). The electrochemical capacitive properties of the rGO-conductive polymer composite materials showed superior performance (Zhang & Zhao, 2012). A very low

percolation threshold was achieved due to the formation of a two-dimensional conductive network (Pang et al., 2010).

2.5.5 Natural polymers

Cellulose fibres have broad applications to medical textiles owing to the “unique characteristics”, such as high moisture and liquids' adsorption, low impurity content, antistatic behaviour, and good mechanical properties. Due to their molecular structure and a large active surface area, cellulose fibres were considered as favourable materials for developing biomaterials because of their good bioactivity, biocompatibility, biodegradability, bioadhesivity, intelligent materials and antibacterial activity (Stashak, Farstvedt, & Othic, 2004). According to the literature, cellulose fibres are one of the most interesting basic materials for antimicrobial functionalization. Surface modification of cellulose fibres is currently considered to be the best route for obtaining modern functionality of textiles for use in medical applications (Yuan Gao & Cranston, 2008).

Despite various techniques used for fibre functionalization in order to impart antimicrobial properties and to develop biomedical products, there is still a large gap in knowledge of interactions between bacterial and fungal systems and bioactive surfaces of medical textile materials. Standard test methods are commonly applied to determine the efficiency of antimicrobial agents. These methods do not usually reflect in-use circumstances, because the majority of tests have only been performed in liquid media and not on dry, complex

heterogeneous systems such as functionalized fibrous materials. Testing and evaluating antimicrobial efficiency in laboratory conditions with respect to the real-life environment is rather challenging. Thus, the tests selected and interpretations made may vary on the basis of differences in antimicrobial action. The evaluation of any antimicrobial test results requires a thoughtful and basic understanding of microbiology, an understanding of the strengths and limitations of each test, and understanding the mode of action of the antimicrobial agent in question.

Chitosan has been extensively investigated for several decades for use in biosensors, separation membrane, artificial skin, bone substitutes, water treatment, and so on, because of its biocompatibility, biodegradability, multiple functional groups, as well as its solubility in aqueous medium (Fernandes et al., 2010; Liu et al., 2009). Despite numerous advantages and the unique properties of chitosan, its mechanical properties are not able to satisfy a wide range of applications. The formation of organic–inorganic hybrids through incorporation of fillers is an effective approach for improving physical and mechanical properties of chitosan. For example, hydroxyapatite (Cai et al., 2009), and carbon nanotubes (Liu, Chen, & Chang, 2009; Tang et al., 2008) have been used to reinforce chitosan. Yang et al. (2010) recently studied the nanocomposites of chitosan and graphene oxide (GO) in aqueous media (Yang et al., 2010). Porous scaffolds chitosan/graphene oxide (CHT/GO) biocomposites prepared by freeze-drying method are capable of mimicking the bone extracellular matrix and could have potential applications for bone tissue engineering (Pandele et al., 2015).

2.6 Process of Fibre Spinning

Several methods have been reported to prepare ordered graphene fibres, such as hydrothermal strategies and wet spinning of a concentrated graphene oxide (GO) liquid crystal solution.

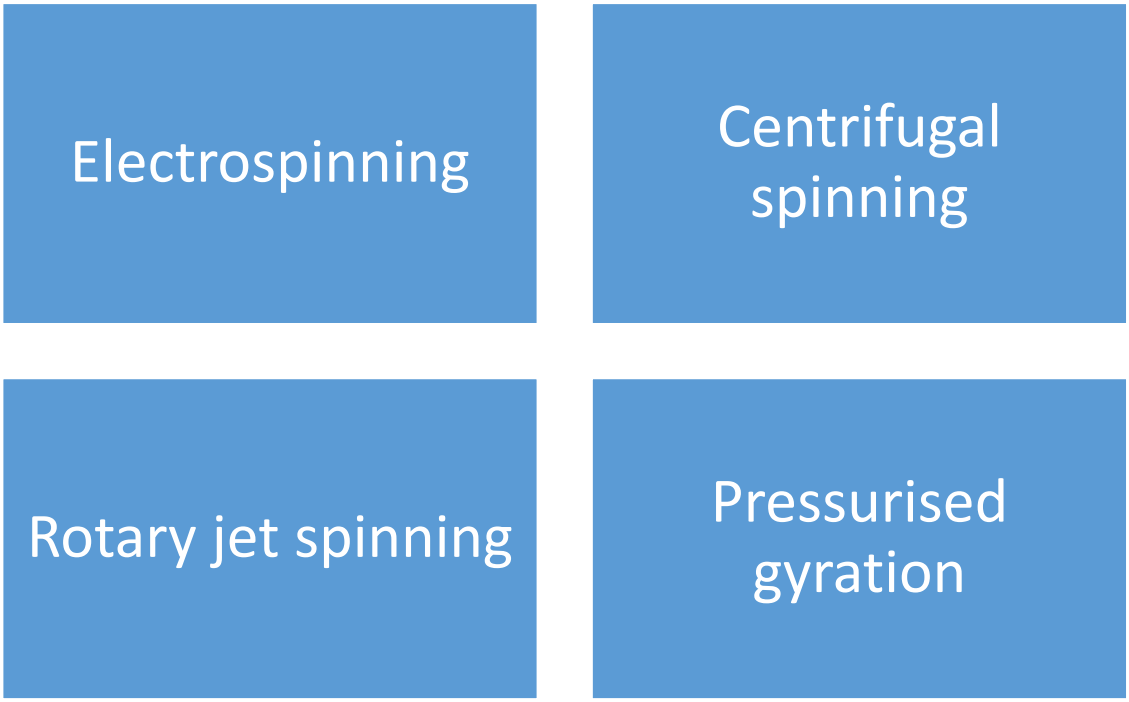

Figure 2.5 Fibre processing methods

2.6.1 Electrospinning

Electrospinning is a fibre spinning technique that produces polymer fibres of nanometre to micrometre size in diameter. Typically, a polymer solution or melt is placed into a container that has a millimetre size nozzle and is subjected to electric fields of several kilovolts, up to 40 kV. Under the applied electrostatic force, the polymer is ejected from the nozzle whose diameter is reduced

significantly as it is transported to and deposited on a template, which also serves as the ground for the electrical charge. Such thin fibres provide unexpected high surface area to volume ratios and are of interest for many applications ranging from textiles to composite reinforcement, sensors, biomaterials and membrane technology. In recent years, many different types of polymer fibres have been generated by electrospinning (Reneker et al., 2000). Nanofibres to date have largely been produced by fibre spinning, thermal controlled phase separation and bio-fabrication usually by molecular self-assembly (Luo et al., 2011). Fibre spinning, specifically electrospinning, appears to be the method mostly used in generating nanofibres (Zhou, Gong, & Porat, 2009).

2.6.2 Pressurised Gyration

A new solvent-based nanofabrication system, pressurized gyration, has recently been developed by Mahalingam and Edirisinghe (Mahalingam & Edirisinghe, 2013). The pressurized gyration process exploits both simultaneous centrifugal spinning (Badrossamay et al., 2010) and solution blowing (Medeiros et al., 2009) to generate uniform polymeric nanofibres. Since its invention in 2013, innovation of this process such as pressurised melt gyration, infusion gyration and pressure-coupled infusion gyration had evolved in Table 2.2.

Table 2.2 Chronology of work produced by pressurised gyration

Method	Materials	Outcomes	Author
Pressurised gyration	PEO water solutions	New fibre spinning technique	(Mahalingam & Edirisinghe, 2013)
Infusion gyration	PVA	Magnetic fibres	(Zhang et al., 2015)
Pressurised gyration	PMMA	Antimicrobial fibres	(Xu et al., 2015)
Pressurised gyration	PMMA	Nanopores fibres	(Illangakoon et al., 2016)
Pressurised gyration	PVA Lysozome	Generate microbubbles	(Mahalingam et al., 2015a)
Used fins as collectors	Shape memory polymer (PLLA-PMMA)	Aligned fibres and mats	(Wu et al., 2017)
Pressure driven spinning	PEO,PCL, PVA, PLLA	Direct fibre spinning using single needle	(Jayasinghe & Suter, 2010)
Solution blowing	Cellulose nanofibre	Coaxial structure fibre	(Zhuang et al., 2012)
Melt blowing	PBT, PS, PP	Produced fibre using single orifice melt blowing	(Ellison et al., 2007)
Pull spinning	PCL, PU, nylon, gelatin	Extruded a polymer droplet into a solid nanofiber	(Deravi et al., 2017)
Pressure coupled infusion gyration	PEO water solutions	Used squirrel cage to collect fibre	(Hong et al., 2017)

The pressurized gyration process comes from the rotary jet spinning method. The centrifugal force used as rotational shear force and solution blowing can accelerate the air velocity to extrude the polymer solutions via a narrow orifice. The Rayleigh-Taylor instability, (the balance force of the surface) on the jet caused by ejection of polymer solution can explain the pressurized gyration technique.

Equation 2.1 shows the destabilising gravitational force per unit volume to the stabilising surface tension force per unit volume equals the instability between the liquid-gas interfaces (Mahalingam & Edirisinghe, 2013; Weitz et al., 2008).

$$\rho g \frac{\partial h}{\partial x} = \gamma \frac{\partial^3 h}{\partial x^3} \qquad \text{Equation 2.1}$$

where, g is the gravitational force, ρ is the density of the polymer solution, γ is the liquid-gas surface tension, h is the height of the liquid drop hanging under the horizontal surface and x is the vertical distance.

According to Equation 2.1, during the spinning and gas blowing period, using the destabilising centrifugal force ($\rho\omega^2 R$), pressure difference (Δp), rotational speed (ω) and radius of the vessel (R), the characteristic length scale of the instability can be rewritten as Equation 2.2 (Mahalingam & Edirisinghe, 2013).

$$L = \left[\frac{\gamma}{(\rho\omega^2 R) + \Delta p}\right]^{1/2} \qquad \text{Equation 2.2}$$

Fibre production by pressurised gyration process is similar to the rotary jet-spinning process in that a jet occurs from the orifice and elongates as a result of the centrifugal force and the pressure difference at the orifice, and the solid fibre is finally formed with the evaporation of the polymer solution.

2.7 Fabrication of graphene fibres

Significant progress has been made in recent years in the development of graphene-based fibers. Graphene-based fibers with a 1D linear structure are flexible and weavable, suitable for producing multi-functional electronic textiles, and could be used in some difficult-to-reach locations such as in the case of sensing/surveillance. The development of high-performance graphene-based fibers could inspire more engineering applications of graphene. To date, some potential applications of graphene-based fibers have been demonstrated, including conducting wires, fiber-shaped energy-storage devices, and smart actuators, to name a few. Recently, significant efforts have been made on the promotion of graphene-based fibers from laboratory research to industrial applications (Meng et al., 2015).

The main methods used to produce graphene-based fibers are solution-spinning methods. This includes wet-spinning, dry-jet wet-spinning, and dry-spinning, differing on whether the spinning dope is coagulated in a solution bath or not and whether there is an air gap between the spinneret and the coagulation bath.

In wet-spinning, a GO dope is prepared by dispersing GO sheets into a stable water solution and then injecting them into a coagulation bath to form a gel-state fiber. After coagulation for a specific time, a GO fiber can be obtained by extracting the gel-state fiber and then drying (Pal et al., 2013; Weise et al., 2017; Zander, 2015). A reduced graphene oxide (rGO) fiber can be produced by further reducing the GO fiber when needed. To ensure the uniform and continuous

formation of a GO gel-state fiber, the as-coagulated fiber should be drawn at a constant speed either by rotating the bath or drawing the fiber using a collection unit (Xu et al., 2013). An air gap between the spinneret and the coagulation bath resulted in superior mechanical properties due to the drawing of the jet (Xiang et al., 2013). Liquid crystalline graphene oxide showed that spinning conditions that resulted in fibre defects show low stiffness and strength (Chen et al., 2013).

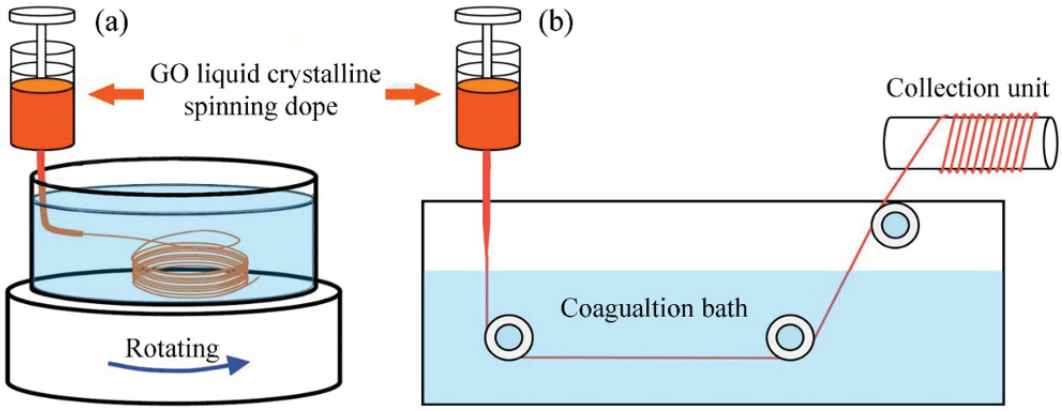

Figure 2.6 Wet-spinning set-up showing the as-synthesized fibres drawn by a rotating coagulation bath (Xu et al., 2013)

In the melt-spinning process, solid-state polymer is melted to the gel state for fiber-filament extrusion. Therefore, this method is suitable for spinning fibers from polymers that can be melted without obvious degradation, such as nylon and polyester.

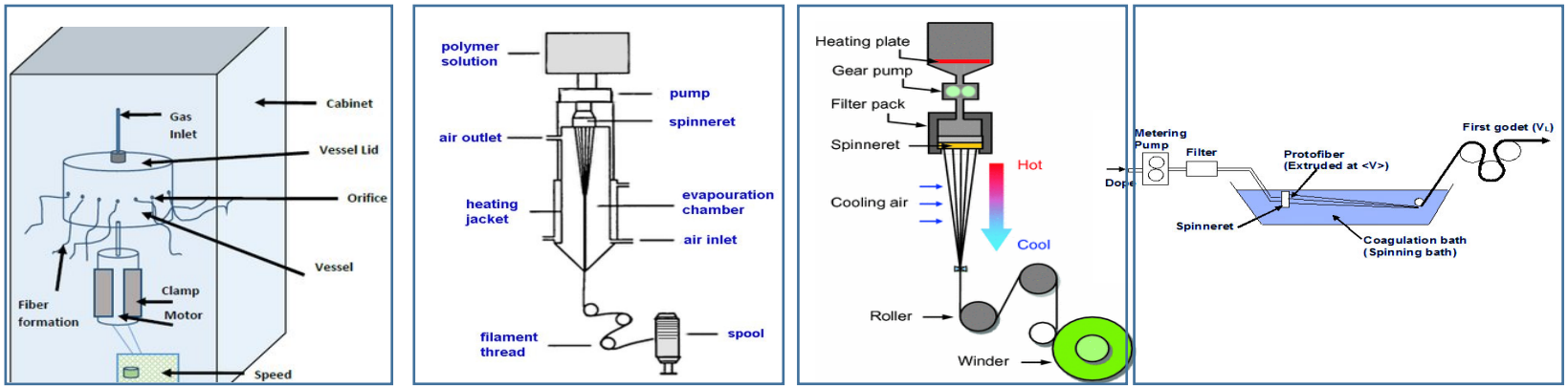

	Pressurised gyration	Dry spinning	Melt spinning	Wet spinning
Process				
Advantage	High yield, use pressure to control fibre diameter, versatile polymer	productivity of dry spin is much higher, no further purification	High speed, no purification, no solvents	Can handle large pulling of fibres
Disadvantage	Nanotube is not feasible, uniformity of particulate fibre	Flammable, slow production, need solvent recovery	Only for lower melting point polymer, separate drawing step	Low productivity, need purification

Figure 2.7 Comparison of fibre production processes

2.8 Applications

Graphene fibres possess many of the outstanding attributes of graphene, they should have many functionalities that can be used in a wide variety of functional applications. Apart from the important goal of upgrading the intrinsic properties of graphene fibres, considerable effort has been devoted to exploiting their functional uses in products, such as electrical conductors, supercapacitors, actuators and solar cells (Xu & Gao, 2015), all of which indicated the rich functionalities of graphene fibres that surpass those of conventional carbon fibres. Graphene fibres provide wide spectral range but require a cost-effective graphene-transferring technology. The combination of transparency, conductivity and elasticity will find use in flexible electronics, whereas transparency, impermeability and conductivity will find application in transparent protective coatings and barrier films; and the list of such combinations is continuously growing (Novoselov et al., 2012).

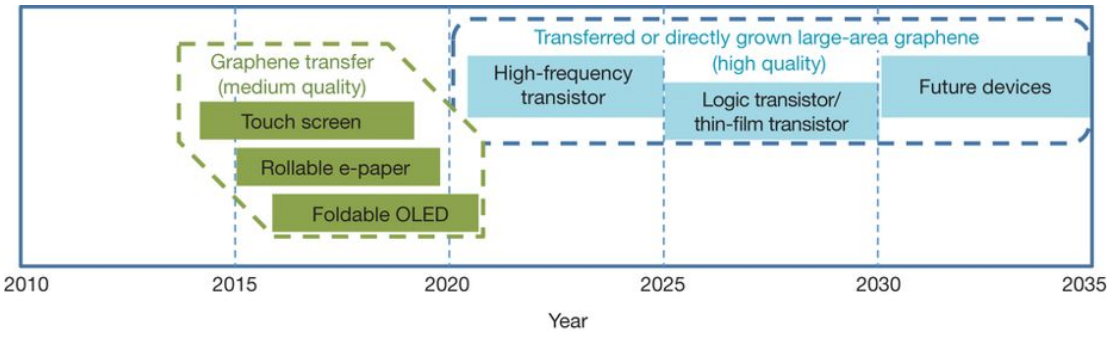

Figure 2.8 Graphene-based display and electronic devices (Novoselov et al., 2012)**.**

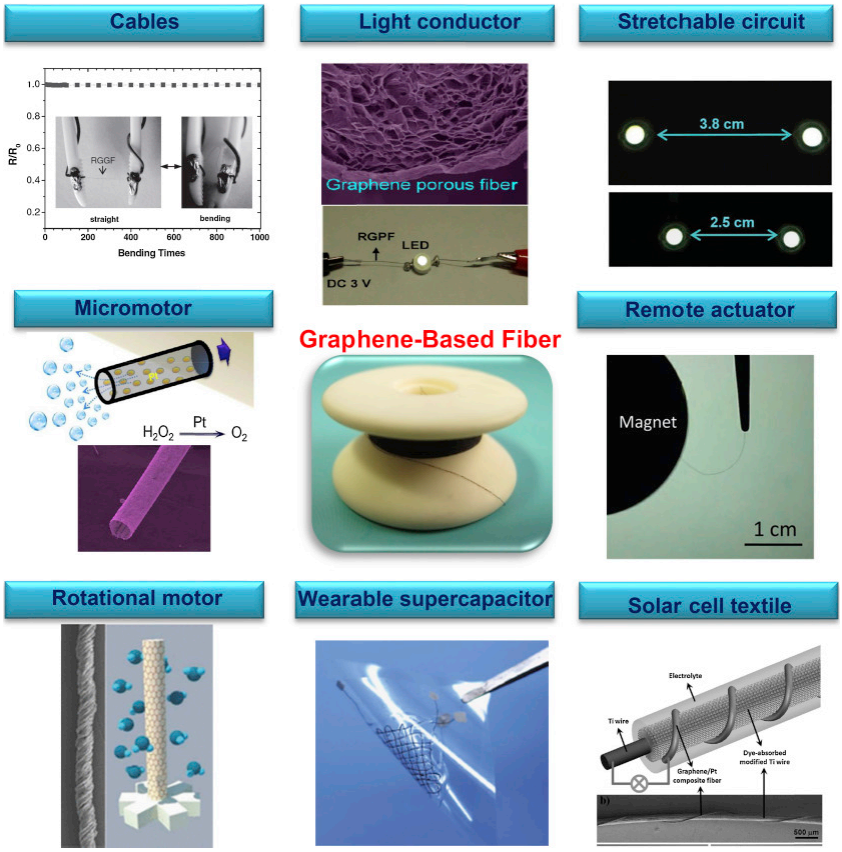

Figure 2.9 Functional applications of graphene fibres (Zhen Xu & Gao, 2015)

2.8.1 Antibacterial

It has been found that GO dispersion shows the highest antibacterial activity compared to rGO, graphite, and graphite oxide under the same dispersion concentration toward E. coli (Liu et al., 2011). Exposure to GO and rGO induced significant production of superoxide radical anion compared to control. GO and rGO showed dose-dependent antibacterial activity against P. aeruginosa cells through the generation of reactive oxygen species, leading to cell death, which was further confirmed through resulting nuclear fragmentation (Gurunathan et al., 2012). The effects of GNPs in PMMA fibres on the growth of E. coli and P. aeruginosa was showed that 8 wt% GNP fibres had antimicrobial activity. The

bacterial growth observed with lower GNP-concentration fibres may be attributed to GNPs serving as a nutrient source for microbial growth (Matharu et al., 2018).

2.8.2 Supercapacitors

A new generation of supercapacitors is expected to replace batteries in certain applications where high efficiency, high power, and a high level of reliability is required. High performance supercapacitors are promising candidates for future energy and power storage devices (Bose et al., 2012). Supercapacitors from graphene-wrapped PANi nanowires showed high capacity performance and good conductivity (Yu et al., 2014). The capacitive performance remains stable after charging and discharging, the thermal stability is improved and for long-term charge storage, GO is further electrochemically reduced into graphene and PPy is subsequently thermally carbonized. That value of capacitance was higher than that of conventional porous carbon materials while the reduced graphene oxide/carbon nanowires show a lower Faraday resistance and higher thermal stability than the GO/PPy nanowires (Chen et al., 2014). Faraday resistance is the interfacial resistance of capacitors.

2.8.3 Lightweight electrical conductors

Highly conductive lightweight graphene fibres are good candidates for wires and cables to carry heavy current. Another advantage of graphene fibres is their valuable flexibility; they can be twisted into tight knots without breaking, which is not possible for conventional carbon fibres. Chemical reduced graphene fibres

can be used as conductors to connect prototype devices and batteries (Zamora-Ledezma et al., 2012). Meanwhile, Ag-doping enhanced the electrical conductivity and only minimally affected the mechanical strength and flexibility of graphene fibres (Xiang et al., 2013). Through the “pre-stretching and buckling” strategy, flexible Ag-doped GFs were employed to construct stretchable circuits on rubber substrate, and the resistance remained invariable during 50 cycles of stretching-relaxation. The breakdown current density (ampacity) of this Ag-doped graphene fibres was 7.1×10^7 A/m^2, which should be greatly improved by further thermal annealing and graphitization for practical uses.

2.8.4 Smart actuators

Researchers from Beijing Institute of Technology established a series of smart actuators of graphene fibres, such as self-driven graphene fibres tubes, moisture actuators, torsional motors and magnetic-driven springs, by virtue of their structural design (Cheng et al., 2014, 2013; Pei & Cheng, 2012). They used lasers to reduce only one side of GO fibres and obtained graphene fibres with asymmetrically hydrophilic attributes. The remaining GO part was responsive to moisture and drove the whole graphene fibres to bend or curl reversibly (Cheng et al., 2013). For a torsional motor, they rotated GO gel fibres in the radial direction during the drying process and obtained GO fibres with helically twisted wrinkles on the surface. The twisted GO fibres are able to reversibly respond to moisture by rotation, behaving like a typical rotational motor (Cheng et al., 2014).

2.8.5 Composite materials

Currently, aerospace engineers are incorporating carbon fibres into the production of aircrafts as it is also very strong and light. However, graphene is much stronger whilst being also much lighter. Ultimately, it is expected that graphene is utilized (probably integrated into plastics such as epoxy) to create a material that can replace steel in the structure of aircraft, improving fuel efficiency, range and reducing weight. Due to its electrical conductivity, it could even be used to coat aircraft surface materials to prevent electrical damage resulting from lightning strikes (Jesus de La Fuente, 2013). In this example, the same graphene coating could also be used to measure strain rate, notifying the pilot of any changes in the stress levels that the aircraft wings are under. These characteristics can also help in the development of high strength applications such as body armour for military personnel and vehicles.

2.9 Graphene fibre processability using PG

Carbon fibres have excellent strength and are lightweight. These characteristics make it a viable, versatile, and useful commercial product for a wide variety of markets. Carbon fibres offer high surface area to volume ratio; and consist of cylindrical nanostructures with graphene layers arranged as stacked sheets or plates. Graphene has extraordinary mechanical properties, including high tensile strength, notable flexibility, extremely high electric conductivity, high thermal conductivity, and good stability against chemicals. Therefore, with increased strength and rich functionalities, graphene fibres have attracted a lot of

researchers to untiringly pursue its processability. Polyacrylonitrile (PAN) and pitch are the two dominant precursors for the production of carbon fibre. PAN-based carbon fibres are used for high tensile and compressive strength applications. Meanwhile, most graphene fibres are prepared from graphene oxide precursors due to their easy dispersibility in liquid, owing to the presence of the oxygen functionalities. Selecting suitable polymer materials and applying further mixing processes, properties conferred onto these nanostructures affected their electrical properties. This sums up the rationale for producing graphene fibres by pressurised gyration, which has good prospects of upscaling for yields to meet realistic demands. This approach in producing graphene fibres offer many parameters that may be adjusted to optimise the outcome of production. These include flexibility with the choice of material, solution properties, production conditions such as rotation speed, pressure and environmental factors e.g. room temperature and humidity.

Producing substantial quantities of graphene fibres with good electrical conductivity will be a positive addition to efforts in the supercapacitor industry. It is expected that outcomes from the work reported subsequently in this thesis will be a significant contribution to improving processability of graphene fibre.

Chapter 3 **Experimental details**

This chapter presents the details of the materials, equipment and experimental procedures of this study. With respect to materials used, a thorough description, rationale for selection as well as suppliers are given. For equipment, details of manufacturers or suppliers in addition to an overview of their operation and instrumental settings are set out in relevant sections discussing various procedures. The parameters analysed by this equipment and their objectives of this project are highlighted in this section.

3.1 Materials

In generating various kind of graphene fibres, several types of polymers have been used. Further details of the polymers are given in later subchapters. Various parameters were investigated to find the best composition of the graphene fibres.

3.1.1 Thermoplastic polyurethane (TPU)

Thermoplastic polyurethane (TPU) was purchased from Covestro under the brand of Desmopan DP 9855DU, which consist of linear segmented block copolymers composed of hard and soft segments in Figure 3.1. TPU is known under different trade names for commercial of major manufacturers. It is a thermoplastic elastomer with high durability and flexibility. Therefore, it is very in demand because of the outstanding properties between the characteristics of plastic and rubber and contributes to excellent tensile strength, high elongation at break, and good load bearing capacity.

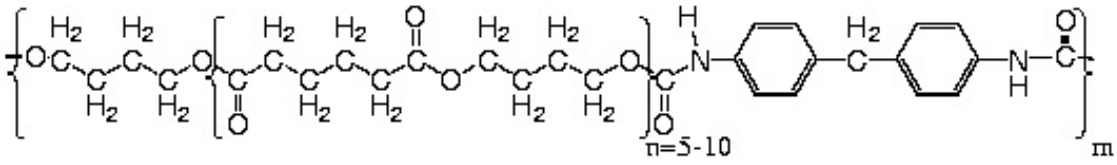

Figure 3.1 Molecular Structure of thermoplastic polyurethanes

3.1.2 Phenolic resins (PR)

Phenolic resins (or phenol formaldehyde resins) with formula $HOC_6H_4CH_2OH$ were supplied by Bayer Italia (Milan, Italy) and were used as the polymer matrices. It is a synthetic polymer obtained through the reaction of phenol or substituted phenol with formaldehyde.

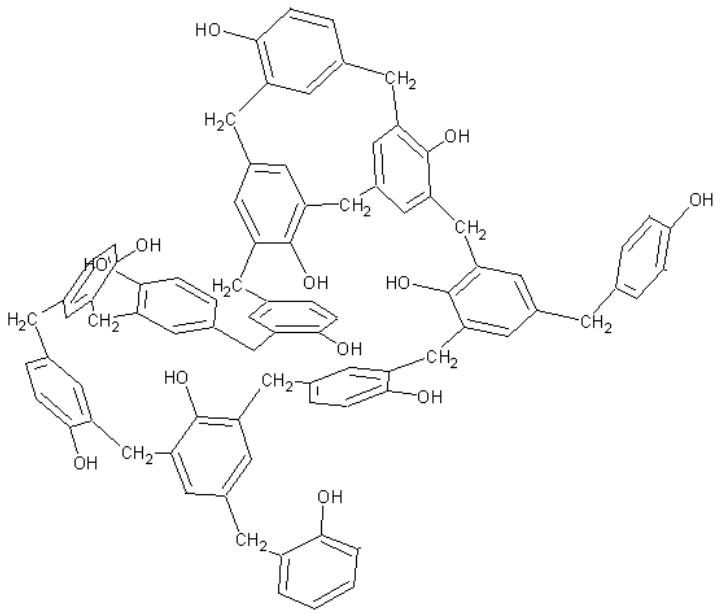

Figure 3.2 Molecular structure of phenolic resins

3.1.3 Polyvinylpyrrolidone (PVP)

PVP with molecular weight 1, 300, 000 $gmol^{-1}$ and molecular formula of $(C_6H_9NO)_n$ was supplied by Aldrich and is water-soluble polymer. PVP binds to polar molecules exceptionally well, owing to its polarity.

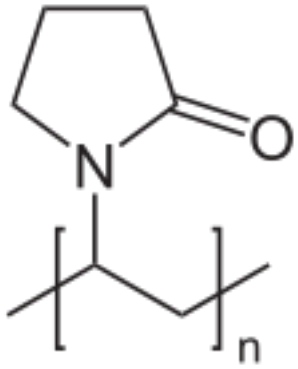

Figure 3.3 Molecular structure of PVP

3.1.4 Polymethylmethacrylate (PMMA)

Poly(methylmethacrylate) of molecular weight 120,000 g/mol were obtained from Sigma-Aldrich (Gillingham, UK). PMMA is an amorphous, transparent thermoplastic polymer widely used in biomedical applications such as bone implants (Bai et al., 2016), prosthetics (Caro-Osorio et al., 2013), dentistry (Canché-Escamilla, Duarte-Aranda, & Toledano, 2014), drug delivery (Zupančič et al., 2016), cosmetic surgeries and as intraocular lenses (Brint, Ostrick, & Bryan, 1991) implanted after cataract surgery. PMMA was selected as the model polymer for this study due to its high solubility in a wide range of solvents. Hierarchical structures of PMMA were prepared by several researchers (Deng et al., 2014; Morariu et al., 2003) using electrospinning as the fibre-making

technique. However, such a study has not been performed using pressurised gyration and, in this work, we are reporting the formation of hierarchical structures of PMMA using this forming route.

3.1.5 Graphene nanoplatelets (GNP)

The average single layer thickness of the GNPs were around 2 nm and diameter between 1 - 2 μm, with an average surface area of ~750 $m^2 g^{-1}$ and bulk density of ~0.2 g cm^{-3}. All reagents were used as received without further purification. Graphene nanoplatelets were supplied by XG Sciences (XGNP-C750grade) from Lansing, USA and were used as a filler material. A TEM micrograph of the GNPs is shown in Figure 4.1b. PX35.

Continuous tow carbon fibre was purchased from ZOLTEK (St. Charles, Missouri) and is a 50K filament fibre manufactured from a PAN precursor.

3.1.6 Solvents

A range of polymeric fibers were prepared by pressurised gyration using acetone, chloroform, N,N-dimethylformamide (DMF), ethyl acetate and dichloromethane as solvents. It was found that microscale fibers with surface nanopores were formed when using chloroform, ethyl acetate and dichloromethane and poreless fibres were formed when using acetone and DMF as the solvent. These observations are explained on the basis of the physical properties of the solvents and mechanisms of pore formation. The formation of porous fibres is due to many solvent properties such as volatility, solubility

parameters, vapour pressure and surface tension (Illangakoon et al., 2017). N,N-dimethylformamide (DMF) were purchased from Sigma Aldrich (St. Louis, MO) and used as received without further purification. It is an organic compound with the formula $(CH_3)_2NC(O)H$, it is colourless and has a fishy odour. DMF is a polar (hydrophilic) aprotic solvent with a high boiling point. The molecular structures in Figure 3.4 indicates partial double bond character for the C-N and C-O bonds. Thus, the infrared spectrum shows a C=O stretching frequency at only 1675 cm^{-1}, whereas a ketone would absorb near 1700 cm^{-1} (Comins & Joseph, 2001).

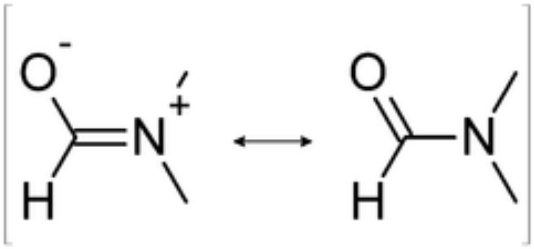

Figure 3.4 Two resonance structures of DMF

3.1.7 Polyacrylonitrile (PAN)

Polyacrylonitrile (PAN) was used with the linear formula $(C_3H_3N)_n$ and is a synthetic, semicrystalline organic polymer resin with average molecular weight of 150,000, and density of 1.184 g/mL at 20°C. It is thermoplastic and does not melt under normal conditions but degrades before melting.

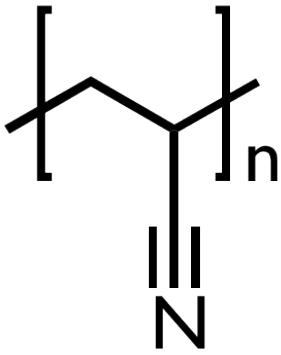

Figure 3.5 Molecular structure of polyacrylonitrile

3.1.8 Graphene oxide

The GO used in this study was synthesised at the University of Sheffield. Mutiple-layer graphene oxide with a purity of up 95 wt%, thickness of 3.4-8 nm was used. The diameter of the lamella 10-50 μm; the number of layers 5-10; and the specific surface area was 100-300 m^2/g; and with an appearance color of brown and yellow powder.

3.2 Preparation of graphene oxide (GO) suspensions

Graphene nanoparticle (GNP) or graphene oxide (GO) in DMF were sonicated in an ice bath using an ultrasound sonifier (Bransonsonifier 250) at a power output of 60 % for 4 hours. It should be noted that DMF was used as the processing solvent due to its low boiling point (~80 ^oC) which enabled easy drying. This prevented aggregation of the graphene nanoparticles in the polymer solution at an ambient temperature (~20 ^oC).

Four different GO concentrations (3, 5, 8 and 10 wt%) were prepared using DMF in an airtight bottle and these polymer solutions were magnetically stirred for 50

hours at ambient temperature. The prepared solutions were used to make GO containing polymer solutions.

Then from the suspension of GO, a few mililiters of solution was added to each polymer solution. The resulting polymer-graphene solutions were magnetically stirred for 5 hours at ambient temperature.

3.3 Solutions for generating nanofibre

Three different TPU concentrations (15 wt%, 20 wt% and 25 wt%) were prepared using DMF in air tight bottle and these polymer solutions were magnetically stirred for 50 hours at ambient temperature. The prepared solutions were used to make GNPs containing polymer solutions. For this purpose, the above prepared GNP suspensions were ultrasonically treated in an ice bath using an ultrasound sonifier (Branson sonifier 250) at a power output of 60 % for 30 minutes. Then from the suspension of GNPs, a few mililitres solution (5 wt%) was added into each polymer solution. The resulting polymer-graphene solutions were magnetically stirred for 5 hours at ambient temperature. The final solutions were again ultrasonically treated for 30 minutes before used in pressurised gyration at ambient temperature.

Similarly, three different PR concentrations (10 wt%, 15 wt% and 25 wt%) were prepared using DMF in air tight bottles and these polymer solutions were magnetically stirred for 50 hours at ambient temperatures. Separately, 10 wt% polyvinylpyrrolidone (PVP, Sigma Aldrich, UK) was prepared in de-ionised water in an air tight bottle at ambient temperatures. Then from the suspension of GNPs,

few millilitres solution (5 wt%) was added into 10 wt% PVP solution and stirred for 3 hours. The PVP was added to modify and improve the rheological behaviour of the spinning solution. Finally, this solution was added to each PR polymer solution and ultrasonically treated for 30 minutes before using in pressurised gyration.

3.3.1 Characterisation of solutions

Solution characterisation mainly involved measuring viscosity and surface tension of liquid preparations from which fibres were spun. These are the two most important properties affecting nanofiber processing and outcome, as established by (Mahalingam & Edirisinghe, 2013) in their pioneering experiments on fibre generation by pressurised gyration.

3.3.1.1 Viscosity

The viscosity for each polymer solution or blend was measured using Brookfield DV-111 viscometer (Harlow, Essex, UK) at a specific shear stress (indicated where relevant). The Brookfield DV-111 is a rotational viscometer that measures the absolute viscosity of fluids using the torque of a rotating spindle submerged in the fluid being analysed to calculate the resistance to flow. In simple terms, the viscosity measured by this equipment is a function of the resistance encountered by the spindle as it rotates through the liquid being analysed at a particular shear stress. In measuring viscosity, 5ml of solution was placed in a

tube and a spindle (Number 18) was lowered into the tube such that it was completely submerged in the solution being analysed.

At a shear stress of 3.5 Pa, suitable point for consistent readings for the viscosity range of all liquids analysed, the dynamic viscosity of each solution was taken and noted. Four additional measurements were taken for each batch of solution. The mean and standard deviations from the five measurements were used in subsequent analyses.

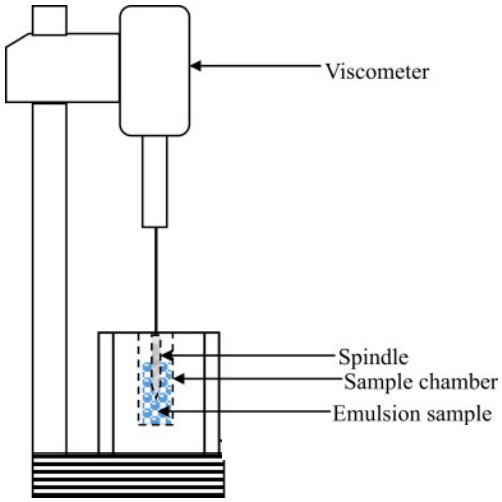

Figure 3.6 Schematic diagram of rotational viscometer

3.3.1.2 Surface tension

Solution surface tension measurements were done using a Kruss K9 tensiometer (Hamburg, Germany). The Wilhemy plate method, in which a thin platinum plate (Kruss PL21, Hamburg, Germany) is positioned perpendicular through the liquid being analysed and the force required to break contact between the plate tip and liquid surface is measured to assess the surface tension of solutions. The

surface tension is given as a function of the force (F), the wetted perimeter of the platinum tip (ι), and contact angle θ (Butt et al., 2003). The equation is given below:

$$\gamma = \frac{F}{\iota \cos(\theta)}$$

When complete plate wetting by the liquid being analysed has occurred, which is usually the case in this method, the contact angle, θ is 0°. Cos 0 is 1 therefore effectively, surface tension measured by this method is given as a ratio of F and ι, calculated as *2w +2d* where w and d are width and thickness of the platinum plate respectively.

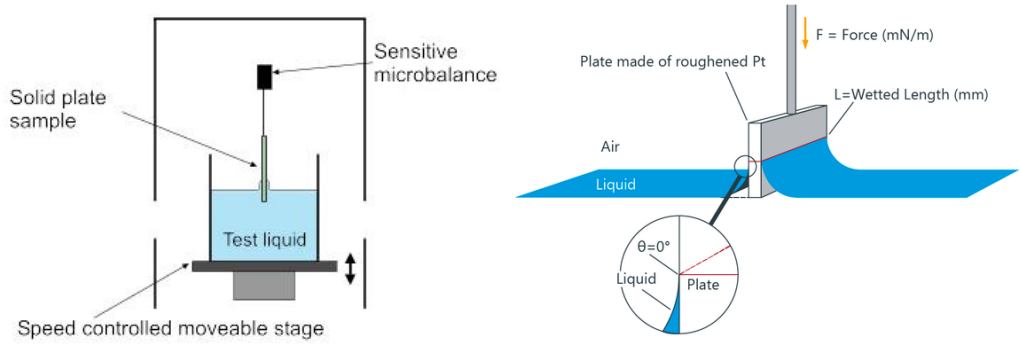

Figure 3.7 Schematic diagram of the Wilhelmy plate method (Kruss Scientific)

In assessing these, the platinum plate connected to a balance was dipped into 20 ml of solution in a 25 ml beaker on a fixed stage. The platinum plate was gradually removed from the liquid with the automated balance recording the tension at the air-liquid interface. In all, five measurements were taken for each solution sample and the mean and standard deviations were used in subsequent analyses.

3.3.1.3 Particle size analysis - Transmission Electron Microscopy (TEM)

TEM was initially carried out at University of Sheffield to determine the lateral dimension and size distribution of the flakes. Owing to the precision of the TEM measurement, the lateral size distribution was then used as a benchmark for further experiments. Flake thickness was estimated by the Mean Grey Value Ratio (MGVR) method which is based on normalised TEM Bright Field image contrast (Rubino, Akhtar, & Leifer, 2016). Direct imaging of folded graphene edges and low-loss electron energy loss spectroscopy (EELS) was used at University of Sheffield to provide complementary information for MGVR measurements. In addition, an image technique was developed so that the flake lateral size distribution could be obtained rapidly via quantification of several optical microscopy images. To develop an in-situ characterisation technique, Dynamic light scattering (DLS) was performed at University of Sheffield to obtain the lateral size distribution of dispersed flakes. Although no precise or reliable parameters for graphene flakes dispersed in isopropyl alcohol (IPA) exist in the literature, approximate optical parameters were used to perform the DLS analysis.

TEM measurements were conducted using an FEI Titan3 Themis 300 S/TEM operated at 80 kV, which is below the threshold for knock-on damage (Banhart, 2004). TEM magnifications of 55,000 x and 295,000 x were used for the development of MGVR and folded edge methods respectively. EELS measurements were recorded in diffraction mode from an area of ca. 100nm in diameter.

3.3.2 Method of melt compounding

Beforehand, the TPU was dried under vacuum at 50 ^{o}C for at least 48 h before melt compounding. Each polymer/GNP composite was prepared by a mini-compounder, DSM Micro-extruder 15 (DSM Research B.V., The Nederlands) has 15ml volume capacity, co-rotating twin screws and the temperatures of 230 ^{o}C, 50 rpm and mixing for 5 min.

3.3.3 Preparation of Solutions of TPU/GNP using Melt Compounding Technique

The size of GNP was 15μm, and the temperature of the screw during the mixing was 230 ^{o}C. The pressure was 0.1 MPa with Argon flow during mixing. Composition of the compound was 20 wt% GNP, 80 wt% TPU according to the experimental section in Chapter 4. Processing parameters: 13.5g DMF + 7g melt compounding (34 wt% melt compounding).

3.3.4 Preparation of solutions of GO/PAN

The gyration solutions were prepared by dispersing an appropriate amount of GO (3, 5, 8 and 10 wt%) relative to the solution of PAN which was of 8 wt% in DMF, and the solution was sonicated for 1h in an ice-water bath to disperse the GO homogeneously.

3.4 Fibre generation

In order to generate fibres from pressurise gyration set up, the vessel with all its connections are held in place securely by a retort stand and clamps. The gyration

process is carried out in a Perspex box to ensure safety. Aliquots of the solution to be spun into fibres are placed in the vessel and covered. Rotation begins at the same time as pressure is being applied. Each cycle takes between 2-5 minutes depending on the experimental conditions. Fibres ejected through the nozzles are collected and stored until required for further analyses.

The gyration system consists of a rotary aluminium cylindrical vessel containing 20 small round orifices equally spaced on the face in Figure 3.8. The dimensions of vessel and orifices are 60 mm in diameter with a height of 25 mm, and 0.5 mm in diameter which can form micro- to nanofibres by ejecting polymer solution as the vessel rotates at high speed, located at the same vessel height, respectively. An inlet pipe of N_2 gas was connected from the top of the vessel to induce pressure in the rotating vessel.

A gas regulator controlled the flow into the vessel. The bottom end of the vessel was connected to a DC motor, which can produce variable speeds up to 36k rpm. In order to investigate the nanofibre size and size distribution under different conditions, the polymer solution was spun at three different rotating speeds (10 k, 24 k, 36k rpm) at ambient temperature (~20 °C) and relative humidity (~ 42 %). Protected by a transparent plastic container, the system allows convenient collection of the polymer fibres on stationary aluminium foil sheets within the container.

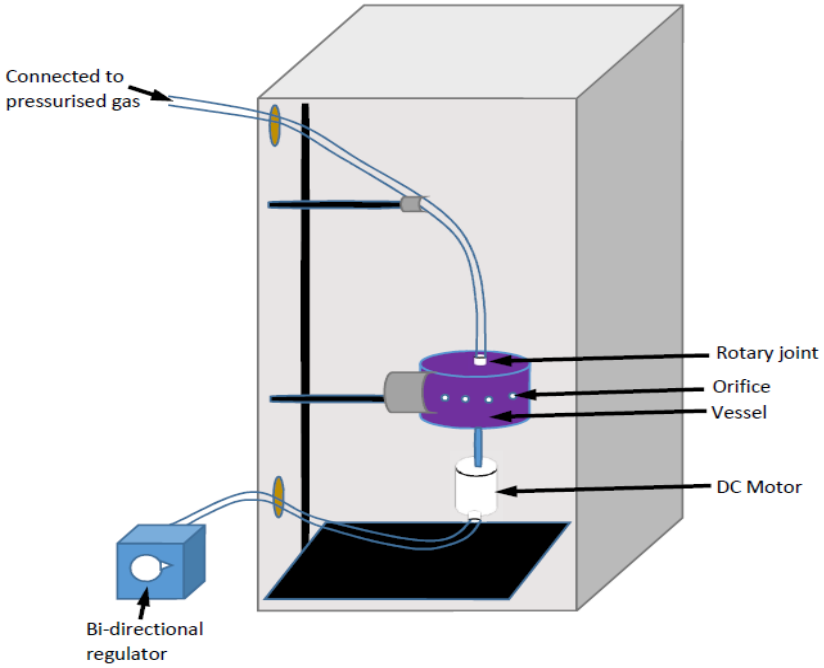

Figure 3.8 Gyrator set-up used in this work

3.4.1 Pressurised gyration of GNP/PAN

The gyration solutions were prepared by dispersing an appropriate amount of GNPs (0, 0.2, 1, 3 and 8 wt%) relative to solution of PAN, which was of 10wt% in DMF, and the solution was sonicated for 1h in an ice-water bath to homogeneously disperse the GNPs. A schematic of the pressurised gyration set up is shown in Figure 3.9.

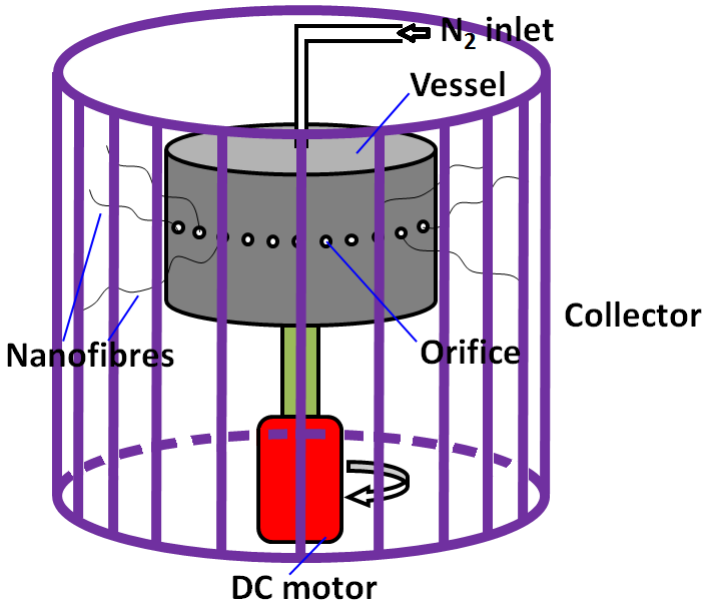

Figure 3.9 Schematic illustration of pressurised gyration process.

During gyration, the working pressure was varied from 1 to 3 $\times 10^5$ Pa by controlling the pressure of inlet N_2 gas into the vessel, and the rotational speed was varied from 10 k to 36k rpm by a bi-directional regulator. The as-spun PAN/GNPs precursor nanofibres were collected randomly as an overlaid mat on aluminium foil placed on the inner wall of the collector. The compositions and processing parameters of different samples are compiled and shown in Table 3.1.

The weight percentage value of GNP in solution has been used consistently, as the GNP concentration in the following text for consistency.

The compositions and processing parameters of different samples are tabulated and shown in Table 3.2.

Table 3.1 The concentration of GNPs and the parameters of pressurised gyration.

Sample number	GNPs concentration[a]	Rotational speed(rpm)	Working pressure(×10^5Pa)
1#	0	10k, 24k, and 36k	1, 2, and 3
2#	0.2	10k, and 24k	1
3#	1	10k, and 24k	1
4#	3	10k, and 24k	1
5#	8	10k	1

[a]The concentration of GNP in the solution was calculated by the weight of GNP divided by the total weight of GNP and PAN solution. The concentration of GNP in the as-spun fibre was calculated by the weight and density of GNP and PAN.

Table 3.2 Generating as-spun fibres of 8 wt. % PAN

As-spun fibres	GO concentration	Rotational speed (rpm) vs. Working pressure (x10^5Pa)								
Speed (rpm) vs. Pressure (x10^5 Pa)		10k			24k			36k		
		1	2	3	1	2	3	1	2	3
27.3	3	X	/	X	/	X	/	X	X	X
38.5	5	X	X	X	/	/	/	/	/	/
46.7	8	X	X	/	/	/	/	/	/	/
55.5	10	X	/	/	/	/	/	X	/	/

/ fibre was produced during the pressurised gyration process

X no fibre produced or polymer spraying

The development of 8 wt% PAN with various GO concentrations was compared with 10 wt% PAN in Table 6.1 . Some of the solutions did not produce any fibre composites. This condition can be attributed to the internal interaction between hydroxyl and amine groups in an aqueous bed which can deteriorate jetting ability of resulting solution by increasing the surface tension. To overcome this

particular problem of polymer droplet, the polarity of the solvent plays an important role opposed to the concentration and viscosity. At lower concentrations, some fibrous structures formed. When changing the polarity of the solvent by mixing with other polar/non-polar solvents, the choice of solvent and amount have to be judicious to keep the polymers soluble and generate fibres while spinning.

3.5 Carbonization and SPS processing

The as-spun TPU/GNP, PR/GNP, PAN/GNP, nanofibres were peeled off from the aluminium foil and placed in a horizontal tube furnace for heat treatment at Padova University, Italy. GO/PAN and TPU/GNP melt compounded was pyrolyzed at China University of Geoscience Beijing. Before carbonization, there was a stabilization process on the as-spun samples, which took place at 290 ^{o}C for 30 mins. Then the samples were heated again from 290 ^{o}C with a heating rate of 2 ^{o}C/min and maintained for 1 h at 900 ^{o}C before further heating at a heating rate of 2 ^{o}C/min. Subsequently, the samples were maintained for 1 h at the final temperature under an argon gas flow (60 mL/min) for carbonization. The products were cooled to 25 °C under an argon atmosphere at a cooling rate set at 2 °C/min. This treatment was tailored to generate carbon nanofibres containing graphene.

3.6 Pyrolysis of the fibres using spark plasma sintering

The TPU-GNP, PR-GNP and GNP/PAN fibres had been pyrolysed using spark plasma sintering at Queen Mary University of London and also using argon assisted vacuum at temperature of 2000 ^{o}C. However, the pyrolysed samples did not remain in a fibrous form, hence the solidification of the graphene nanoplatelets did not occur as expected. The carbonized samples were put into a 20 mm graphite crucible and then sintered in a vacuum (1-3 Pa) in a SPS furnace. A heating rate of 200 °C/min was used, and the final temperature was 2000 °C with a dwell time of 10 minutes.

The applied direct current in the SPS was 1000-1500 A, with a pulse duration of 12 ms applied at an interval of 2 ms. The CNF samples after carbonization and SPS processing are referred to in this work as ‘pyrolyzed’ and ‘after-SPS’ CNFs, respectively.

3.7 Characterization

The rheology of the spinning dopes’ was analysed using a Brookfield viscometer. The viscosity measurement was carried out a shear rate in the range from 0.132 s^{-1} to 1.32 s^{-1} at ambient temperature. The surface tensions of the solutions were measured using a Kruss tensiometer (Wilhemy plate method).

3.7.1 Average fibre size and size distribution

To measure the diameters of the as-spun PAN fibres and CNFs, an image analyser (Image-Pro express, Media Cybernetics Co, US) was used. At least five SEM images were used for each sample. One hundred positions were selected at random and the average fibre diameter and distribution was calculated.

First the scale is set. Then, pixels between two edges of a fibre perpendicular to the fibre axis are counted. The number of the pixels is then converted to nm using the scale and the resulting diameter is recorded. On a typical image, the diameter of 100 fibres are measured using this method and the fibre diameter distribution is plotted as a histogram.

3.7.2 Thermogravimetric analysis (TGA)

TGA of fibres with and without GNPs were carried out on a universal V4.5A TA instrument at a heating rate of 3 °C/min to 1000 °C under nitrogen atmosphere.

3.7.3 Morphology and crystallization

The CNFs prepared before and after SPS were repeatedly washed using deionized water and dried in an oven. A field-emission scanning electron microscope (SEM, HitachiS-3400n) was used to examine the morphologies of the prepared CNFs. The phase identification of the CNFs samples was performed using a Renishaw-2000 laser Raman spectroscopy system with a He-

Ne laser excited at 514 nm. The samples were also analysed using TEM (JEOL 2000) at 200 keV.

3.7.4 Electrical conductivity measurements

Electrical conductivity measurements of the as-spun, pyrolysed and after-SPS fibres were done using a two-point multimeter. Fibrous mats of known weight and length were placed on a glass slide and the ends of the fibres were soldered with silver paste to enable electrical contact. The cross-sectional area of the fibrous mats was calculated from the SEM images of the fracture surface of the CNF composites. Repeated measurements were carried out to determine the average electrical conductivity of each sample.

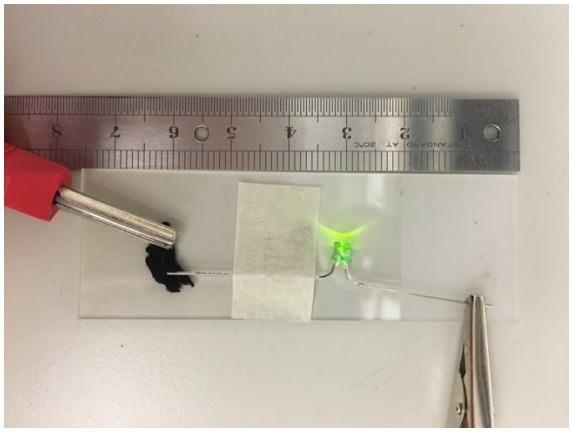

Figure 3.10 Electrical conductivity using LED

Electrical conductivity test using KingBright L-1334 Gx Green LED showed that it's lights on when connected to fibres after pyrolysis.

3.7.5 Mechanical property tests

The mechanical properties of the CNFs were evaluated using Raman spectroscopy after four-point bend testing of the samples. Initially, the CNF mats were placed on a poly(methyl methacrylate) beam and covered with a thin layer of PVA. The beam was then inserted into a four-point bending rig and deformed under various levels of strain. Subsequently, the samples were placed on a Raman microscope stage, and the surface strain was measured after three accumulations. It was assumed that the strain in the PVA resin was the same as in the PMMA substrate.

3.7.6 Scanning Electron Microscope (SEM) Microscopy

The formed composite fibres were investigated with a scanning electron microscope (SEM, Hitachi S – 3400 n) at an accelerating voltage of 5 kV. The samples were coated with gold using a sputtering machine (Edwards Sputter S1 50B) for 150s to minimize charging effects prior to imaging. The obtained images were used to analyse the fibre size. Statistical analysis of fibre size was carried out by Image J software where ~ 100 measurements were obtained at different locations of each sample to calculate the average fibre diameter. Transmission electron microscopy was carried out on graphene nanoplatelets to determine their initial size using a JEOL-JEM 2000 F microscope operating at 200 keV.

3.7.7 Morphology and crystallisation

A field-emission scanning electron microscope (Hitachi S-3400N) was used to examine the morphology of the prepared CNFs. The phase identification of the CNF samples was performed using a Renishaw-2000 laser Raman spectroscopy system with a He−Ne laser excited at 514 nm. The samples were also analysed using TEM (JEOL 2000) at 200 keV.

3.7.8 Fourier transform infrared (FTIR) Spectroscopy

Fourier transform infrared (FTIR) spectra were recorded in the wavelength range 400 - 4000 cm^{-1} using FTIR spectrometer (Bruker-Alpha) equipped with an attenuated total reflectance (ATR) probe attachment along with an internal reflectance element (IRE) germanium (Ge) crystal at an end-face angle of 45°. The data was used to evaluate the interfacial interaction between graphene and polymer matrices.

3.7.9 Raman Spectroscopy

Raman spectroscopy is a fast, non-destructive, and high-resolution tool for characterisation of the lattice structure and the electronic, optical, and phonon properties of carbon materials. Phonons are the elastic arrangement of atoms or molecules in solids and liquids. Phonons play a major role in many of the physical properties of thermal conductivity and electrical conductivity. Raman spectra of graphene-based materials show few prominent features regardless of the final structure.

Raman measurements of the samples were obtained using a Raman microscope (inVia^{TM} Renishaw) excited with 633 nm incident wave length radiation. The data acquisition covered the spectral range 3000 - 100 cm^{-1} with a spatial resolution of 4 cm^{-1}. Raman data were baseline corrected. Raman has better spatial resolution than FTIR and enables the analysis of smaller dimensions, down to the 1μm range.

3.7.9.1 Full width at half maximum (FWHM)

Full width at half maximum (FWHM) is the width of a spectrum curve measured between those points on the y-axis which are half the maximum amplitude. is a reflection of the structural distribution. Thus, for exactly the same molecule, crystalline material shows sharper Raman line than the amorphous material.

3.7.10 Focused Ion Beam (FIB) Microscopy

A FEI Nova 200 dual beam focused ion beam (FIB) system was used to study the cross-sections of the composite fibres. The milling was performed with a 1–5 nA, 30 kV Ga ion beam, followed by cleaning steps at lower currents. SEM imaging of the cross-section was performed using 10 kV and 30 kV beams, with a working distance that varied between 8 and 20 mm and with the composite fibres tilted by 52°.

Chapter 4 Generating graphene nanoparticle loaded polymer fibres

4.1 Introduction

In this chapter, the possibility of producing graphene fibres with polymer blends for the preparation of composites by pressurised gyration is discussed. The superior properties of graphene suggest that graphene could replace carbon nanotubes in existing applications. The combination of transparency, conductivity and elasticity will find use in flexible electronics (Novoselov et al., 2012), where the graphene fibres play a role.

Fibres from different types of polymers in different combinations were obtained from pressurised gyration at different speeds and working pressures. Scanning electron microscopy showed that fibres with diameters in the range of 296 nm to 5800 nm were successfully produced.

4.2 GNP characteristics

Figure 4.1 shows the characterisation of GNPs using Raman spectroscopy and TEM. TEM analysis was done on more than 100 particles. The statistical size distribution of GNPs showed average length and width of the flake to be 964 ± 353nm, 457 ± 214 nm, respectively (Figure 4.1b).

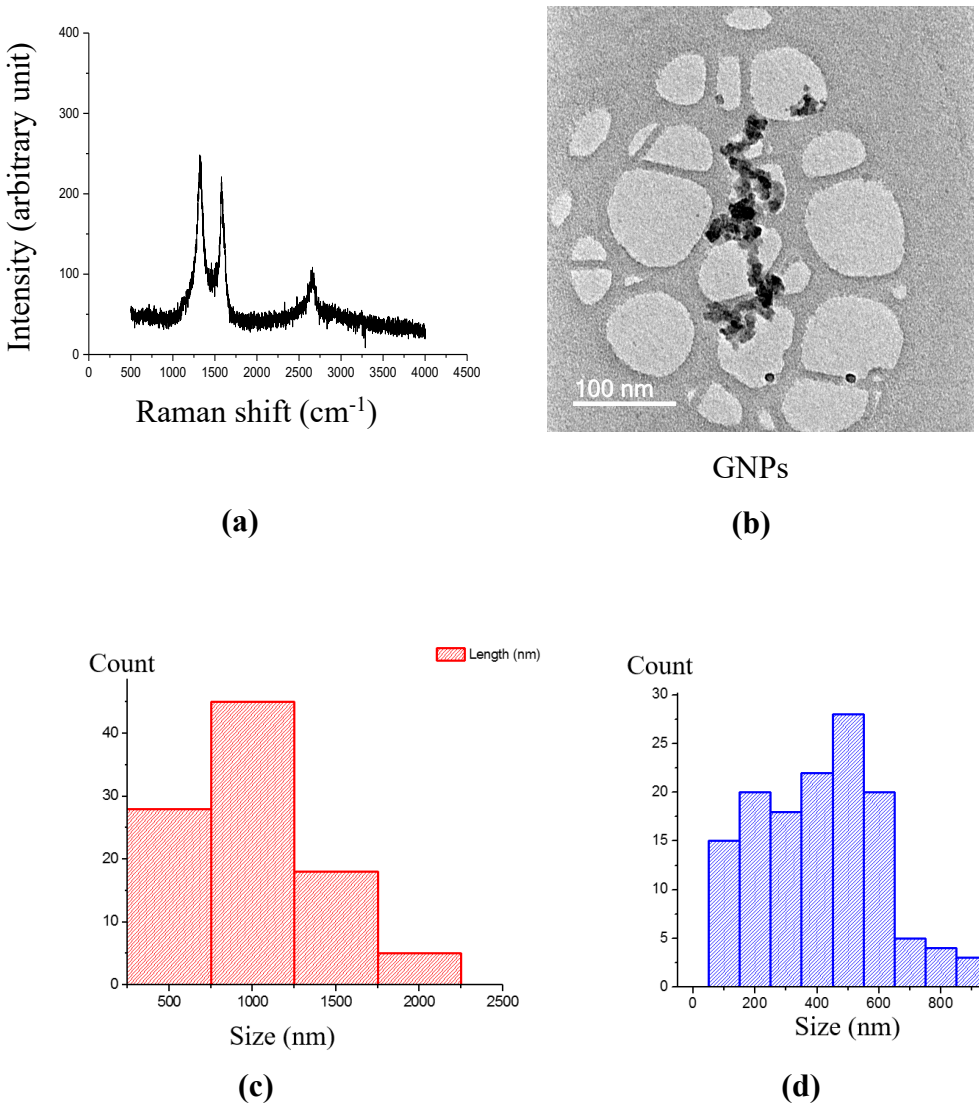

Figure 4.1 a) Raman spectra: b) TEM image: and c) TEM generated statistics of the GNPs used in fibre composites; (a) in length and (b) the width

4.3 Relationships between solution properties and fibre outcome

4.3.1 Fibre morphologies of TPU-GNP composites

Optical micrographs of fibres formed at various working pressures and rotating speeds for TPU-GNP composites are shown in Figure 4.2 and Figure 4.3.

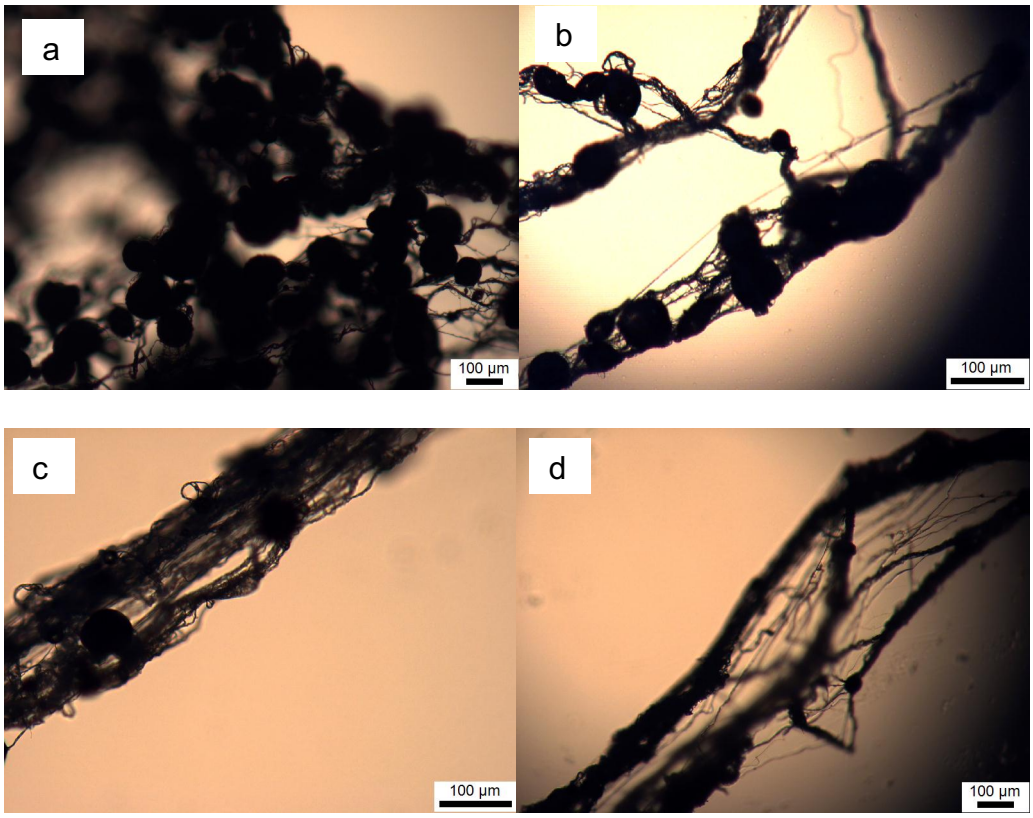

Figure 4.2 Optical micrograph of fibres formed at 20 wt% TPU + 5 wt% GNP in DMF at rotating speed of 24k rpm a) without pressure b) 0.1 MPa c) 0.2 MPa d) 0.3 MPa

Optical examination of the fibre composite shows that increasing pressure reduced the graphene deposition in the structure as show in Figure 4.2. A minimal amount of deposition appeared at maximum pressure of 0.3 MPa. A potential amount of continuation and in-line existing at 0.1 MPa which seems will be connected during thermal pyrolysis.

The same effect appear at the higher speed of 36k rpm in Figure 4.3. However, the amount of fibre bundle decreased when the speed increased.

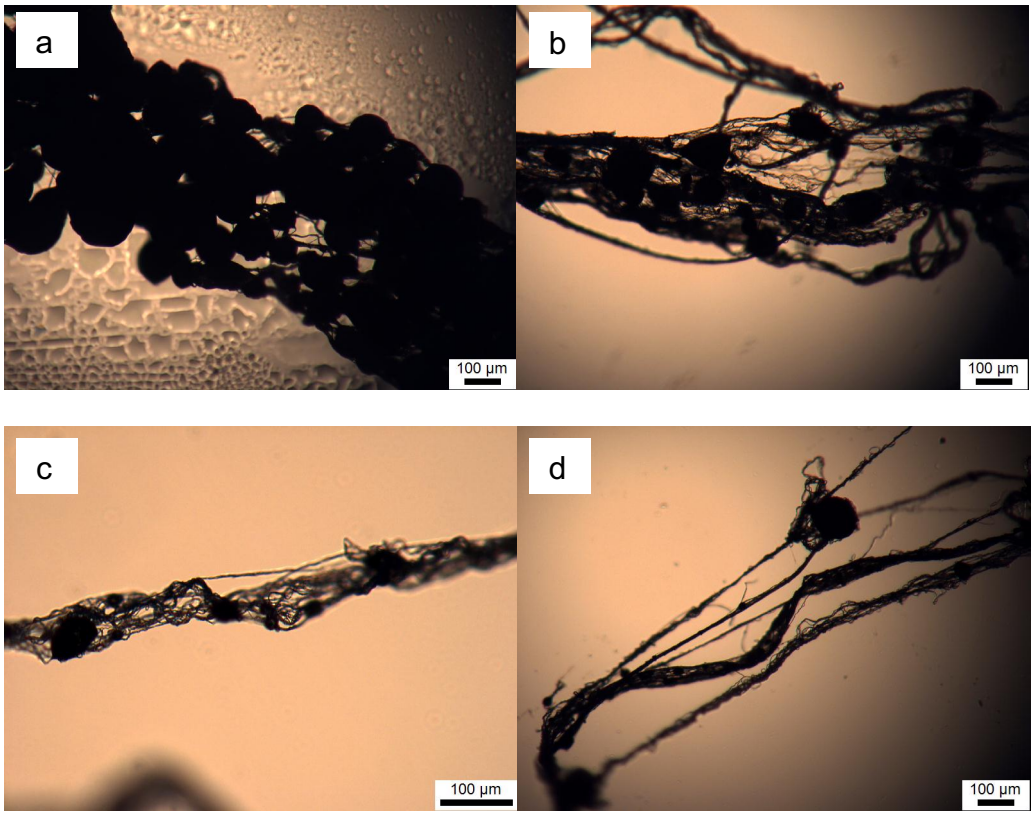

Figure 4.3 Optical micrograph of fibres formed from 20 wt% TPU + 5 wt% GNP in DMF at rotating speed of 36k rpm a) without pressure b) 0.1 MPa c) 0.2 MPa d) 0.3 MPa

4.3.2 Statistical analysis of flow of GNPs in composite fibres

Non-Newtonian fluids are fluids which do not obey Newton's law of viscosity. For describing Non-Newtonian fluids, let's recall the Newton's law of viscosity experiment. There are two long parallel plates situated at distance h to each other. The top plate is stationary and bottom plate is moving with velocity as shown in Figure 4.4. If a force, F, is applied to move plate, then pressure, (τ_{xy})

$$\tau_{xy} = \frac{F}{A}$$ **Equation 4.1**

Where A is the area of the plate; and under steady state conditions when h is small and when $\tilde{v}$ is the velocity of the spindle,

$$\frac{\delta v_x}{\delta y} = \frac{\tilde{v}}{h} \qquad \textbf{Equation 4.2}$$

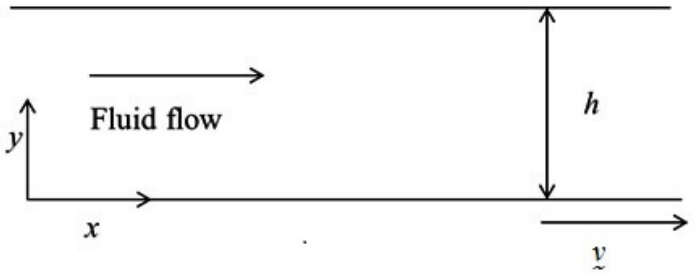

Figure 4.4 Non-Newtonian flow between two parallel plates

Now, we calculate τ_{xy} by repeating experiments for different applied forces and velocities ($\tilde{v}$) achieved by the bottom plate and plotting a graph as shown in Figure 4.5. Depending on the nature of the fluid, different types of curves may be obtained.

If the fluid shows behaviour like curve (1) then it is a Newtonian fluid. Other fluids are non-Newtonian fluids. Curve (2) represents a pseudo-plastic fluid, curve (3) represents a dilatant fluid, and curve (4) represents a Bingham plastic fluid in Figure 4.5. There are several theoretical and empirical models available to describe the rheological behaviour of non-Newtonian fluids.

The basic equation for a generalized non-Newtonian fluid is given below

$$\tau_{yx} = -\eta \frac{\delta v_x}{\delta y}$$ **Equation 4.3**

Here, η is the apparent viscosity, which is clearly a function of shear rate, as may be seen from Figure 4.5 Therefore,

$$\eta = f\left(\frac{\delta v_x}{\delta y}\right)$$ **Equation 4.4**

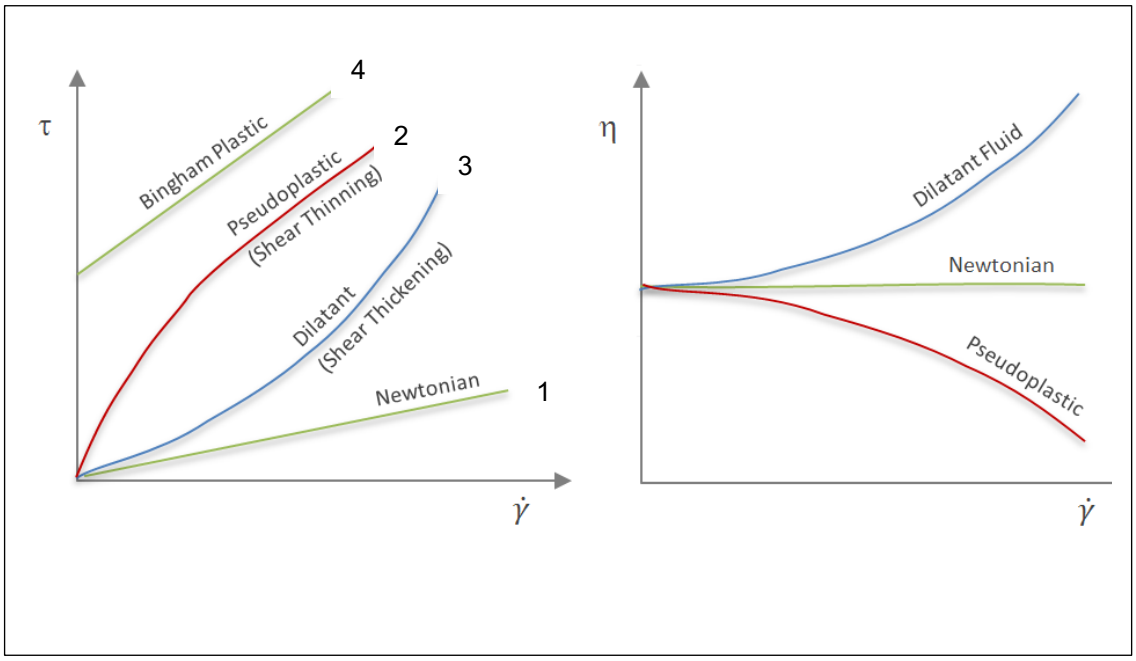

Figure 4.5 Shear stress vs. strain rate diagram for Newtonian and non-Newtonian fluids

If the apparent viscosity increases with increase in shear rate, $\frac{\delta v_x}{\delta y}$, then the fluid is called a dilatant fluid and if it decreases with increase in shear rate, $\frac{\delta v_x}{\delta y}$ then the fluid is called a Pseudo-plastic fluid. Some fluids require a critical shear stress to initiate the flow. These fluids are called Bingham plastics fluids. Some

important rheological models for non-Newtonian fluids are called as the power law or Ostwald De Waele model.

Power law or Ostwald De Waele model is the most generalized model for non-Newtonian fluids. The expression of this model is given in Equation below:

$$\tau_{yx} = -m\left(\frac{\delta v_x}{\delta y}\right)^{n-1}\left(\frac{\delta v_x}{\delta y}\right) \qquad \textbf{Equation 4.5}$$

Here, apparent viscosity η is defined as,

$$\eta = m\left(\frac{\delta v_x}{\delta y}\right)^{n-1} \qquad \textbf{Equation 4.6}$$

This is a two-parameter model where m and η are the two parameters.

If n= 1 then η = m, where m is similar to the viscosity of the fluid and the model shows Newtonian behaviour . If n >1, then η increases with increasing shear rate and the model shows the dilatant behaviour. If n <1, then η decreases with increasing shear rate and the model shows the Pseudo-plastic behaviour.

Shear thinning was apparent in all solutions and rheological data obtained was analysed using the Ostwald-de Waele model, $\eta = m\left(\frac{\delta v_x}{\delta y}\right)^{n-1}$,

where η is the shear stress (σ), $\left(\frac{\delta v_x}{\delta y}\right)$ is the shear rate ($\dot{\gamma}$) and power law index n is calculated for all samples and shown in Table 4.1 as $\sigma = k\dot{\gamma}^{n-1}$.

Flow curves of TPU, PR, TPU-GNP and PR-GNP polymer solutions are shown in Figure 4.6. All curves showed non-Newtonian behaviour and the viscosity increased with increasing polymer concentration. For example, TPU solution with 20 wt% polymer shows a viscosity of 184 Pa s at a shear rate 0.132 s^{-1} (Figure 4.6a). Similarly, TPU-GNP solution with 25 wt% polymer shows a viscosity of ~37Pa s whereas the same solution with 15 wt% polymer shows ~6 Pa s at a shear rate 0.132 s^{-1} (Figure 4.6b).

However, it was not possible to measure the viscosity of the 25 wt% solution as it exceeded the measurable range of the rheometer. But, adding GNP to the 25 wt% TPU solution reduced the viscosity value to within a measurable range. Shear thinning is apparent in all solutions and rheological data obtained was analysed using the Ostwald-de Waele is calculated for all samples and shown in Table 4.1.

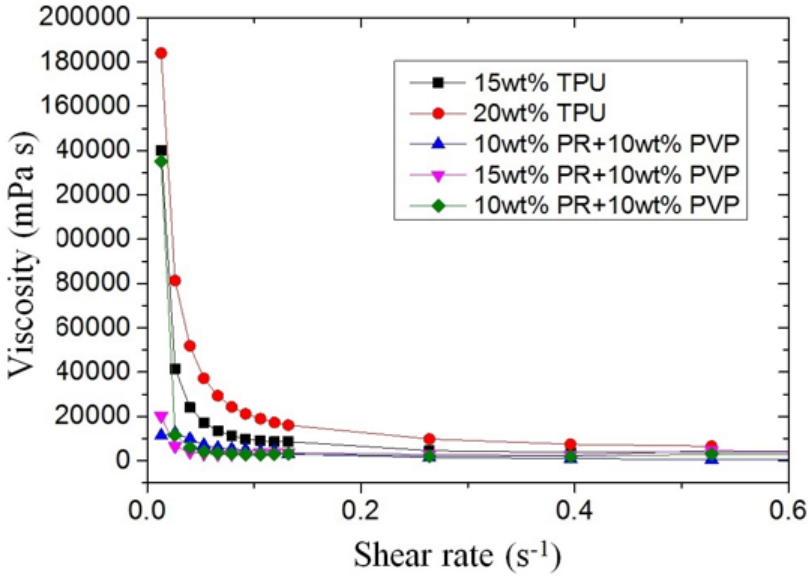

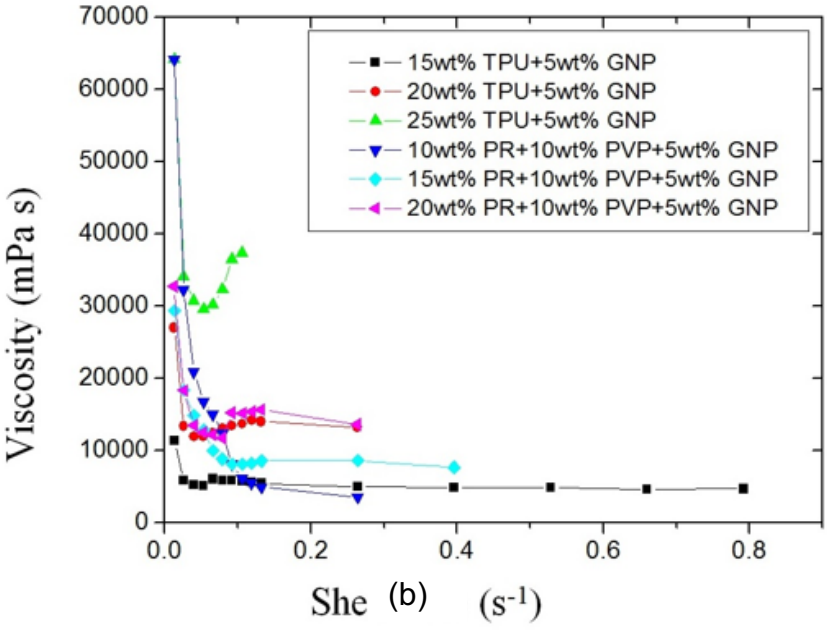

Figure 4.6 Flow curves of the various (a) TPU, PR, (b) TPU-GNP and PR-GNP polymer solutions at ambient temperature

Table 4.1 Flow index and surface tension of polymer solutions used in this experiment

Polymer solution	Power law index (n) ± 0.01	Surface tension (mN/m)
15 % TPU	0.21	-
20 % TPU	0.11	-
25 % TPU	-	-
15 % TPU-5 % GNP	0.83	-
20 % TPU-5 % GNP	0.80	-
25 % TPU-5 % GNP	0.73	-
10% PR-10 % PVP	0.98	49
15 % PR-10 % PVP	0.79	-
20 % PR-10 % PVP	0.53	-
10% PR-10%PVP -5%GNP	0.24	76
15% PR-10%PVP-5%GNP	0.32	-
20% PR-10%PVP-5%GNP	0.75	-

The increase in concentration of polymer showed significantly more shear thinning behaviour in all TPU solutions (low n value). The PR solutions showed the opposite effect compared to TPU solutions, where there was significantly more shear thinning at a lower concentration of polymer. Different TPU-GNP and PR-GNP concentrations showed almost similar trend in their flowability. It is interesting to see that adding GNPs showed a decrease in shear thinning compared to equivalent solutions without GNPs. It is reported that the viscosity of particle containing polymer solutions depends on particle size (Kamibayashi, Ogura, & Otsubo, 2006). The dynamic structure of shear fields is governed by a balance between Brownian motion and the hydrodynamic force in solutions containing well dispersed non-interacting particles (Kamibayashi et al., 2006). The viscosity at a given shear rate is higher for smaller particles. Moreover, the degree of flocculation also influences the flow behaviour and the shear thinning

effect. In general, in a highly flocculated system a three dimensional network of flocs is developed and the viscosity increases and the shear thinning effect becomes striking (Kamibayashi et al., 2006). In addition, the resistance of the macromolecular solution to shear and the extension increases with the particle concentration, however, the increase in extension is much greater than its increase in shear (Wang & Joseph, 2003). Table 4.1 also shows the surface tension forces for some of the polymer solutions used in the experiments. The surface tension value for 10% PR-10% PVP polymer solution is 49 mN/m, while 10% PR - 10%PVP - 5% GNP solution was 76 mN/m, indicating that the surface tension values increased with the GNP loading. In general, an increase in surface tension is observed with increase in polymer concentration but some values could not be accurately determined as they were extremely high and successful pull-out of the Wilhemy plate could not be achieved.

The spinning dope's rheological properties influences fibre formation in pressurised gyration (Mahalingam et al., 2014). It has been shown that the polymer chains act as a thickener and stabilizer against the suspensions and act against sedimentation (Mahalingam et al., 2014). In addition, there needs to be a minimum concentration of the polymer solution for initiating fibre formation, below this minimum polymer concentration only beaded structures are formed. This is either due to lack of polymer chain entanglement or lack of shear forces to drive the polymer jet to form fibres (Mahalingam & Edirisinghe, 2013). Generally, during the polymer stretching process, the polymer molecules that have a smaller hydrodynamic volume and relaxation time of chains acts as a

weaker link that causes an imminent break of local chain-chain coupling within the jet resulting in formation of polymer droplets (Gupta at al., 2005). In contrast, at higher concentrations and higher viscosities, sufficient chain entanglement is reached allowing uniform extrusion of polymer fibres. Higher surface tension promotes beads and beaded fibre formation and reducing surface tension favours the formation of fibres without beads (Fong, Chun, & Reneker, 1999). Moreover, elongational flow affects the molecular stretching and the solvent evaporation affects the solidification of the formed fibres during pressurised gyration. The rotating speed and working pressure of the gyration process can determine the morphology of the product and therefore, careful selection of the operation conditions is vital to the success of the process (Mahalingam *et al.*, 2015a).

4.3.3 Rheological study of fibre diameter variation with polymer concentration

Figure 4.7a shows the plot of fibre diameter variation with the polymer concentration for the polymer solutions gyrated under a fixed rotating speed of 36k rpm. It is clearly seen that the fibre diameter is significantly reduced with increase in polymer concentration.

For phenolic resin-based fibres the diameter increased from 844 nm to 2534 nm when doubling the polymer concentration from 10 wt% to 20 wt%. For TPU based fibres the diameter increased from 296 nm to 5800 nm when increasing the polymer concentration from 15 wt% to 25 wt%. The percentage increase in fibre diameter is higher for TPU fibres compared to PR fibres. This is attributed to the

viscosity of the polymer solutions where the TPU polymer shows a much greater increase in viscosity compared to the PR polymer.

For 20 wt% TPU solutions, the variation of rotating speed and working pressure had a marked influence on fibre diameter of graphene loaded fibres. Here the fibre diameter was reduced when the working pressure increased from 0 MPa to 0.3 MPa for the rotation speeds of 24k rpm and 36k rpm (Figure 4.7b).

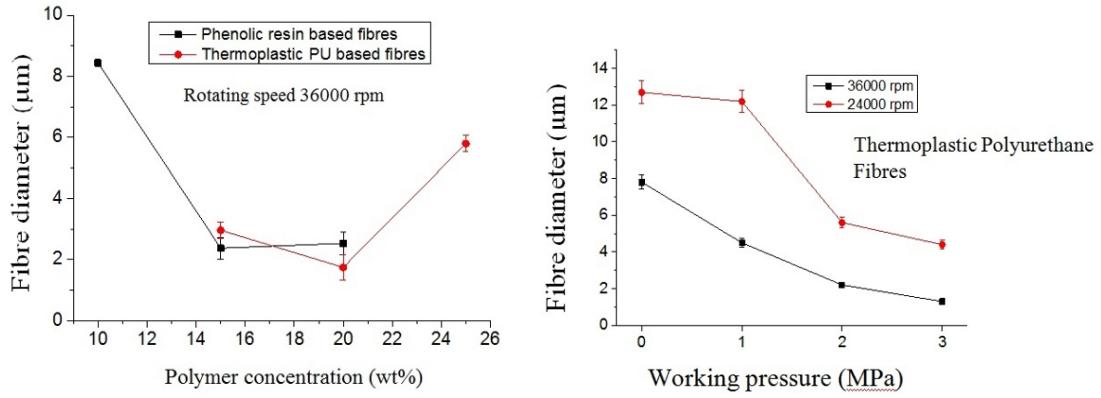

(a) (b)

Figure 4.7 (a), (b) Fibre diameter variations for various TPU, PR, TPU-GNP and PR-GNP polymer fibres made by pressurised gyration at ambient temperature

However, for the rotational speed of 1k0 rpm there is no fibre produced due to insufficient forces for fibre spinning. During spinning, the traveling polymer jet experiences aerodynamic forces that may impact the stretching of the jet and, thereby further alter the final fibre size and size distribution (Padron et al., 2013). In fibre forming processes, viscosity and concentration of the polymer solution influence the resulting fibre size and fibre morphology (Bhardwaj & Kundu, 2010; Mahalingam & Edirisinghe, 2013). In a typical pressurized gyration process, these properties also affect polymer chain entanglement, a prerequisite to the

formation of nanofibres (Mahalingam et al., 2014; Mahalingam & Edirisinghe, 2013).

4.4 Composition of fibres

A combination of FTIR, Raman and FIB spectroscopy were employed to verify the content of fibres produced from the blends. Though precautions were taken to ensure the mixing was homogeneous, it was important to conform of the constituents of the produced fibre. The high velocity of the rotational speed and pressure applied during fibre formation could result in phase separation.

4.4.1 FTIR spectra

FTIR spectra of TPU and PR and blends containing them, as expected gave profiles similar to those of the pure polymers. Figure 4.8 shows FTIR spectra of GNP, TPU based fibres and PR based fibres obtained at ambient temperatures. For GNP, the peak at 3400 cm^{-1} is attributed to the O-H stretching vibrations from the non-reduced graphene oxide in the GNPs (Padron et al., 2013). In addition, the presence of different types of oxygen functionalities in GNPs is confirmed at 1720 cm^{-1} (stretching vibrations from C=O), 1600 cm^{-1} (skeletal vibrations from unoxidised graphitic domain), 1220 cm^{-1} (C-OH stretching vibrations) and 1060 cm^{-1} (C-O stretching vibrations) (Xu et al., 2008). For TPU based fibres the peak at 3265 $cm^{-1}$is attributed to –NH urethane group and the peak at 2866 $cm^{-1}$is due to aliphatic hydrocarbon (C-H) (Li et al., 2015). The peak at 3455 cm^{-1} is assigned to free –NH group and the peak at 1714 cm^{-1} is attributed to the free C=O amide

I band (Barick & Tripathy, 2010). The occurrence of free and hydrogen bonded –NH in the case of TPU and the GNP loaded TPU fibres indicates that majority of –NH groups in urethane linkages participated in hydrogen bonding with the C=O group of the hard segment or, with the ether linkages of the soft segments or with the oxygen present in the fibre surface.

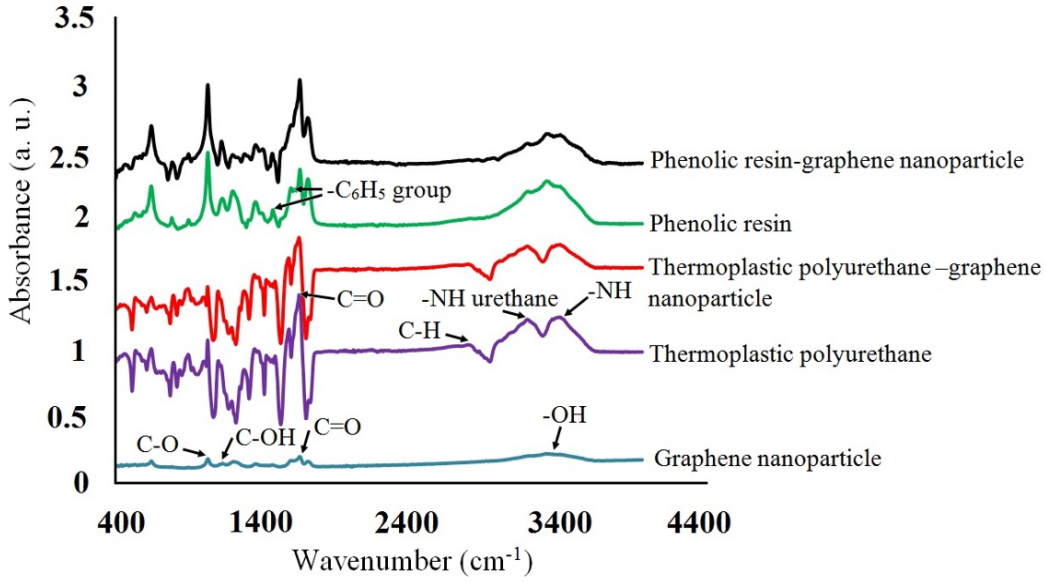

Figure 4.8 (a) FTIR spectra of GNP, TPU, PR, TPU-GNP and PR-GNP polymer fibres obtained at ambient temperature, a.u. indicates arbitrary units

The FTIR spectrum for the TPU-GNP composite fibres show a shifting of –NH and the C=O bonding peaks to higher wavelength regions than the pristine TPU counterpart. This red shift (Einstein shift) indicates that the hydrogen bonding is effective in the composite fibrous structures (Barick & Tripathy, 2010). For phenolic resin, the peaks at 1508 cm^{-1} and 1611 cm^{-1} are related to the stretching vibrations of the aromatic group and the peaks at 875 cm^{-1} and 751 cm^{-1}

demonstrate that the aromatic rings of phenolic resin possesses a large amount of substitute groups (Saito et al., 2002).

4.4.2 Raman spectra

Figure 4.9 shows the Raman spectra of the GNPs used in the experiment. Peaks were observed at 1350 cm^{-1} (D band), 1585 cm^{-1} (G band) and 2700 cm^{-1}(2D band). I_D/I_G ratio for the used GNPs was 0.81± 0.05 which is typical for the graphene produced using liquid phase exfoliation (Porwal et al., 2014). At least three Raman scans were done.

Raman spectroscopy was employed to evaluate the hybridization state of the carbon bonds (Dresselhaus et al., 2002), and the two reflections peak change from graphene nanoplatelets. Raman data for various TPU composites has been shown in Figure 4.9a. As shown in Figure 4.9a, a strong band at 1580 cm^{-1} (G band) and a relatively weak band at 1352 cm^{-1} (D band) appear in the Raman spectra of GNP, which stem from the vibration of sp^2-hybridized graphitic domains (Dresselhaus et al., 2002), and sp^3-hybridized carbon or structural defects (Kudin et al., 2008), respectively. The low I_D/I_G value (0.41) indicates that the graphitic domains were primarily intact for the composite fibres (Song et al., 2011).

The thermal degradation behaviours of the specimens were examined by thermogravimetry (TGA). Figure 4.9b shows the typical thermograms of TGA curves. The initial weight loss was accelerated in the presence of GNP due to

the pyrolysis of the labile oxygen-containing functional groups (Jing et al., 2014; Stankovich et al., 2007).

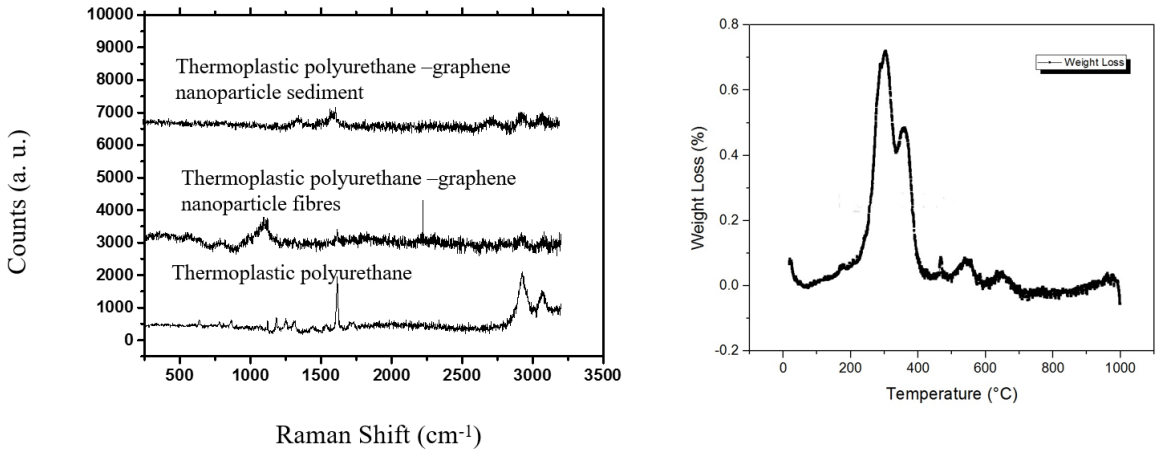

Figure 4.9 (a) Raman spectroscopy results of TPU-GNP composites (b) Derivative of thermogravimetry results of TPU composites

To observe the GNPs embedded in the TPU and the PR, fibres were analysed using FIB-SEM. An ion beam probe was used to cut and etch the fibre surface and remove a part of the fibre through milling, and then cross sections of the fibre were imaged under the SEM.

4.4.3 FIB

Figure 4.10 shows the focussed ion milling and imaging of the thermoplastic PU fibre surfaces.

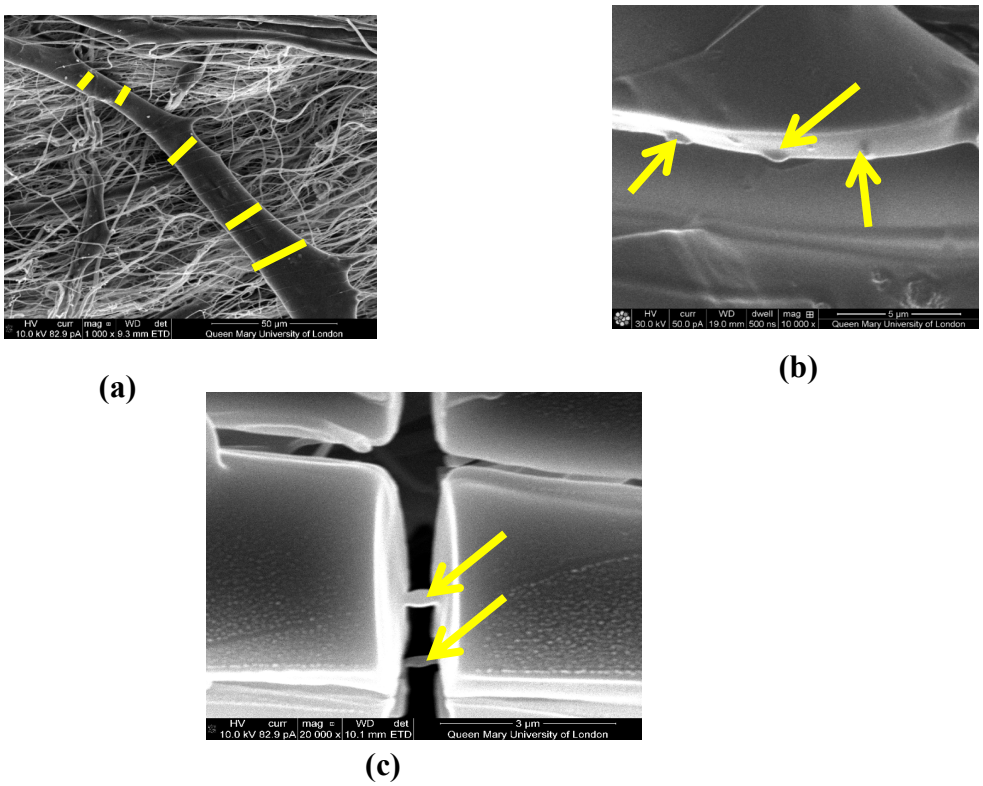

Figure 4.10 FIB-SEM images of TPU-GNP (a) FIB milling points (b) Graphene nanoplatelets within the fibres (c) Contrast effect showing the GNPs

As indicated by the dark yellow lines in Figure 4.10a, various randomly points were selected along a fibre length to determine the packing of the GNPs in the composite structure. The embedded GNPs in the polymer matrix is validated using ion milling. As clearly seen in Figure 4.10b protruding graphene platelets appear in the fibrous structure after the ion milling.

In addition, the contrast of different surface layers due to difference in secondary electron densities between the polymer matrix and GNP surface clearly demonstrate the existence of GNPs in the composite fibre structures. The GNPs were embedded in the polymer matrix along the fibre drawing direction. As can be seen in the cross sections of the fibre in Figure 4.10b,c there are light-shaded

graphene platelets (indicated by arrows) surrounded by the dark regions of the polymer matrix.

To verify the graphene platelets in the polymer matrix, the dimensions of the platelets were measured shown in the Figure 4.10**c**. The FIB-SEM statistical distribution of GNPs with average length and width of the flake were found to be 895 ± 298 nm, 387 ± 254 nm respectively in Figure 4.10c. These results agree very well with the previous TEM statistical distribution calculations and indicate that the graphene platelets were indeed embedded in the fibrous structures.

Figure 4.11 shows a focused ion beam milled surface of the graphene loaded phenolic resin fibres. One of the characteristic features of phenolic resin fibres is that they are hollow in nature in some instances compared to completely dense TPU counterparts. As clearly seen from the pictures it was not possible to mill these fibres. Even using the higher beam current (90 nA) the samples could not be milled with ion beam. It is believed that GNPs accommodate the polymer matrix along the fibre drawing direction like the TPU composites.

The etching and removal rate of polymer molecules differ from polymer to polymer. The results indicate that TPU fibres are milled and etched very effectively in ion beam compared to the phenolic resin fibres. It was reported that the etching rate for perfluorinated polymers is 500 - 1000 times higher than the partially fluorinated polymer (Fukutake et al., 2010).

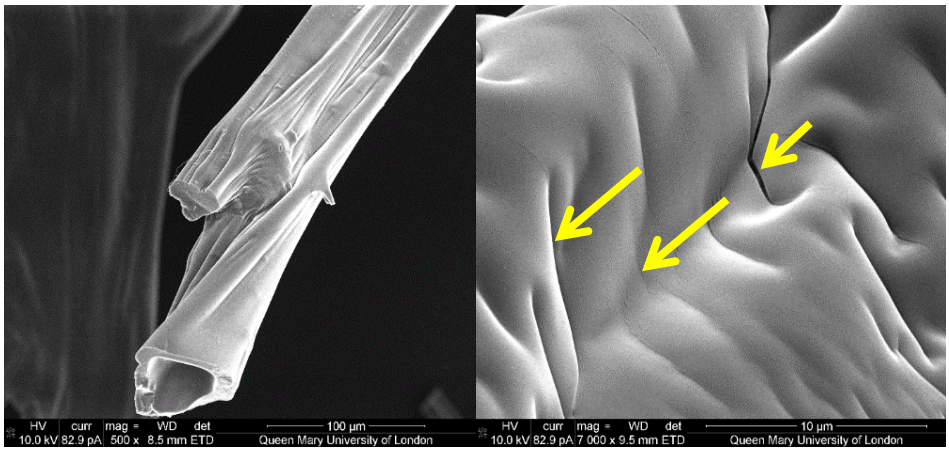

(a) (c)

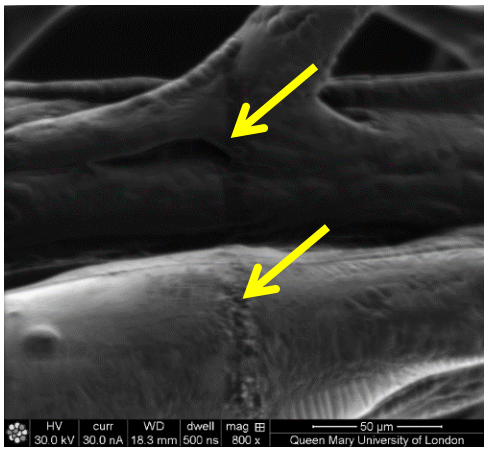

(b)

Figure 4.11 FIB-SEM images of graphene loaded phenolic resin fibres; (a) graphene loaded phenolic resin hollow fibre, (b) specimen after higher beam current used to mill the fibre and (c) crazing effect at the fibre surface

In general, such polymers are degraded very effectively by gamma/electron beam radiation under vacuum at ambient temperatures. The degradation of the polymer is associated with the physical sputtering of Ga^+ ions and the chemical reactions induced by the secondary electrons due to Ga^+ ions. Therefore, in TPU fibres the main-chain scission occurs through dissociative electrons.

On the other hand, in phenolic resin fibres the main-chain scission is limited and hence decomposition of molecules is limited. Therefore, the milling and the

etching is markedly affected by the molecular structure of the polymer. Figure 4.11 shows the high magnification image of the ion beam damaged surface of the phenolic resin fibres milled using a higher milling current. It shows the presence of a cracked surface at regular intervals. The characteristic pattern consisting of regularly spaced cracks perpendicular to the sliding direction has been previously observed in thermoset polymers sliding against smooth surfaces. Evidence of crazing can also be observed, which is normally expected in polymers subjected to sliding wear conditions (Betancourt, Cruz, & Toro, 2011).

4.5 Water soluble polymer as binder study

Water-based polymers are great for applications where the nanofibers are used as a carrier for later release. Water soluble polymers such as polyvinyl alcohol (PVA) and polyvinyl pyrrolidone (PVP) has been tested as quick release agents for oral drugs. High surface area of nanofibers encourages faster dissolution of the polymers compared to cast films. In air filtration, electrospun polyvinyl alcohol (PVA) which is water soluble is commonly used for this application. An obvious advantage of using water-soluble polymers in electrospinning is that the vaporized water is non-toxic to humans and the environment when discharged.

Thicker coatings (double-layer graphene or more) are ideal for hydrophobic applications, such as medical equipment and electronic components (Munz et al., 2015). On the other hand, single-layer graphene coatings could be used where a hydrophilic surface is required, as for example in anti-fog glass and

coatings for buildings. PVP was used to act as a modifier for improving the adsorption of GO onto the nanofibres via strong π-π interactions (Navarro-Pardo, Martinez-Hernandez, & Velasco-Santos, 2016).

4.5.1 Rheology of PVP

Flow curves of PVP-GNP polymer solutions in water are shown in Figure 4.12.

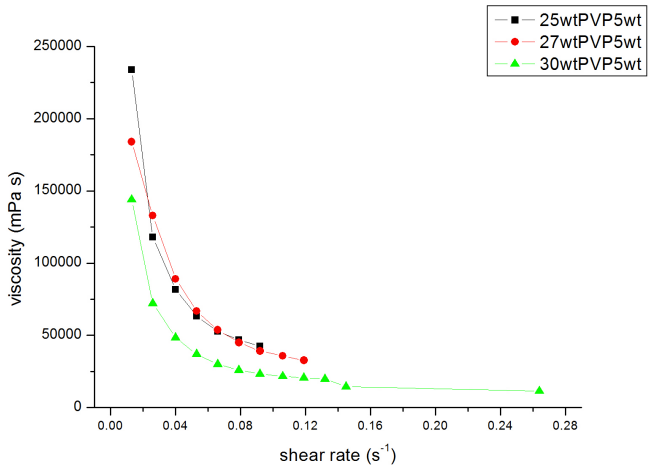

Figure 4.12 Flow curves of the various PVP-GNP polymer solutions in water at ambient temperature

All curves showed non-Newtonian behaviour and the apparent viscosity decreased with increasing polymer concentration. However, it was not possible to measure the viscosity of the 25 wt% solution as it exceeded the measurable range of the rheometer. Adding GNP's to the 27 wt% and 30 wt% PVP solution reduced the viscosity value to within measurable range.

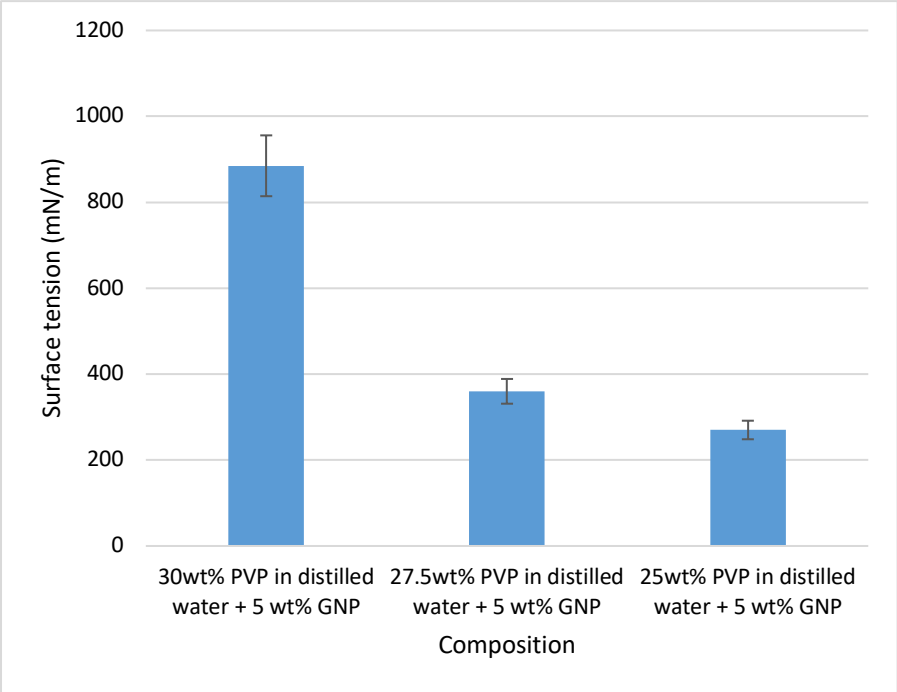

Figure 4.13 Surface tension of PVP loaded GNP

Shear thinning is apparent in all solutions and rheological data obtained was analysed using the Ostwald-de Waele model, $\sigma = k\dot{\gamma}^{n-1}$, where σ is the shear stress, $\dot{\gamma}$ is the shear rate. The increase in concentration of polymer showed significantly more shear thinning behaviour in all PVP solutions (low n value). Randomly oriented, well-dispersed platelets would be expected to percolate at lower concentrations than aligned, well-dispersed platelets (Potts et al., 2011). Study of rheology is important not only for the understanding of processing operations but it may also be used to examine nanocomposite microstructure.

It is worth mentioning that the fibres did not survived during pyrolysis. This might be because the bonding is weaker even though both solvents had polarity. Methyl groups on the substituted ureas appear to be solvated equally and independently compared to water (Spencer & Hovick, 1988)

4.6 Performance assessment of melt compounded PMMA and TPU loaded with GNP nanofibres

Melt compounding is rapid, environmentally friendly, and inexpensive. This will add flexibility, as nanocomposites with desired performance characteristics will be prepared where and when needed (Utracki, Sepehr, & Li, 2006). The melt-compounding process is attractive because of its potential commercial application. They can be polymerised to form polymer chains within the interlayers, and exfoliated nanocomposites are generally obtained.

Incorporation of graphene nanoparticles may lead to significant improvement in properties due to the physical presence of the reinforcing nanoparticles. Moreover, some polymeric matrices such as thermoplastic polyurethanes (TPUs) may also exhibit significant changes in their morphology, including the soft and hard domain sizes, the nature of domain interface as well as the distribution of hard segments in the soft segment phase, all of which altering the material properties (Araby et al., 2013; Yuan et al., 2017a).

The goal of this study is to demonstrate a uniform solution prior to processing of fibre production. The fibres are made from TPU-GNP components targeting to have a uniform structure in the fibre composites. The ability of these fibres is demonstrated with characterisation of their physical and mechanical properties.

The viscosity of the TPU/GNP solutions in Chapter 4 showed that they were too viscous and maybe there will be some non-uniform solutions. Manchado et al.

(2005) found that CNTs could be dispersed uniformly in PP by shear mixing, at minimum low filler loading, and they found that by adding 0.25–0.75 wt. % CNT into PP increased its tensile strength and stiffness as well as storage modulus considerably. In general, the dispersion coefficient increases with shear stress.

Degree of dispersion can be controlled both by the processing conditions and by matching the interaction of organo-modified clay to the polymer matrix. In the case of conventional processing by melt blending (which is a preferred method from the practical view point) using different mixers or extruders, shear forces generated during the processing and the time of the operation will affect deagglomeration and then dispersion of silicate nanoplatelets in the polymer matrix (Pluta, 2006).

4.6.1 Formation of dual polymer TPU/PMMA loaded GNP studies

The possibilities of producing porous fibres loaded with GNP's were anticipated. Combination of PMMA and TPU was used to prepare the fibre in exploitation of properties of TPU that has excellent dimensional stability, good dynamic mechanical behaviour, outstanding abrasion resistance, chemical and corrosion resistance, and a wide range of mechanical strength and toughness (Badamshina et al., 2013).

Meanwhile PMMA, known for transparency and low optical losses, as well as high durability and no toxicity (Prado et al., 2017), has characteristics of being thermoplastic that enables its combination with TPU thus, being the main motivation of this dual polymers combination work. Melt compounding of TPU

and PMMA loaded with GNP's can potentially lead to new separators or filters with enhanced microstructure, porosity and electrochemical properties that cannot be achieved by single-component polymer fibres. Usually, porous nanofibers are produced by immersion in a cryogenic liquid to remove solvent from the fibres, (McCann et al., 2006) or by removing other components in the polymer (Qi et al., 2009; Zhang et al., 2010). PMMA/PAN core–shell hollow fibres, and porous thin films were prepared by electrospinning, (Huang et al., 2016) resulting in lower weight loss, higher degradation temperature and higher glass-transition temperature (T_g).

The dispersion of GNPs into polymeric matrices poses significant challenges (Yuan et al., 2017b). For example, GNP surface modification using physical or chemical methods may provide a means to overcome GNP/polymer incompatibility. The GNP incorporation into the molten polymer enabled polymer diffusion between the graphene sheets and improved the state of dispersion (Yuan et al., 2017b).

The surface of TPU PMMA melt compounded as produced in Figure 4.14 showed that the pores on the fibre surface are all circular with small changes in size, 20 -40 nm. The cross section suggests that the nanopores are shallow and are not connected internally with each other, and the fibres are all with solid cores as the graphene nanoplatelets prevent the formation of pores. These mesopores will act as pathways or vesicles to promote transport of adsorptive to the adsorption sites in the microporosity for excellent performance as an electrochemical double layer capacitor.

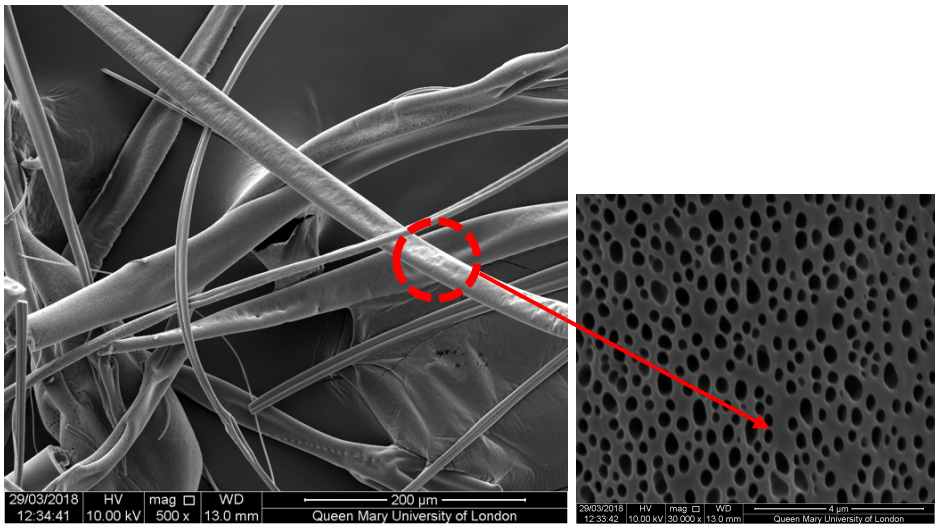

Figure 4.14 10TPU 10PMMA 2GNP melt compounding 36k rpm 0.1 MPa porous fibre

An important characteristic of electrical energy storage in a capacitor is that energy is retrievable in discharge over the same potential range as that required to store the energy on charging, otherwise the energy storage is limited (Lee et al., 1999).

4.6.2 Fibre morphology – surface properties

It has been established that PMMA contributes to the porosity of the fibres. It is clear in Figure 4.15 shows the effects of protrusion by GNP in fibres on cross sectional morphology details of the TPU PMMA is clearly seen.

The GNP sheet is uniformly distributed in the fibre as compounded, especially when compared to TPU fibres which had solid surfaces.

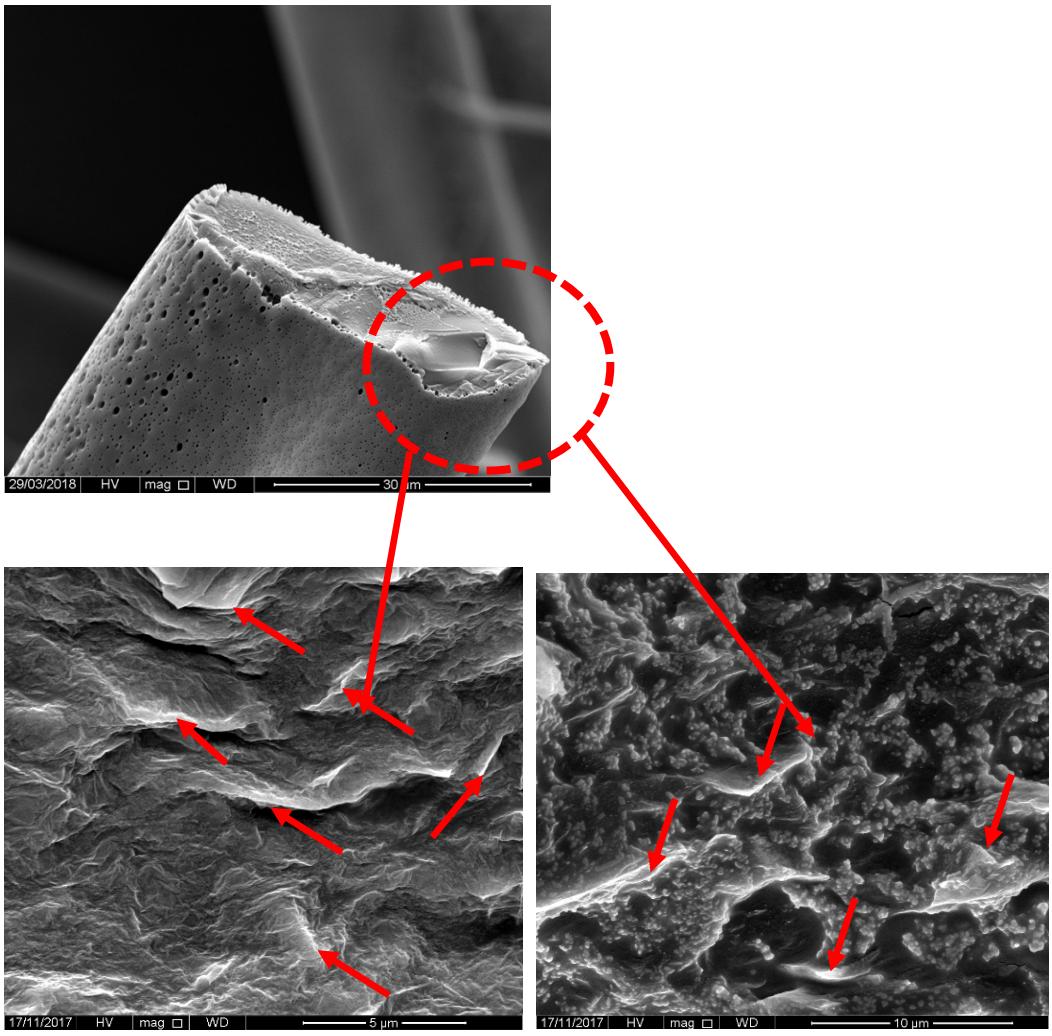

Figure 4.15 Liquid nitrogen used to cut the melt compounded composites showing surface and breakage fraction

The porous structure of PMMA TPU loaded GNP fibers (Figure 4.16) was attributed to the microphase separation structure and the immiscible property between PMMA and TPU.The boundary of PMMA and TPU phases would be formed after DMF evaporation, leading to the porous structure (in Figure 4.16).

Solid smooth fibres were observed in melt compounded 20TPU 2GNP fibres in Figure 4.17. It was expected based on the observation in Section 4.3.1. However, this fibre was successfully pyrolyzed and confirmed that melt

compounding contributes to better and more homogeneous dispersion than vortex stirring techniques. However, TPU PMMA loaded GNP fibre did not survive during pyrolysis because of the porosity structure not strong enough of building scaffold for the fibre to sustain at high temperature.

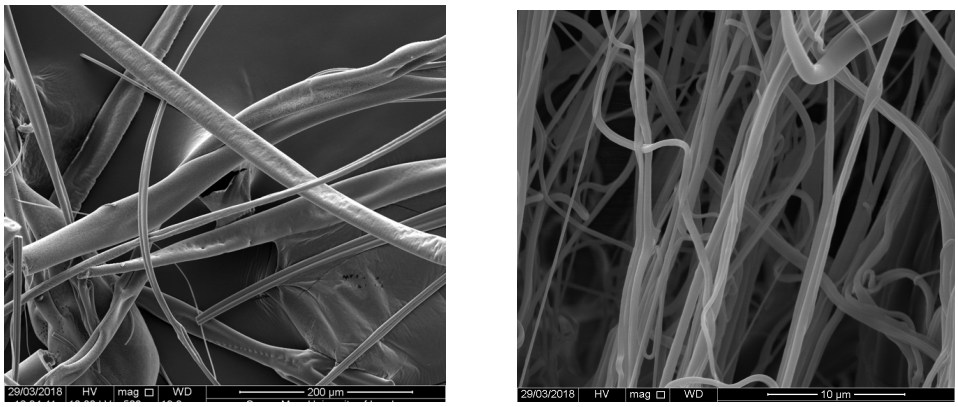

Figure 4.16 a)10TPU 10PMMA 2GNP melt compounding 36k rpm 0.1 MPa b) 20 TPU 2 GNP melt compounding 36k rpm 0.1 MPa

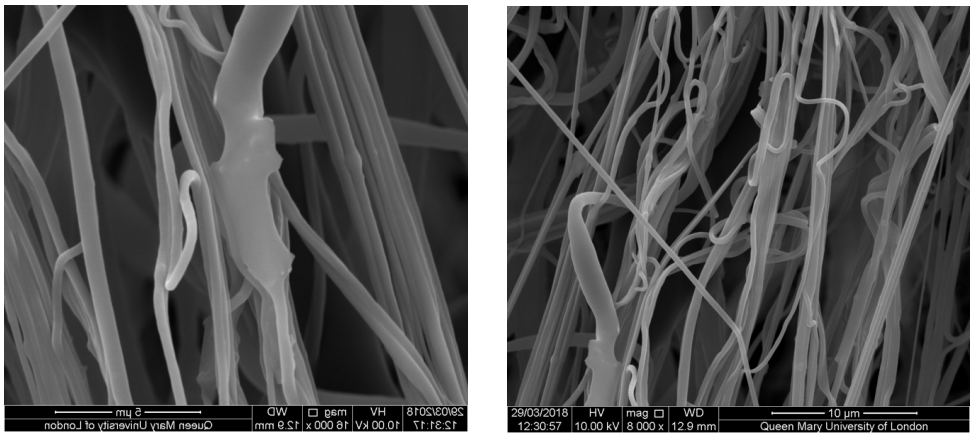

Figure 4.17 20TPU 2GNP melt compounding 36k rpm 0.1 MPa showed the smooth surface of fibre

4.6.3 Conductivity test

Electrical conductivity tests showed that after pyrolysis only 20TPU2GNP melt compounding gave values of 349 S/m. The reduced percentage of GO resulted in conductive GO because increasing GO caused more agglomeration and the graphene form particulate and become insulator.

4.7 Comparison of speed mixer, and vortex followed by magnetic stirring

A study has been done in Figure 4.19 to compare the effectiveness of speed mixing and vortex mixing followed by magnetic stirring. It showed that the speed mixer did not break the polymer chain, hence promoting better solubility of thicker solutions resulted in better yield.

The process also increased the workability solutions which not permit with the old process and unlike sonication where polymer chain break. The fibre produced using speed mixing had better yields, were finer, and more flexible. This encouraged the graphene nanoparticles and graphene oxide powder to embed in the fibres homogeneously.

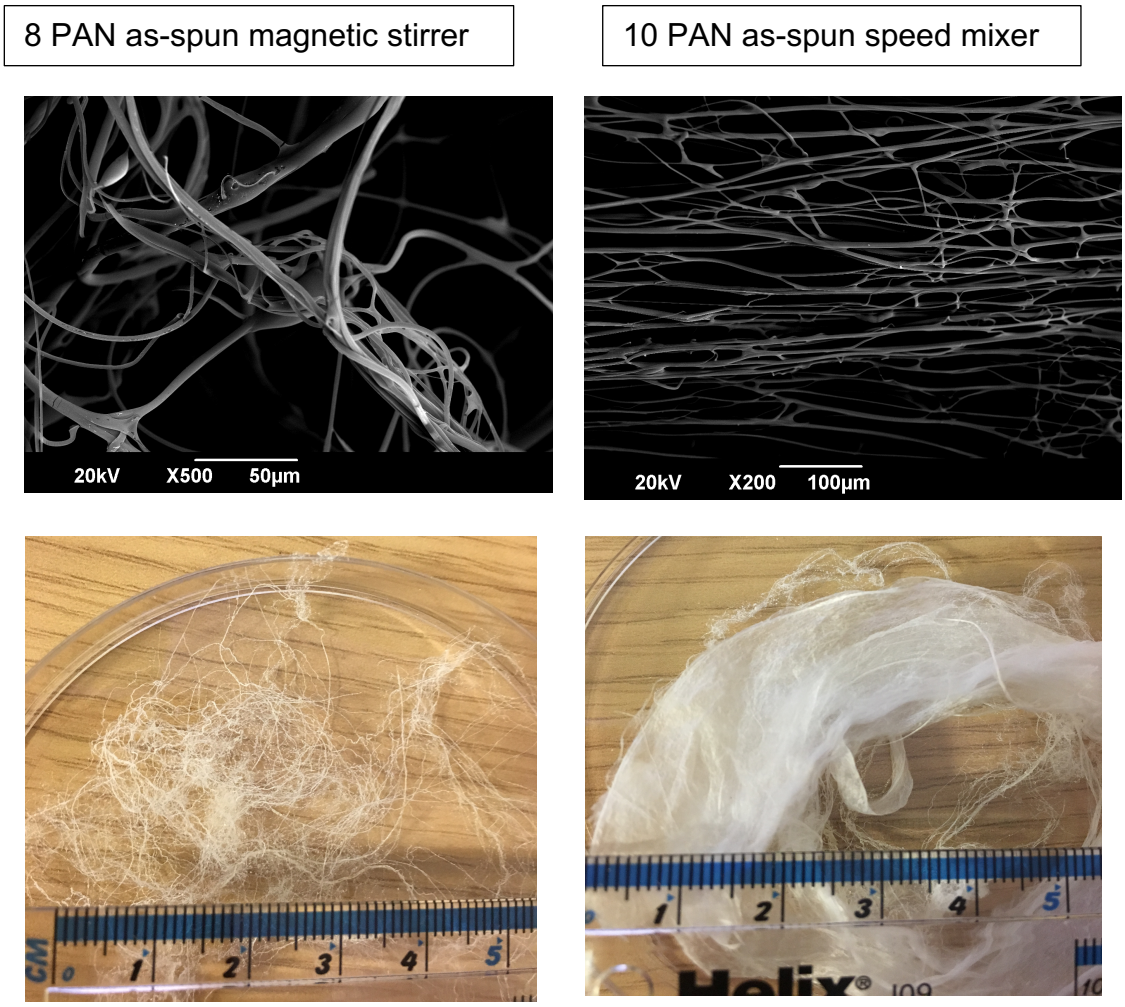

Figure 4.19 Comparison of speed mixer and the vortex mixing followed by magnetic stirring

4.8 Conclusions

Graphene loaded TPU fibres were successfully formed using a pressurised gyration process. The process makes use of simultaneous centrifugal force and dynamic fluid flow to jet the fibres before evaporation of the solvents to form the composite fibre. The fibre diameter generated was in the range of 800–6000 nm. The forming process conditions such as vessel rotating speed, working pressure

and the polymer concentration used, had a significant effect on fibre diameter. The fibre diameter increased with increasing weight percentage of phenolic resin and TPU polymer. The use of higher working pressures resulted in reduced fibre diameter. However, for the highest rotational speed there is no fibre produced. FTIR and Raman spectroscopy analysis confirmed the various bonding characteristics of the hybrid composite fibre structures. Focussed ion beam milling and etching verified the effective incorporation of graphene nanoparticles into the fibre composites.

Chapter 5 Preparation and characterisation of PAN-based carbon nanofibres with spark plasma sintering

5.1 Introduction

Polyacrylonitrile (PAN) fibres containing various concentrations of graphene nanoplatelets (GNPs) have been prepared by pressurised gyration, and carbon nanofibres (CNFs) have been obtained after subsequent heat treatment and spark plasma sintering (SPS). The influence of processing parameters such as rotational speed, working pressure, carbonization and SPS temperatures on the diameter of the nanofibres were studied. Furthermore, the thermal properties, morphologies, and crystallization properties of the CNFs have been investigated by using thermogravimetry, scanning and transmission electron microscopy, and Raman spectroscopy. Also, the electrical conductivity and mechanical properties of these samples was studied. The results suggest that the gyration conditions and the loading concentration of the GNP significantly modified the characteristics of the nanofibres.

5.2 Fibre diameter distributions

Figure 5.1 illustrates the statistical distributions of the PAN-based fibre samples with 0, 1, and 8 wt% of GNPs prepared under different processing conditions, categorized as follows: as-spun, pyrolyzed, and after-SPS samples. With regard to the influence of the GNP concentration, it can be seen that the difference in the mean diameter becomes wide in totality, especially for the as-spun samples, even though it appeared to be narrower at first and then wider, when increasing

the concentration of GNPs from 0 to 1 wt% and then to 8 wt%. This could be due to differences in the viscosity of the feed stock solution and the uniformity of the GNP distribution in the PAN solution. The GNPs were dispersed well in the solutions when the concentration is low (1 wt%); thus, the differences in the diameter of these samples are narrower than the others. On increasing the content of GNPs, the solution became denser and some agglomeration of GNPs took place, thus worsening the dispersion. As a result, the diameter difference became larger again as the concentration of GNPs increased to 8 wt%.

It can also be seen in Figure 5.1 that the largest statistical variation in the diameter for a particular GNP content is for the as-spun samples. After carbonization, the statistical difference in the diameter of the fibres became narrower, especially in the samples with GNPs of 1 and 8 wt% (Figure 5.1**-2, c-2**). Furthermore, after SPS the statistical difference in diameter of the pyrolysed samples further decreased, especially in the samples with 0 and 1 wt% GNPs (Figure 5.1**a-3, b-3**). The narrow diameter distribution indicates the uniformity in pyrolyzed and SPS samples, which is mainly attributed to the solvent and residue evaporation. Generally, a decrease in this trend is observed for fibre diameter of the as-spun, pyrolyzed and after-SPS samples. For example, the average diameter of pure PAN fibres changed from 3.21 to 2.44 μm from as-spun to pyrolyzed conditions. This change can be observed more clearly and intuitively from Figure 5.2.

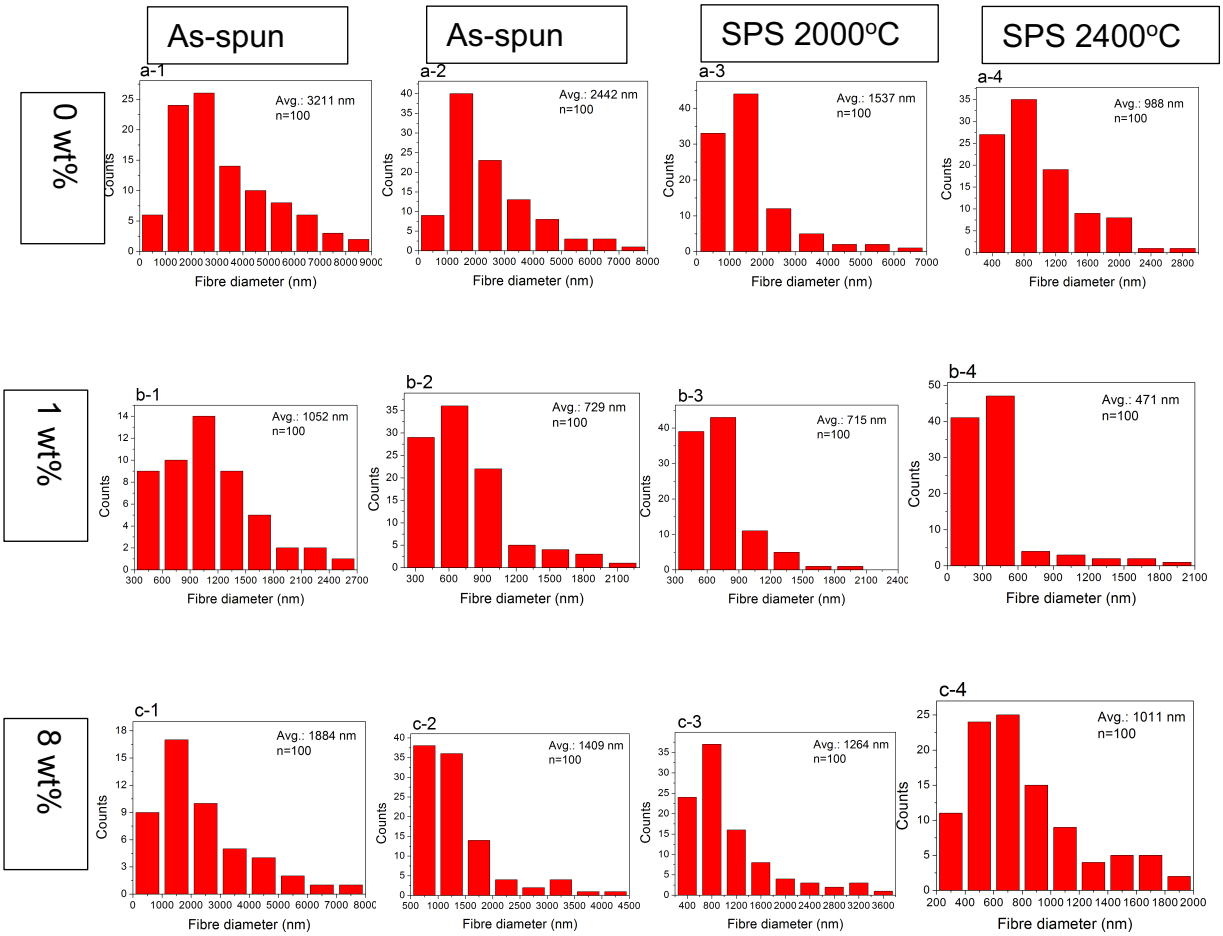

Figure 5.1 Diameter distributions for PAN-based fibres with various GNPs concentrations (a) 0 wt%, (b) 1wt%, (c) 8wt% under different conditions (1, as-spun;2, pyrolysed;3, SPS at 2000 ºC;4 SPS at 2400ºC). n denotes the number of samples analysed.

Figure 5.2 shows the difference in fibre diameter between the as-spun, pyrolysed, and after-SPS samples at different temperatures during the SPS processing. It can be clearly seen that the average diameter of the PAN-based fibres decreased gradually after the carbonization and SPS processes regardless of the GNP concentration. The average diameter of the fibres without GNPs decreased from 3.51 μm to 2.44 μm after the carbonization process at 900 °C, and then to 1.54 μm after SPS treatment at 2000°C. Also, as the SPS treatment temperature increased from 2000 °C to 2400 °C, the average fibre diameter decreased further from 1.54 μm to 0.99 μm. Similarly, for the samples

with 3wt% GNPs, the average fibre diameter decreased from 2.79 μm to 2.12 μm after the carbonization process at 900 °C, and then decreased to 1.38 μm and 0.98 μm after SPS treatment at 2000 °C and 2400 °C, respectively. This result can be explained by the fact that, shrinkage took place in the fibres during the high temperature heat treatments due to decomposition reactions. Moreover, one can observe in Figure 5.2 that on increasing the concentration of GNPs the average fibre diameter decreased first and then increased, irrespective of the processing conditions of the fibres.

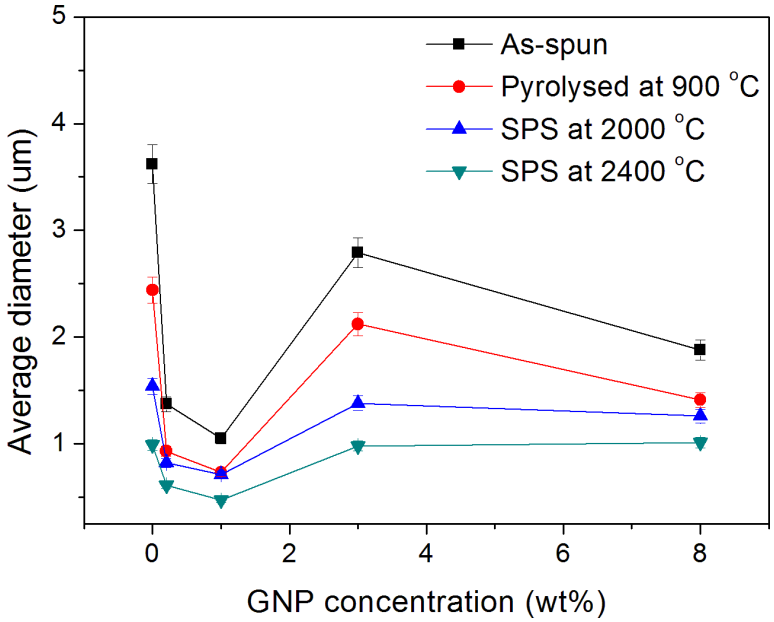

Figure 5.2 Average fibre diameter for as-spun, pyrolysed, and SPS treated samples at different temperatures with different concentration of GNPs.

This can be the result of the uniformity of additive as well as the viscosity of the solutions. Consequently, the average diameter of as-spun, pyrolysed, and SPS treatment at 2000 and 2400 °C resulted in finer fibre diameters of 1.05, 0.73, 0.71, and 0.47 μm, respectively, at a GNPs concentration of ~1wt%.

The rotational speed and working pressure of gyration were varied to study the effect on the average diameter of the fibres. Figure 5.3 shows the plot of fibre diameter against rotational speed under different working pressures.

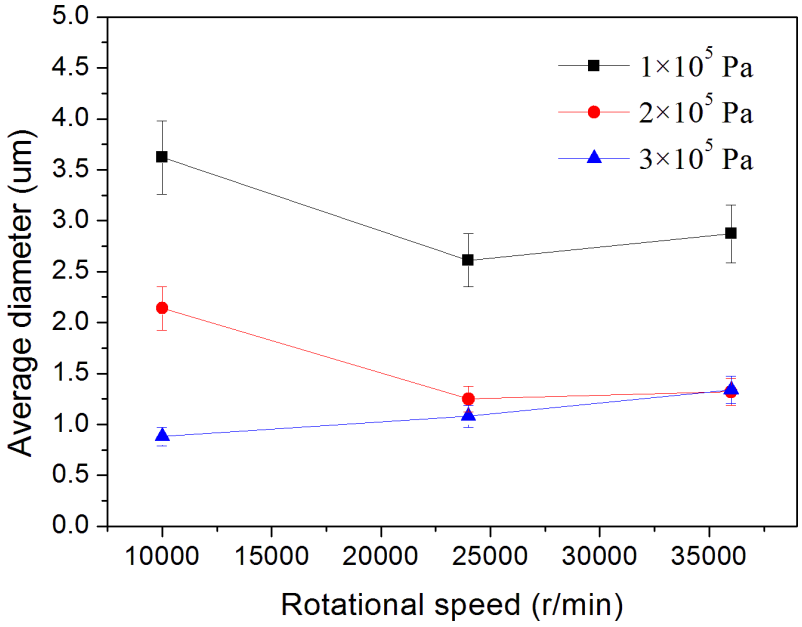

Figure 5.3 Average fibre diameter for as-spun PAN with different rotational speeds and various working pressures.

A substantial reduction in the average fibre diameter was observed by increasing the rotational speed from 10k rpm to 24k rpm at a working pressure of ≤0.2 MPa. Thus, for the samples fabricated at 0.1MPa, increasing the rotational speed from 10k rpm to 24k rpm reduced fibre diameters from ~3.6 μm to ~2.6 μm. Similarly, for the samples fabricated at 0.2 MPa, the fibre diameter decreased from ~2.15 μm to 1.25 μm. However, with further increase of the rotational speed from 24k rpm to 36k rpm there was not a significant decrease, but actually a slight increase in diameter of fibres compared with the former. In comparison to previous results for pure polymer (Mahalingam & Edirisinghe, 2013), there is a slight deviation of

trend, but the overall tendency of diameter reduction by (initial) increase of rotation speed is similar. As for samples produced with a higher working pressure of 0.3 MPa, the impact of rotational speed on diameter is not significant for the whole range of rotational speeds investigated (10k to 36k rpm).

5.3 Thermogravimetry of CNFs

Figure 5.4 displays thermogravimetric curves and the differential thermogravimetric analysis (DTGA) curves of the pure PAN fibre and PAN-GNPs fibre with 8 wt% of GNPs, carried out in a nitrogen atmosphere.

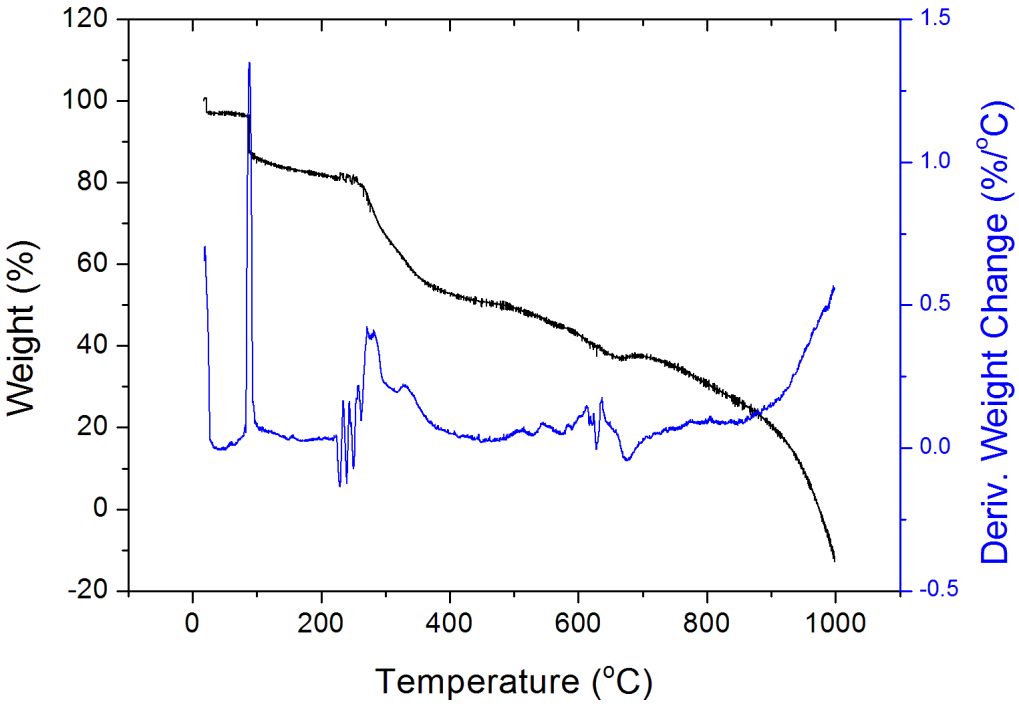

Figure 5.4 TGA and DTGA curves of as-spun PAN-GNPs (8wt%) nanofibres in nitrogen atmosphere.

As observed from the TGA curve, there is a sharp decrease in weight in the temperature range of 80 - 100 °C because of loss of solvent and/or the adsorbed

water molecules in the fibres. Moreover, a large amount of weight loss of PAN-GNPs fibre was observed at ~250 °C, and the weight change of the sample in the temperature range of 270 - 300 °C is 16.1 %, which is mainly due to the decomposition of the fibres (Rahaman et al., 2007).

5.4 Morphologies of PAN-based fibres

The SEM micrographs of as-spun, pyrolyzed, after-SPS PAN-based fibres with different concentration of GNPs are shown in Figure 5.5. It can be seen in Figure 5.5**a-1,b-1,c-1** that the as-spun PAN fibres are distributed randomly and the difference between their diameters is wide, as can be seen in Figure 5.1**a-1**. Moreover, there are some beads within the fibres which were possibly created by the mismatch of viscosity and processing parameters such as rotational speed and working pressures.

As for pyrolysed PAN-based CNFs, there are differences in morphologies of the surfaces of the fibres with different concentration of GNPs. It can be observed in Figure 5.5**a-2,b-2,c-2**, that the surface of the fibres are smooth when the concentration of GNPs is 0 wt% or at a low value (1 wt%). However, on increasing the GNP concentration from 0 to 8 wt%, the surface of the CNF samples becomes increasingly rougher.

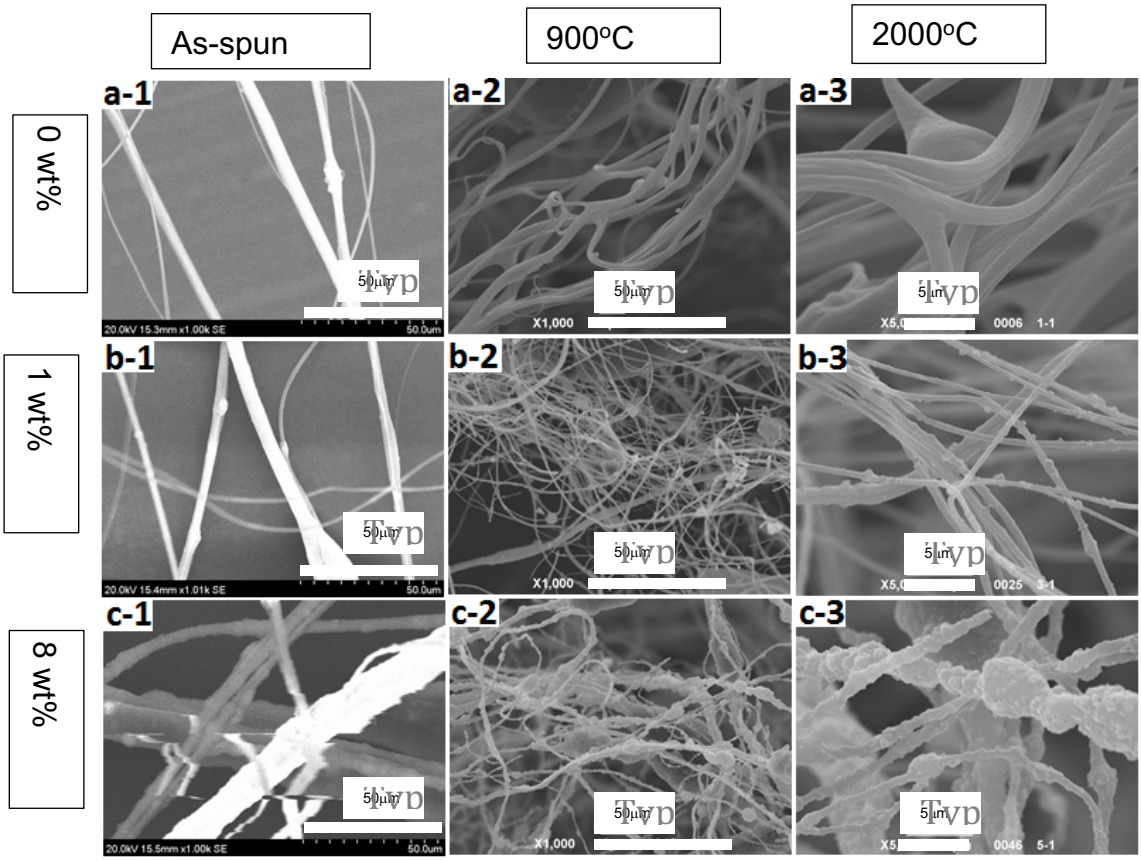

Figure 5.5 Scanning electron micrographs of PAN-based fibres made with various concentrations of GNPs (a) 0 wt%, (b) 1 wt%, and (c) 8 wt% and under different conditions (1, as-spun;2 and 3, pyrolysed).

This change in morphology can be seen more clearly in SEM micrographs at a larger magnification (Figure 5.5**a-3,b-3,c-3**). Furthermore, there are many fine particles with size about hundreds of nanometers on the surface of the fibres when the concentration of GNPs was increased to 1 wt% (Figure 5.5**b-2,b-3**). These particles are GNPs, which will be verified and discussed in detail in Section 5.5. Meanwhile, the diameter of the CNFs decreased initially and then increased (Figure 5.2**)**.

Figure 5.6 shows the SEM study results of CNFs with various GNPs concentrations (0, 1, and 8wt %) after SPS treatment at different temperatures (2000 and 2400 °C). As for the pure PAN carbon fibre samples, it can be seen in Figure 5.6**a** that the SPS processing resulted in a rougher surface of the fibres compared to that of the pyrolysed samples (Figure 5.5**a-3**). The reason for this is that the graphitization takes place at the high temperature of 2000 and 2400 °C [23] during SPS. The amorphous structure of carbon transformed into graphite, partly by heat treatment as well as by thermal decomposition at higher temperatures. Meanwhile, the diameter of the pure PAN-based CNFs decreased, which is shown qualitatively in Figure 5.2.

With regard to the after-SPS CNFs, it can be seen in Figure 5.6 that the SPS processing resulted in a rougher surface of the pure PAN-based fibres compared with those of pyrolyzed CNFs. The reason for this is that the graphitization takes place at a higher temperature of 2000 ^{o}C during SPS (Rahaman et al., 2007). The amorphous structure of carbon transformed into graphite partly by heat treatment as well as by thermal decomposition at higher temperatures, which can be verified by the diffraction patterns of TEM (section 5.5.2).

Meanwhile, the diameter of the pure PAN-based CNFs decreased, which is shown quantitively in Figure 5.2.

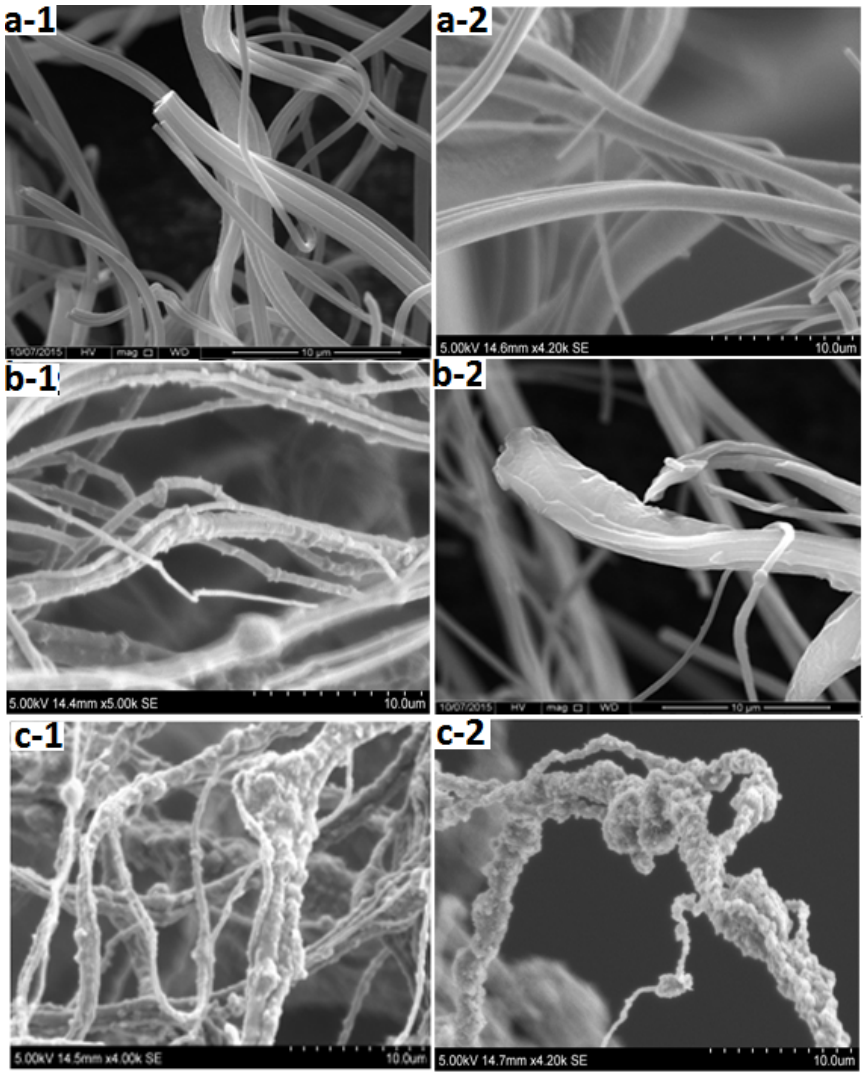

Figure 5.6 Scanning electron micrographs of CNFs at GNPs concentration of 0 wt%(a), 1 wt%(b), 8 wt%(c) after SPS treatment at different temperatures (1, 2000°C; 2, 2400°C).

Furthermore, it can be seen in Figure 5.6**b-1** and **c-1** that the morphologies of the fibres after-SPS treatment at 2000 °C have not produced a significant difference compared to that of the pyrolysed samples (Figure 5.5**b-3,c-3**). This can be attributed to the relatively high temperature of the SPS process. However, with increasing SPS temperature (from 2000 to 2400 °C) the surface of CNFs became smoother again. This result indicates that the GNPs inside and on the surface of fibres grew during SPS processing at high temperature (2400 °C).

Thus, this transformation of structure resulted in some movement of the nanoparticles on the surface of the fibres, and they became smoother compared with before SPS treatment (Figure 5.5**b-3**) and SPS treatment at 2000 °C (Figure 5.6**b-1**).

Concerning the samples with a high concentration of 8 wt% of GNPs, it can be seen in Figure 5.6**c** that the aggregation of graphene still existed after SPS processing. Moreover, the content of graphene as well the degree of graphitization could be improved by the heat treatment at such a high temperature (2400 °C).

5.5 Analysis of crystalline structure of CNFs

5.5.1 Raman analysis of CNFs before and after SPS

Figure 5.7 illustrates the Raman spectra of the PAN-based CNFs with different concentration of GNPs processed under various conditions. The Raman spectroscopy was performed at different locations on each sample to improve the sampling. It is evident that there are two main peaks (D and G bands) at about 1350 and 1583 cm^{-1} due to the existence of a disordered structure and stretching of the C-C bond respectively (Yan, 2014) regardless of the GNPs concentration and forming conditions. However, the differences in the Raman spectra are clearly the existence (or not) of the band around 2680 cm^{-1} which is called the 2D band and the intensity ratio between the D and G bands.

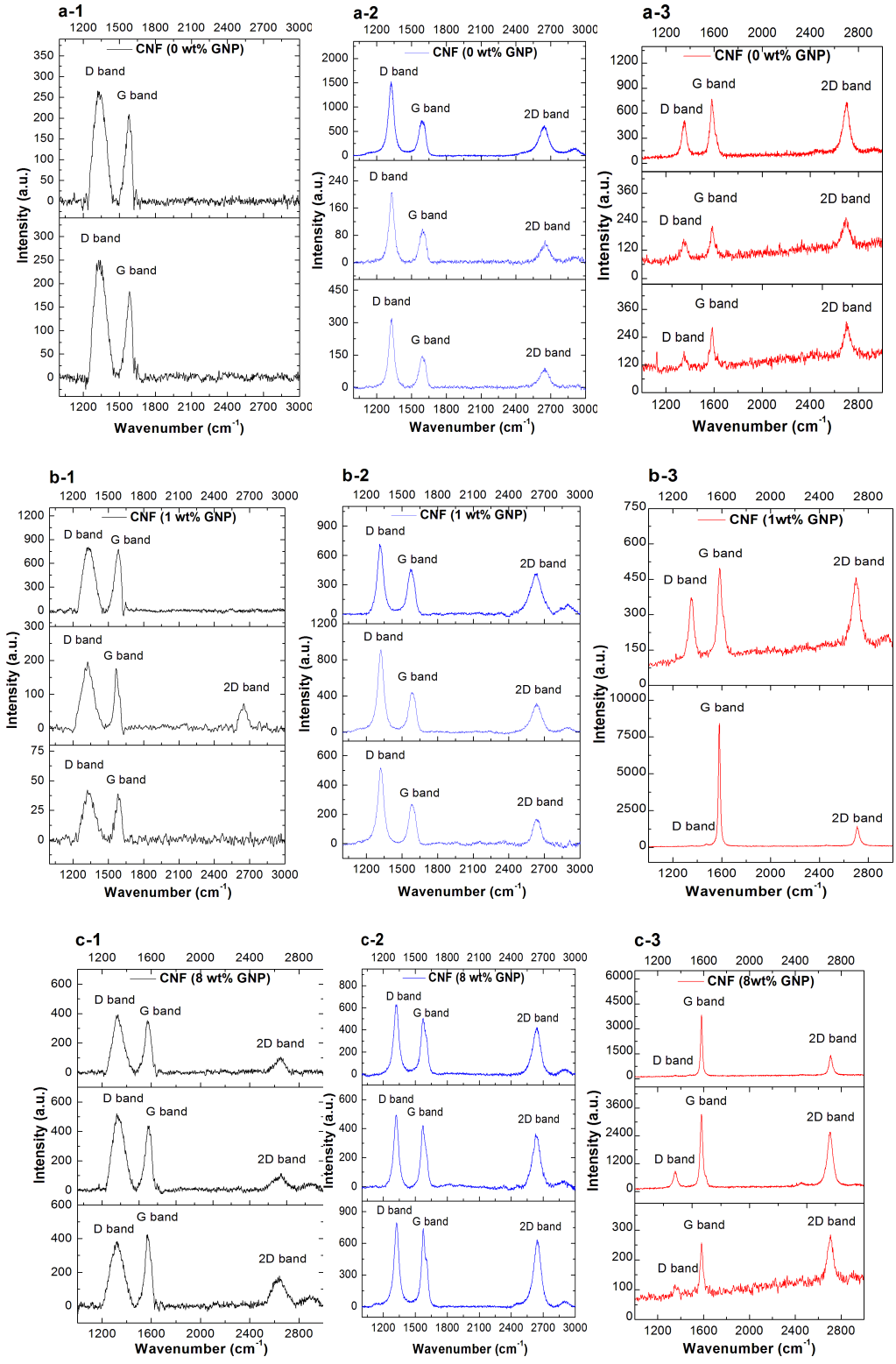

Figure 5.7 Raman spectra of CNF samples with different concentration of GNPs (a) 0 wt%, (b) 1 wt%, and (c) 8 wt% and made under various conditions (1, pyrolysed; 2, SPS at 2000 °C; 3, SPS at 2400 °C). a.u. indicates arbitrary units.

Firstly, in the case of the pyrolysed samples, there is no 2D band in the pure PAN-based CNF sample (Figure 5.7**a-1**), while the 2D band appeared in the spectra of the pyrolysed samples that contained GNPs (Figure 5.7**b-1, c-1**). Combined with the G band, the 2D band is a Raman signature of graphitic sp^2 materials, which indicates that pyrolysed pure CNFs have the turbostratic structure. Moreover, with increasing concentration of GNPs from 1 to 8 wt% the 2D band was detected more prominently and its intensity increased gradually.

For CNF samples made under different conditions, it can be seen in Figure 5.7**a** that the 2D band was observed after SPS treatment at 2000 °C in the Raman spectra compared to that of pyrolysed samples. Moreover, as the SPS temperature increased from 2000 to 2400 °C the intensity of the 2D band increased with increasing graphitization of the fibres. This tendency can also be seen for the rest of the samples containing GNPs. Furthermore, another aspect of SPS treatment of the samples is the change in the intensity ratio of D to G bands in the Raman spectra. The calculated results of intensity ratio of D to G bands (I_D/I_G), and 2D to G band (I_{2D}/I_G) of the different samples are compiled in Table 5.1.

Generally, the higher the D-band intensity the larger the number of defects, and from the double resonance theory, the crystal defect scattered the excited electrons resulting in the wave vector condition, making the intensity of the D-band defect dependent (Dillon, Yudasaka, & Dresselhaus, 2004; Schönfelder et al., 2014). A narrow G band is an indication of higher structural ordering and crystallinity (Schönfelder et al., 2014).

Table 5.1 The intensity ratio between the D-band and the G-band (I_D/I_G), 2D-band and G-band(I_{2D}/I_G) of the CNF samples with various concentrations of GNPs made under different conditions.

Wt.%	I_D/I_G (Pyrolysed)	I_D/I_G (SPS 2000°C)	I_D/I_G (SPS 2400°C)	I_{2D}/I_G (Pyrolysed)	I_{2D}/I_G (SPS 2000°C)	I_{2D}/I_G (SPS 2400°C)
0	1.30,1.37	2.12,2.03, 2.18	0.67,0.76, 0.63	0.01,0.01	0.87,0.63,0.73	0.95,1.16,1.08
0.2	1.16,0.97	1.94,1.75, 1.28	0.86,0.85	0.01, 0.01	0.89,0.81,1.13	1.09,0.97
1	1.04,1.11, 1.01	1.61,2.00, 1.84	0.75,0.03	0.41,0.01,0.01	0.91,0.72,0.65	0.92,0.17
3	1.34,1.16, 1.19	1.52,1.43, 1.38	0.24,0.01, 0.39	0.35,0.17,0.01	0.78,0.62,0.67	0.79,0.89
8	1.09,1.15, 0.83	1.26,1.16, 1.07	0.34,0.27, 0.45	0.31,0.27,0.41	0.83, 0.88, 0.86	0.37,0.77,1.11

Therefore, the intensity ratio of the D-band and the G-band and the shape of these bands can be used to determine the structural ordering in the CNFs. It is clearly seen from the Table 5.1 that increasing the GNPs concentration decreased the ratio of I_D/I_G of the pyrolysed samples indicating greater graphitisation in the samples. It is also true for the SPS treated samples at 2000 °C.

Figure 5.8 shows the dependence of GNP concentration and processing conditions on the I_D/I_G and I_{2D}/I_G ratios. The ratio of I_D/I_G increased after SPS at 2000 °C for all of the samples (different concentration of GNPs from 0 to 8 wt%).

However, the ratio of I_D/I_G decreased when the SPS temperature was increased from 2000 to 2400 °C. The higher processing temperature produced crystallization and ordering of the carbon in the fibres. The I_D/I_G ratio was reported to be inversely proportional to the crystallite size by Tuinstra and Koenig (Tuinstra & Koenig, 1970), and this was later confirmed by Knight and White (Knight & White, 1989). The above results suggest that during the SPS heat treatment at 2000 °C, nanocrystals of graphene nanoplatelets evolved from the amorphous structure. In fact, owing to the dependence of the I_D/I_G ratio on the excitation wavelength, Tuinstra and Koenig's law becomes approximate and cannot apply for a crystallite size below ~10 nm (Mallet-Ladeira et al., 2014). The smaller the volume of the graphene nanoplatelets the larger the I_D/I_G ratio. For example, the I_D/I_G of single-layer graphene is larger than that of double-layer and triple-layer graphene. Nevertheless, nanocrystals would grow resulting in a crystallite size of 10 nm in the SPS processing at a higher temperature of 2400 °C. Consequently, the value of I_D/I_G decreased dramatically after SPS at 2400 °C, independent of the concentration of the GNPs (Figure 5.8**a**). The effect of GNPs content caused the ratio of I_D/I_G to drop with increasing the concentration of GNPs (even though the value for sample with 0.2 wt% GNPs deviated to some extent). This deviation may have been caused by the non-homogeneity of GNP dispersion due to low concentrations. With increasing GNPs, the agglomeration is stronger and the ratio of I_D/I_G decreased.

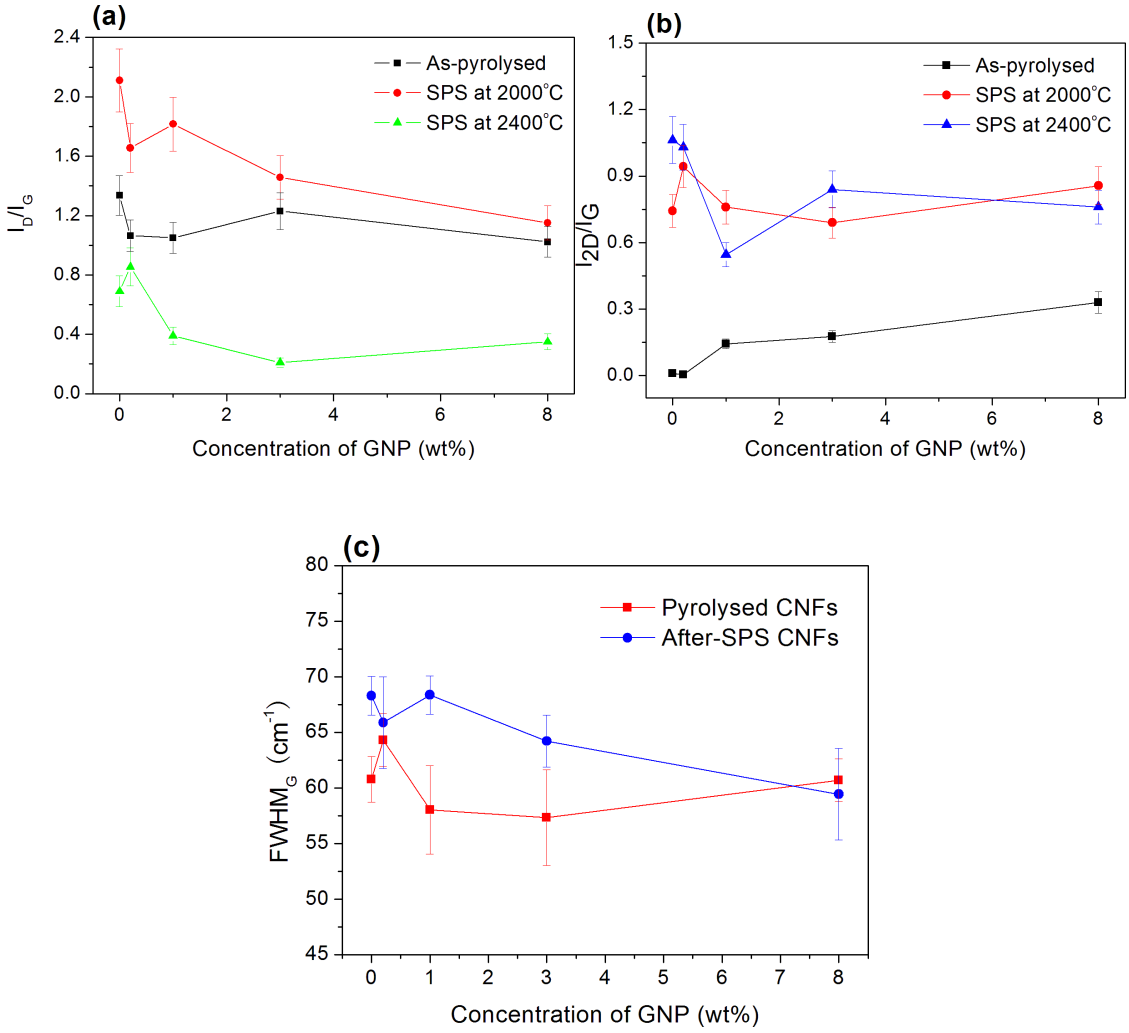

Figure 5.8 Ratio of (a)I_D/I_G, (b) I_{2D}/I_G and (c) $FWHM_G$ of CNF samples with various concentrations of GNPs made under different conditions.

Figure 5.8**b** shows that the value of theI_{2D}/I_G ratio increased after SPS treatment, because post-SPS the degree of graphitization of CNF samples is higher than that of the original samples (pyrolysed). This ratio is widely used to determine the number of graphene layers in the structures (Deng et al., 2014). Actually, the I_{2D}/I_G of multi-layer graphene is larger than that of single-layer graphene. Similarly, there is an enhancement of I_{2D}/I_G for the pyrolysed CNFs as the GNPs added increased from 0 to 8 wt%. The reason for this can be the same as that

for I_D/I_G, resulting from the agglomerate of GNPs which can be verified by the SEM micrographs in Figure 5.6.

Figure 5.8c shows that the Full width at half maximum G band ($FWHM_G$) of after-SPS CNFs is higher than that of pyrolysed samples of up to ~8 wt% of the concentration of GNPs. This can be due to the fact that the higher degree of graphitisation after the high temperature SPS processing produced a high intensity of G band in Raman spectra.

5.5.2 TEM analysis of CNFs with GNPs

Figure 5.9 illustrates the key features of the microstructure of the CNFs determined from TEM images and diffraction patterns with different concentration of GNPs (0 and 8 wt%) after carbonisation as well as SPS treatments. It can be seen that the graphene exists inside the CNFs and can be more easily discerned at the edges of the fibres (Figure 5.9**c**). The selected area diffraction shows the crystallinity of the CNFs. From the diffraction patterns, the ordered graphitic layers present in the CNFs after carbonization treatment, especially after SPS at 2400 °C, can be clearly seen. The diffraction planes in the fibres are identified as [002], [100] and [004], from the inner circle to outer circle, respectively (Fan et al., 1998). Even though there is no graphene in the pure PAN-based CNFs, diffraction patterns emerge after SPS at 2400 °C (Figure 5.9**d**), which indicates that nanocrystallites of graphite are formed at high temperatures. These results are consistent with the Raman results (section 5.5.1).

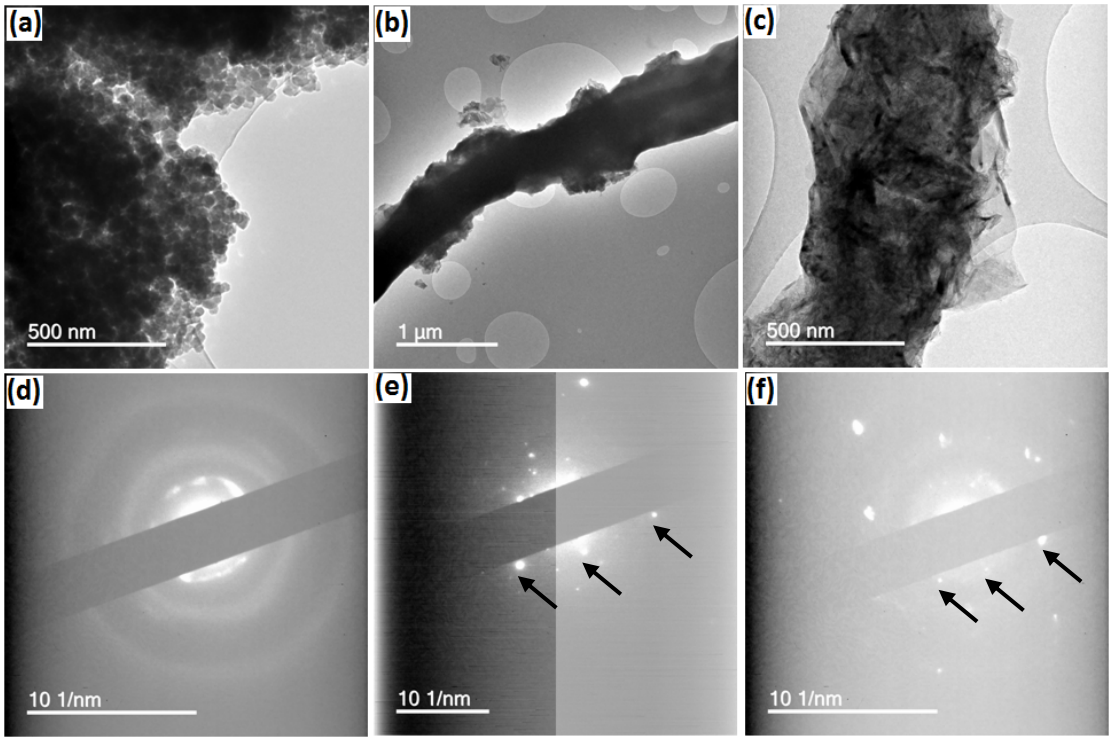

Figure 5.9 Transmission electron microscope images and diffraction patterns of CNFs (a) and (d) pure PAN-based CNFs after SPS at 2400 °C; (b) and (e)8wt% of GNPs after carbonization; (c) and (f) 8wt% of GNPs after SPS at 2400 °C.

5.6 Electrical properties of CNFs

Figure 5.10 shows that the electrical conductivity of CNFs made under different conditions are dependent on the concentration of GNPs. Increasing the loading of GNP caused the conductivity of the CNFs to increase gradually no matter how they were prepared (Figure 5.10**a**). Figure 5.10b shows a typical SEM image of the fracture surface after bending tests which was used for determining the cross-sectional area of CNFs. The value of electrical conductivity of as-spun PAN-based fibres increased from ~4 to ~46 S/mm when increasing the GNP loading content from 0 to 8 wt%. Similarly, that of pyrolysed CNFs increased from ~36 to ~193 S/mm as the concentration of GNPs increased from 0 to 8wt%. Most

strikingly, for a similar increase in GNPs, the increase in the electrical conductivity of the CNFs after SPS at 2400 °C was ~179 to ~272 S/mm. The increase in electrical conductivity of the pyrolyzed and SPS samples indicates that the degree of graphitization is higher in these samples than that of as-spun PAN fibres. This validates the Raman and TEM data showing nanocrystallites of graphites formed at higher temperature, which act as effective electron carriers.

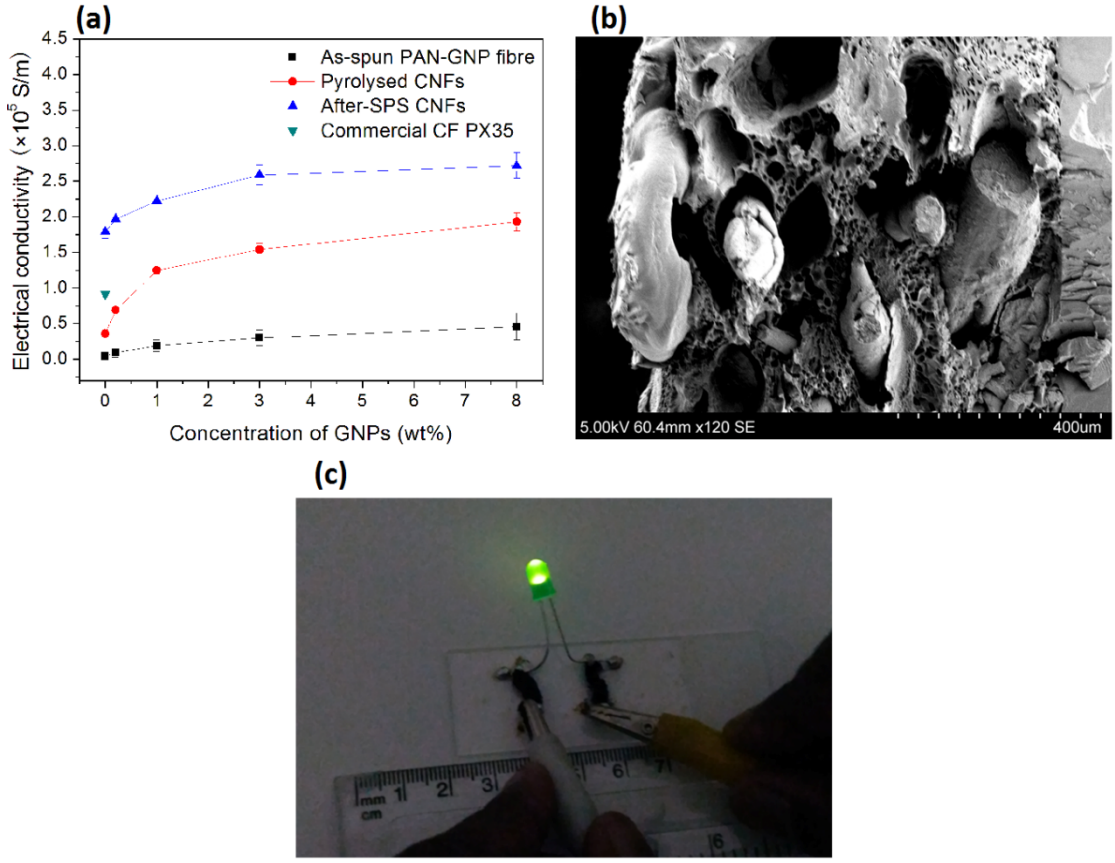

Figure 5.10 Electrical conductivities of CNFs prepared in this work (a) conductivity dependent on the concentration of GNPs (b) typical scanning electron micrographs of fracture surface of CNFs/PVA composites (c) demonstration of performance in an activated electrical circuit of pyrolysed CNFs

Figure 5.10**c** demonstrates the conductivity of the fibres very clearly, where a LED lights-up when connected in close-circuit using pyrolysed samples, even

before SPS. Thus, these samples have the potential of making conductivity bridges for electrical engineering applications.

5.7 Mechanical properties of CNFs

The presence of the 2D-band in the Raman spectra of the samples provides an opportunity to study the mechanical properties of the CNFs produced in this work because this band position in the spectra is very sensitive to deformation. Figure 5.11 shows the deformation-induced shifts in the position of 2D-band during four-point bend tests of the CNF composites (pyrolyzed CNFs). It can be seen that the band position of the CNFs decreased with tensile deformation; the higher the deformation the higher the peak shift. The rate of Raman shift with respect to strain was obtained by fitting the data linearly in the strain range measured. This value was found to be -0.037 cm^{-1}. It was reported that the rate of 2D Raman shift can be related to the modulus of the CNFs (Cooper & Young, 2000). There exists a universal calibration of -0.05 cm^{-1}/GPa for the stress induced shifts of the 2D-band of CNFs pyrolyzed at 1000 ^{o}C. This calibration has been extensively used to obtain the modulus of graphene and carbon nanotubes (Deng et al., 2011). Under this assumption, the calibration is also valid for the CNFs in this work, the modulus of the CNFs is 74 GPa. This value is in agreement with those reported in the literature for cellulose based carbon fibres (Peng, Shao, & Hu, 2003) but is substantially higher than that reported for carbon fibres derived from micron-sized cellulose fibres (Kong et al., 2012), which is 40 GPa.

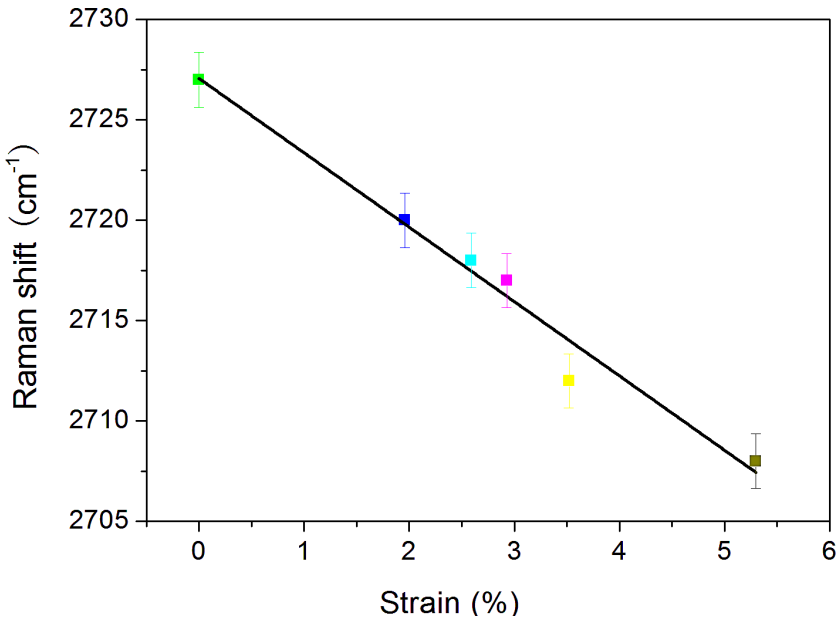

Figure 5.11 Mechanical property relationship between Raman shifts versus strain of CNFs made in this work obtained using 4-point bend testing and Raman spectroscopy

5.8 Conclusions

Carbon nanofibres were obtained by utilising pressurised gyration and high temperature processing. The fibre diameter and distribution is controlled by the key forming parameters of rotating speed, working pressure and the loading concentration of the graphene nanoplatelets. The pyrolysis and the spark plasma temperature influenced the microstructures of the carbon nanofibres. A heat treatment temperature of 2400 °C in SPS produced nanofibres with a high degree of graphitization with properties superior to those of commercial carbon fibres. These nanofibres are useful in advanced engineering applications.

Chapter 6 **Preparation and characterization of GO-PAN nanofibres**

6.1 Introduction

Graphene oxide (GO) fibres are attractive to produce because of their promising multifunctional applications area such as electronic textiles, smart clothing, electronic wire, field emission, chemical sensors, photovoltaics, batteries, fuel cells, sensors, filters in large scale worldwide. The forming process selected was pressurised gyration because it is capable of producing in mass production. Therefore, this project also optimises the processing parameters using pressurised gyration in term of composition, rotational speed, pressure and GO amount. The graphene oxide consisting of 3, 5, 7 and 10 wt% in two different polyacrylonitrile (PAN) concentrations of 8 and 10 wt% were investigated in Table 6.1. Scanning electron microscopy (SEM) was used to observe the fibre morphology. Raman spectroscopy showed that the peak of GO was obtained.

Table 6.1 Generating as spun fibres of 10 wt. % PAN

As-spun fibres	GO concentration	Rotational speed (rpm) vs. Working pressure (x10^5Pa)								
Speed (rpm) vs. Pressure (x10^5 Pa)		10k			24k			36k		
		1	2	3	1	2	3	1	2	3
27.3	3	X	X	/	/	/	/	/	/	/
38.5	5	X	/	/	/	/	/	/	/	/
46.7	7	/	/	/	/	/	/	/	/	/
55.5	10	/	/	X	/	/	/	/	/	/

X means no fibre produced or polymer spraying
/ means fibre was produced during the pressurised gyration process

6.2 Characterisation

6.2.1 Average fibre size & size distribution

Scanning electron microscopy (SEM) images of the GO-PAN fibres are given in Figure 6.1 below. The SEM images show that all the composite fibres were cylindrical, with rough surfaces and some flaky particles visible. This indicates that GO particles were successfully encapsulated homogenously in the polymer. However, when the loading of GO-PAN was increased, the surface of the fibre composites became rougher.

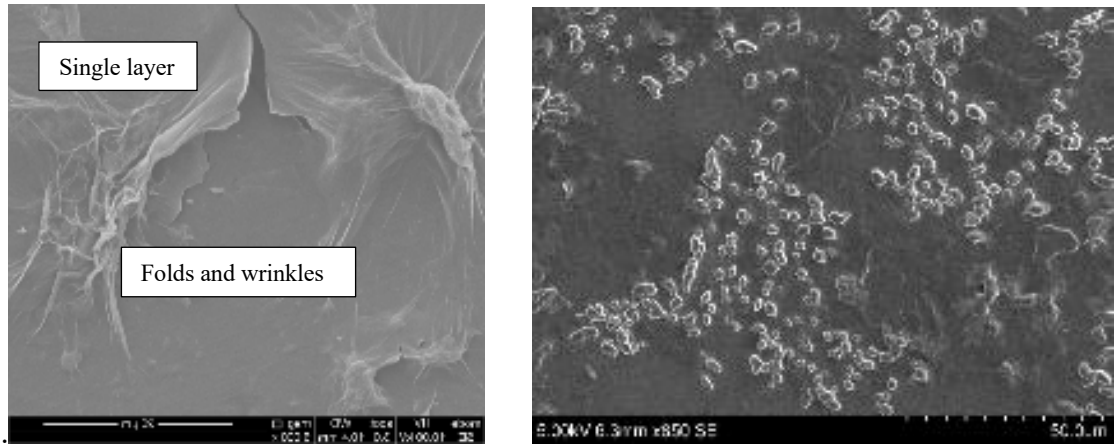

Figure 6.1 SEM images of a single and double GO layers

The size distributions of graphene oxide have been studied. The particles were spread evenly along the fibres. Figure 6.1 shows a topographic image of a single and double GO layers are shown. Figure 6.2 shows the particle size distribution of GO in the fibres. Thicker GO sheets ranging from 2 nm to 60 μm are observed.

Figure 6.3 is shown together with the height profiles taken along a green lines marked (i) and (ii). The scale (i) crosses a single step, the height of which is

around 0.8 nm. The scale (ii), on the other hand, crosses over the folds of GO sheets or the wrinkles on the GO surface, the height of which reaches a few nanometers. The current image of the same area, which was measured at a bias voltage of 5 V, is shown in Figure 6.3. Brighter areas correspond to higher electric current, in which the boundary between a single and double layer is seen. It is noted that the spatial resolution in the current image is as high as that in the topographic image.

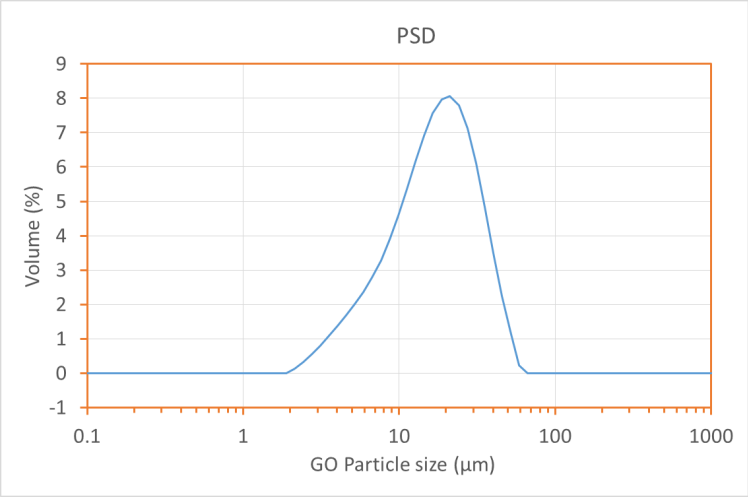

Figure 6.2 GO particle size distributions

The contrast in the current image can be controlled by the applied voltage, taking account of the GO thickness. This means that the current does not diffuse parallel to the GO sheet beyond the lateral resolution (less than 0.05 µm), which is in close agreement with the fact that the as-grown GO is insulating for the electric field parallel to the sheet (Kanamori, Obata, & Saiki, 2011).

The AFM analysis is of particular interest for understanding the sheet depth. Single layers of graphene oxide are just less than 1 nm tall, with greater depths

informing the analyst approximately how many layers are stacked on top of one another. A few sheets stacked on top of one another can indicate that the graphene oxide is not sufficiently dispersed into monolayers or that the graphite was not fully oxidised to enable all single layers to form. The AFM analysis of GO graphene oxide has shown a sheet depth of around 2 nm, proving that the individual flakes are only two graphene oxide sheets tall.

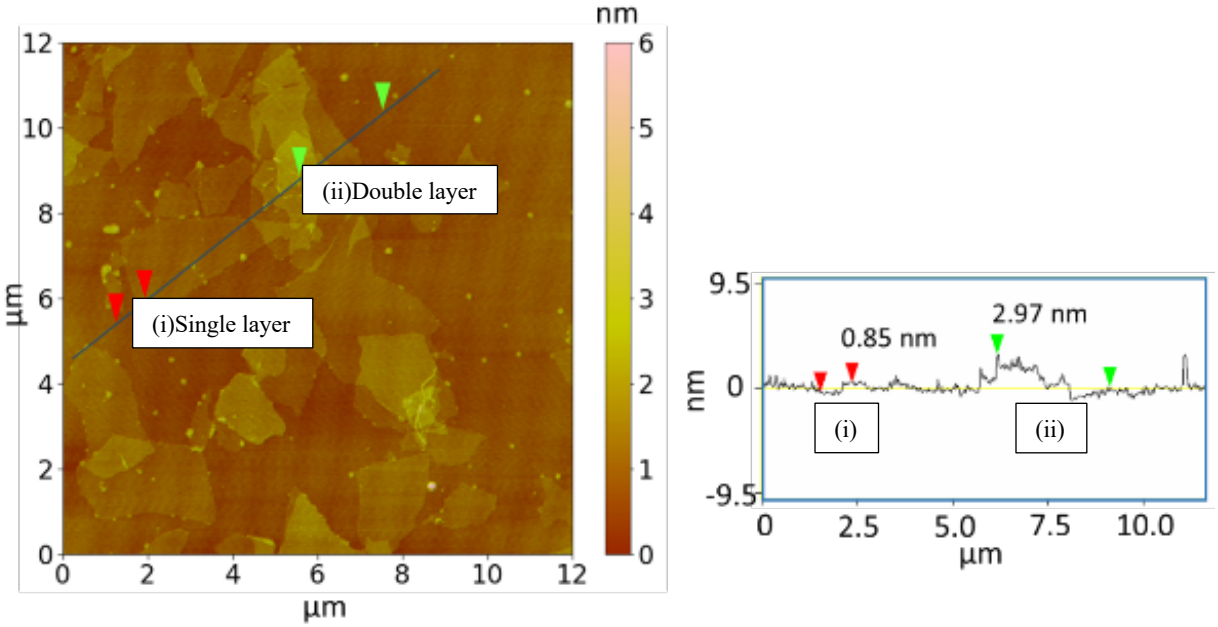

Figure 6.3 AFM and the height profiles taken along the dashed lines

6.2.2 Fibre diameter distributions

At the lowest rotational speed of 10k rpm with 8 wt% polymer composition, none of the composition produces fibres, thus exhibiting polymer spraying. It is because the critical minimum rotation speed has not been exceeded, and is too slow for a solution to move to the orifice thus no polymer was accelerated to carry the GO particles and jetting to form fibres.

Table 6.2 Fibre diameter of 8 wt% PAN at various parameters

8PAN	0.1 MPa			0.2 MPa			0.3 MPa		
	10K	24K	36K	10K	24K	36K	10K	24K	36K
3GO	-	3.2 ± 0.96	-	2.38 ± 0.91	-	-	-	20.49 ± 2.45	-
5GO	-	6.56 ± 1.93	5.35 ± 3.45	-	12.26 ± 3.07	16.46 ± 3.16	-	2.77 ± 0.57	2.23 ± 0.57
7GO	-	7.82 ± 2.61	3.79 ± 1.08	-	2.27 ± 0.56	3.15 ± 0.81	3.17 ± 0.77	3.96 ± 1.26	6.54 ± 2.44
10GO	-	6.14 ± 2.25	-	15.37 ± 3.48	16.76 ± 4.99	7.66 ± 2.35	4.73 ± 1.95	9.4 ± 1.59	4.69 ± 1.95

Table 6.3 Fibre diameter of 10wt% PAN at various parameters

10PAN	0.1 MPa			0.2 MPa			0.3 MPa		
	10K	24K	36K	10K	24K	36K	10K	24K	36K
3GO	-	9.35 ± 3.06	6.49 ± 2.17	-	6.84 ± 2.05	5.48 ± 2.24	11.58 ± 4.02	3.16 ± 1.33	5.52 ± 1.63
5GO	-	5.8 ± 1.90	12.76 ± 5.46	4.41 ± 1.76	8.88 ± 3.94	6.43 ± 2.86	3.79 ± 1.22	3.91 ± 1.46	3.75 ± 0.85
7GO	4.2 ± 1.60	1.03 ± 0.62	3.35 ± 0.64	4.52 ± 2.14	3.71 ± 0.85	3.18 ± 0.95	4.37 ± 1.45	4.25 ± 0.62	3.72 ± 0.84
10GO	5.19 ± 1.33	9.54 ± 3.88	7 ± 1.77	4.42 ± 1.32	6.89 ± 2.58	13.98 ± 4.19	-	17.49 ± 4.81	3.69 ± 1.51

Increasing the speed to 24k rpm, all of the solutions formed fibre composites as the centrifugal force exceeded the surface tension percolation threshold of the polymeric solutions, creating a polymer jet which subsequently leaves behind fibres. It is the point of phase transition of surface tension percolation system where the jet formation forming fibres and not spraying.

At 3 wt% GO fibre has the thinnest and most uniform composition. However, increasing the speed to 36k rpm, only 5 wt% and 7 wt% GO formed fibres. It could be due to the sliding of GO platelets when the rotation speed was exceeded.

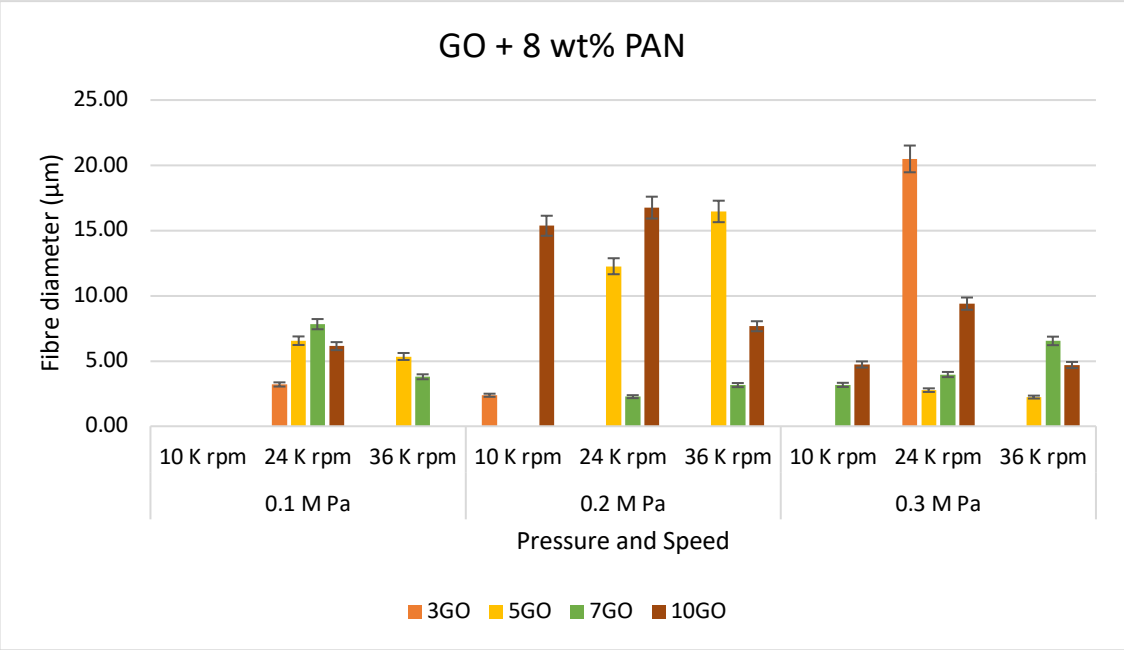

Figure 6.4 Fibre diameter as spun fibre of 8 wt% PAN at different speed and pressure

At pressures of 0.2 MPa with rotational speed of 10k rpm 3 wt% GO compared to 10 wt% has much smaller diameter fibre and uniform. With higher percentage of GO, 7 wt% and 10 wt%, the aggregation of graphene might cause less sliding because steric hindrance at the surface of the graphene sheets inhibits stacking, and stable dispersion inhibits agglomeration. This effect may cause a reduction in surface tension and increased viscosity and polymer entanglement.

The 8 wt% PAN-based fibres had mean diameters of 7.26 μm. The fibre diameter hence shows a gradual decrease in GO content, but the size distributions also broaden. Similar trends are seen with 10 wt% PAN which has mean diameters of 6.20 μm.

The external driving force is the gravitational force when a polymer drop emerges from the orifices (Mahalingam & Edirisinghe, 2013) because surface tension

inclined along the liquid-air interface separates the drop from the surrounding air. Fibre formation from this process starts with a jet emerging from the orifice on the face of the vessel. The jet further stretches due to the centrifugal force and the pressure difference at the orifice. Finally, the evaporation of the solvent leads to thinning of the fibres formed. The reason for only jet formation instead of droplets in this surface instability is viscoelasticity of the polymer solution used (Mahalingam & Edirisinghe, 2013). From this observation, most of the solutions did not produces fibres at 3 wt% GO 8 wt% PAN.

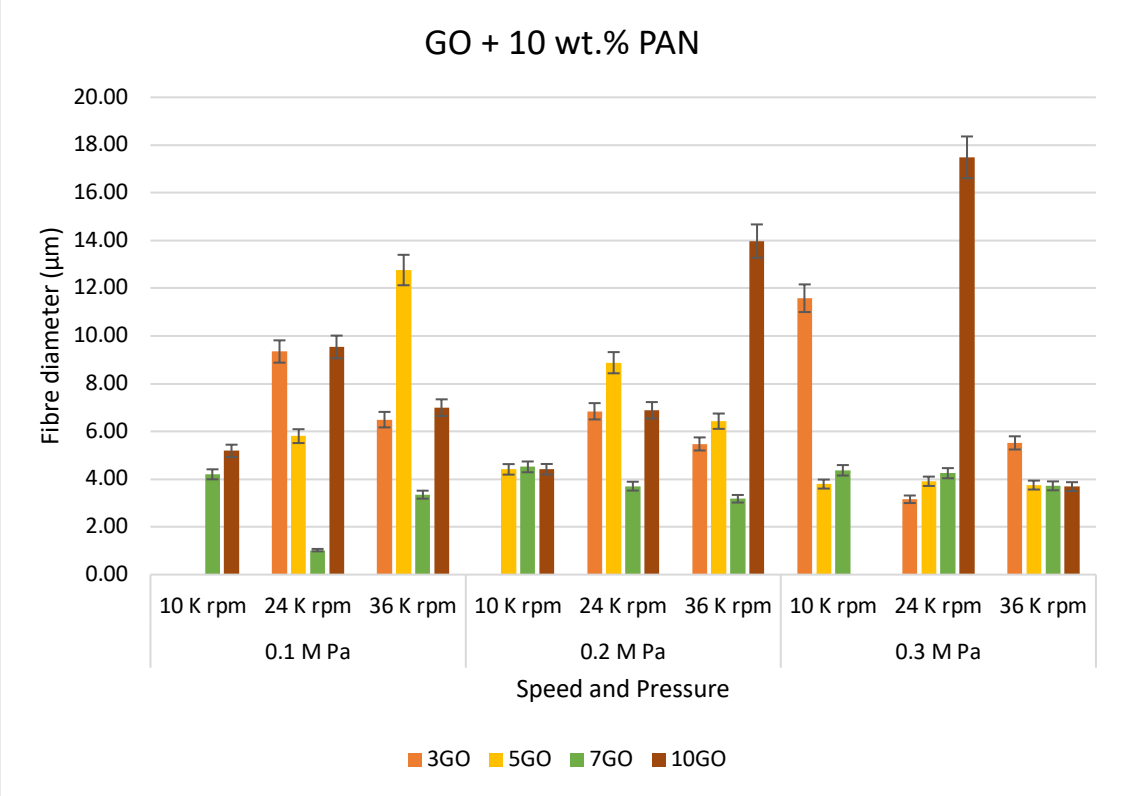

Figure 6.5 Fibre diameter as spun fibre of 10 wt% PAN at different speed and pressure

The trend is quite similar to 10 wt% PAN in Table 6.3 where all the fibres formed when the speed is 24k rpm and 36k rpm at all concentration and pressure.

Composition of 10 wt% GO shows the highest fibre diameter of all parameters, due to more GO particles inside the fibres.

For the 10 wt% PAN-GO fibres, at the lowest rotational speed of 10k rpm and at 0.1 MPa pressure, none of the compositions formed fibres, except 7GO and 10GO. Increasing the speed to 24k rpm, all of the solutions formed fibre composites. However, increasing the speed to 36k rpm, all compositions formed fibres and they are thicker than the fibres formed at 24k rpm rotating speed. At pressure of 0.2 MPa with rotational speeds of 10k rpm 3 wt%, GO didn't yield any fibres but all other compositions did. Increasing the rotating speeds to 24 k and 36 k rpm, fibres were formed. From the observation in Figure 6.5, fibre diameter is large for 24k rpm compared to 36k rpm. At pressures of 0.3 MPa with the 10k rpm rotating speed all the compositions produced fibres except 10GO. By increasing the rotating speeds to 24k and 36k rpm fibres were formed. In general, fibre diameter didn't shown any variation for 24k rpm and 36k rpm for all compositions except 10GO. It is well known that centrifugal force applied on the polymer solution is the driving force for jet formation and mostly affected by the rotating speed. It further influences the exit velocity of the jet, the jet's path to the collector and thus fibre diameter and the fibre morphology. The increase of rotational speed accelerates the polymer chain elongation, thus improves jet attenuation and the fibre diameter decreases. However, the solution mass throughput from the nozzle not only depends on the rotating speed, but is also governed by pressure difference at the orifice. On the other hand, rotating speed influences the air flow that acts outside of the spinneret and helps the

evaporation of the solvent. Higher airflow accelerates solvent evaporation, which suppresses the elongation of the polymer jet resulting in thicker fibres. This may be the reason for the variation in the fibre diameters with various pressures in the process.

A strand fibre of 10 GO 10PAN 36k rpm 0.1 MPa in Figure 6.6 was chosen to observe the particle distributions in the fibre. It has been shown that the graphene oxide particle is located along the fibre.

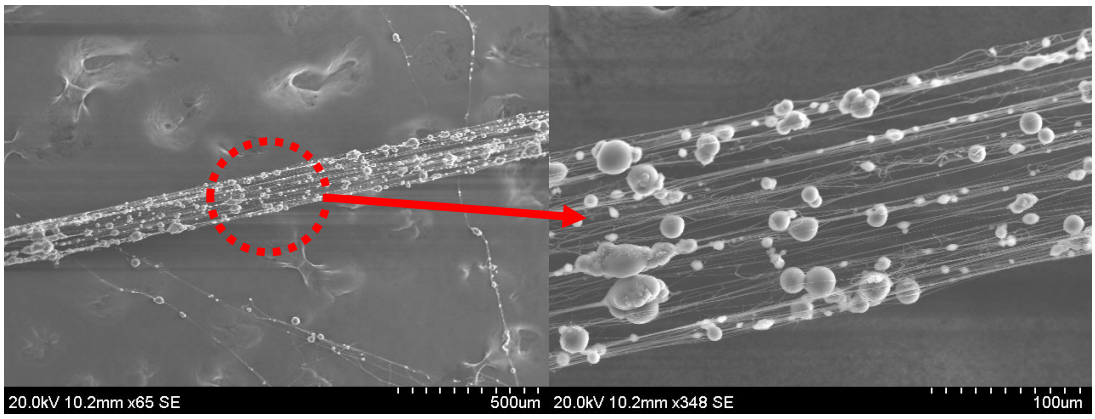

Figure 6.6 The fibre of 10 GO 10PAN 36k rpm 0.1 MPa fibre, showing the particle distribution of the GO in fibre

Figure 6.7 to Figure 6.10 shows the scanning electron microscopy images and size distributions of spun fibres using 3, 5, 7 and 10 wt% solutions subjected to 10k - 36k rpm and 0.1 – 0.3 MPa. The mean fibre size ranged from 20 - 170 nm for the 3 - 10 wt% solutions. The average fibre diameters are listed in Table 6.2 and Table 6.3. At fixed (0.1 MPa) pressure and 36k rpm rotational speed a trend of increasing average fibre size is shown, when the percentage of GO is increased. This is attributed to the volume and mass of polymer solution that is being transferred across the orifice. Thicker polymer jets were formed at a higher

polymer and GO concentration which, on the other hand, hinders the evaporation of solution, causing a more significant transfer rate of solution across the vessel orifices.

Fibre formation just started at lower concentration of 3GO 10PAN 10k rpm at pressure of 0.3 MPa, showed in Figure 6.7 that the fibre started to form. However, the speed was not enough to jet out the fibre and polymer and particle agglomerate in a lump state. However, high pressure force to form fibre, but it's not enough for the fibre formation.

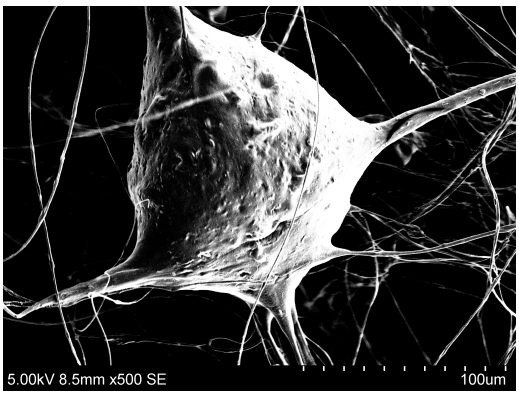

Figure 6.7 3GO 10PAN 10k rpm 0.3 MPa as spun fibre

Figure 6.8 showed that by increasing pressure, the PAN-GO solution is thin, the disjoining pressure affects the capillary interactions between particles attached to the fibre surfaces. It appears between particles protruding from a solution and it a physical origin is the capillary rise of the liquid along the surface of each particle (Kralchevskyt & Nagayama', 1994).

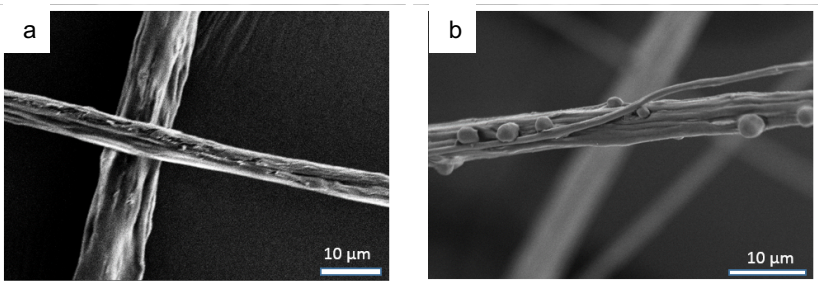

Figure 6.8 a) 3GO 10PAN 24k rpm 0.1 MPa b) 3GO 10PAN 24k rpm 0.2 MPa where at higher pressure, some of the particle force to protruded on the surface

Figure 6.9(b) showed that at a speed of 36k rpm and pressure of 0.3 MPa, composition 3GO 10PAN showed that the fibres formed a graphene composite fibre knot showed it can be stretched under tensile stress, leading to the high fracture elongation for the graphene fibre.

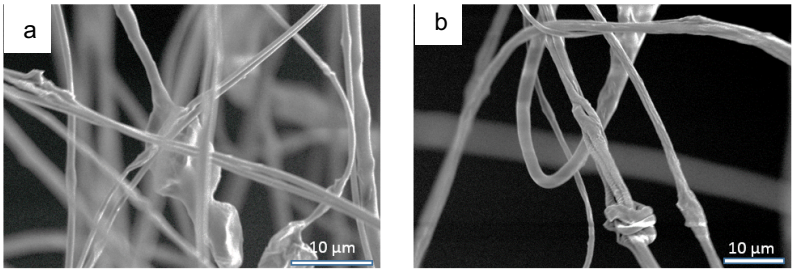

Figure 6.9 a) 3GO 10PAN 36k rpm 0.2 MPa b) 3GO 10PAN 36k rpm 0.3 MPa

The influence of pressure applied during gyration in generating different fibre morphologies was studied by fixing the rotational speed at 36k rpm and conducting experiments at 0.1 - 0.3 MPa for 3 -10 wt% solutions (Table 6.2). It is evident that, in general, a narrow distribution of fibre diameter is achieved at higher working pressures.

At any fixed polymer concentration, by increasing the pressure, a trend of reduction in the fibre diameter was observed. This is due to the introduced gas stream which enhances the combined shearing force (consisting of centrifugal force and blowing) against the surface tension force in the elongational flow of polymer jets (Mahalingam & Edirisinghe, 2013).

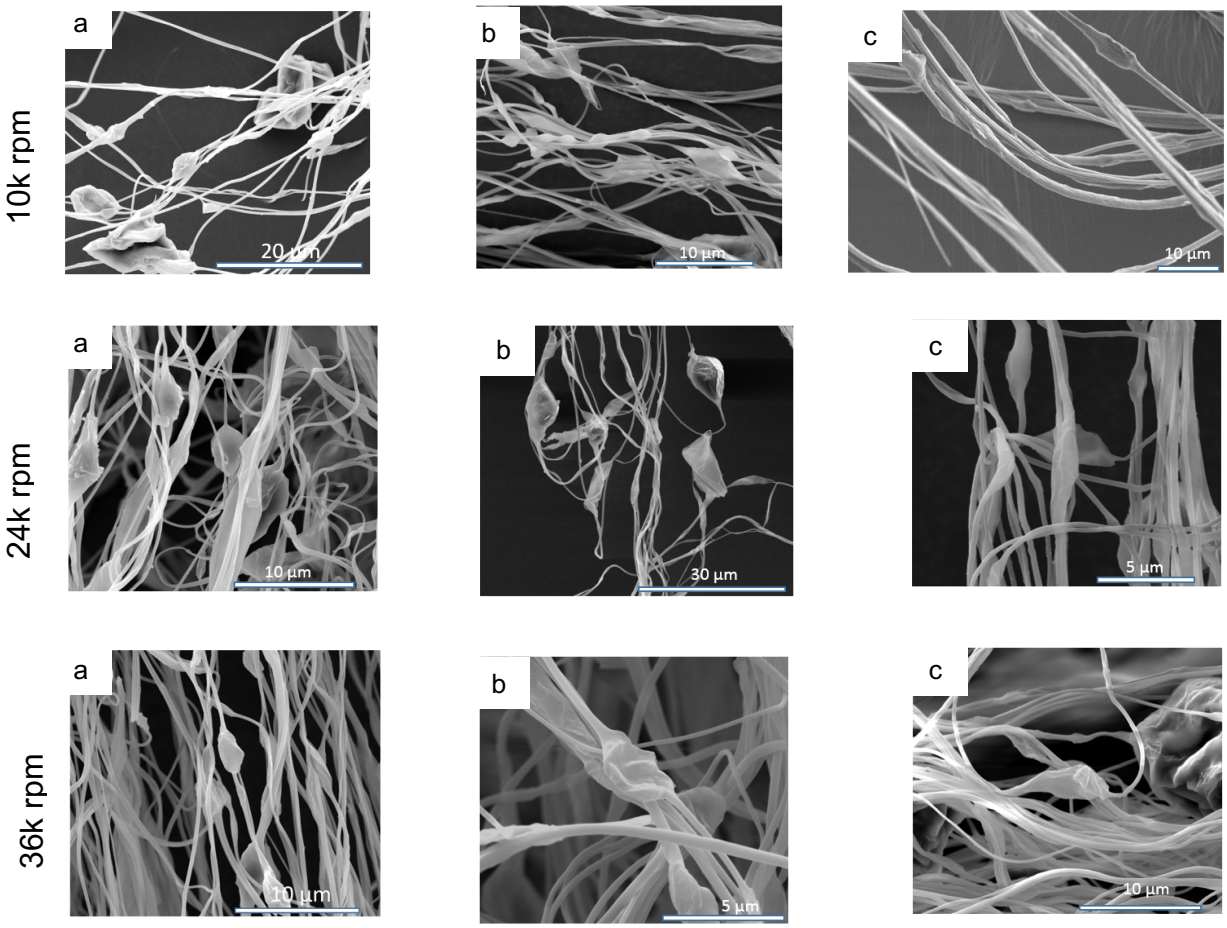

Figure 6.10 7GO 10PAN fibres before pyrolysis of different pressures and speed

Therefore the diameters of the ejected polymer jets at the orifices of the vessel were reduced, which helps to promote thinner fibre formation. Solvent evaporation can be enhanced by blowing a hot air gun which affects the relative

speed of air flow on the liquid-air interface in the polymer at the fibre surface, thus contributing to fibre formation.

The results also indicate that the polymer concentration has a significant influence on the as-spun fibre morphology, that is, the increased polymer viscosity plays a role of stabilising polymer jets against the action of centrifugal force and dynamic solution blowing, hence promoting larger fibre diameter. When the polymer concentration is continuously increased, solvent evaporation is hindered. Hence it leads to the relatively long relaxation time/evaporation time during stretching.

A minimum rotation speed that could result in enough viscous solution response enables the generation of nanofibres at lower polymer concentrations. On the whole, increasing rotational speed accelerates stretching of polymer jets, this decreases the diameters of the polymer jets at the orifices of the vessel, and thinner fibres are obtained. It is seen that, overall, a narrower size distribution is obtained at a higher rotational speed. It is noteworthy that, at 10k rpm not all of the solution is spinnable using a typical pressurised gyration method at a pressure of 0.1 MPa using 8 wt% PAN. However, this new process enables gyratory spinning.

However, it is a great challenge to directly assemble 2D GO sheets into 1D fibres without any polymer or surfactant, due to the lack of scalable assembly methods (Park & Ruoff, 2009) the size and irregular shape of chemically derived graphenes, and the movable layer-by-layer stacking of graphenes (Dong et al.,

2012). Therefore, for integration of the remarkable properties of individual graphene sheet or its derivatives into advanced, macroscopic, and functional structures for practical applications, an effective assembly strategy in a well-controlled way has to be developed (Tian et al., 2013).

6.2.3 Fourier-transform infrared spectroscopy (FTIR)

Polymer compatibility is a crucial factor in determining the stability of nanofibres. If the GO is not compatible with PAN polymer, then a solid phase separation will be observed. Secondary interactions such as hydrogen bonding, hydrophobic reactions, and electrostatic forces can increase the compatibility in the fibres (Chen et al., 2008).

The FTIR spectrum of GO in Figure 6.11 shows, characteristic bands at 3500 cm^{-1} (C-H stress) and 1500 cm^{-1} (C=O stress), while the spectrum of GO-PAN contains peak at 2448 cm^{-1} (N-H stretching), (aromatic and aliphatic C-H stretching). The frequency of the physical mixture is a composite of the pure polymer, containing all the characteristic bands of GO-PAN. This indicates that the interactions between GO and the polymer are weak when they are mixed physically.

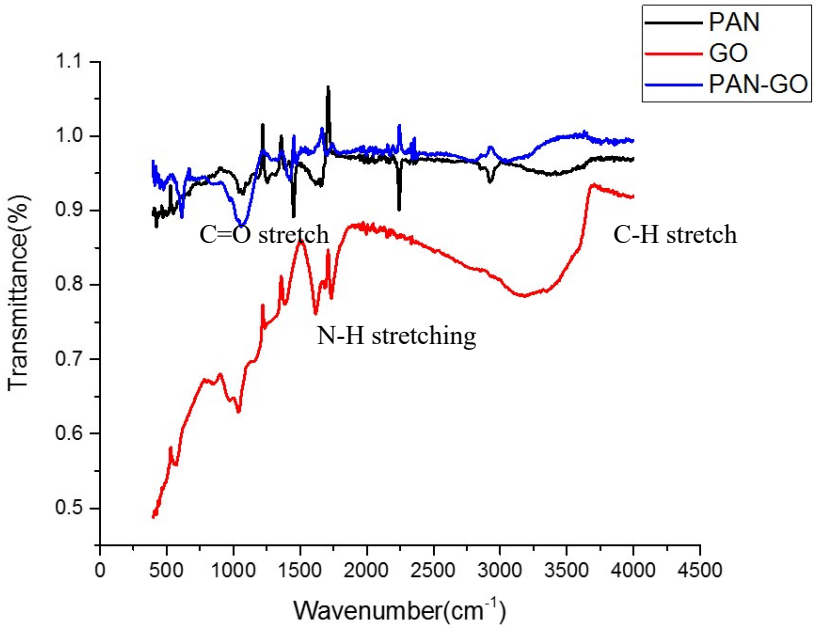

Figure 6.11 FTIR spectrum of GO PAN stretching vibrations

The FTIR spectrum of PAN displays characteristic bands of methyl and methylene C-H stretching vibrations at 3000 cm^{-1} and 1560 cm^{-1}, as well as a strong band due to carbonyl groups at 1500 cm^{-1} (C=O stretch) and two bands due to ester linkages (C-O-C stretches). Therefore it suggests there is good compatibility between GO and PAN.

Regarding the FT-IR spectra (Figure 6.27), the broad signal between 3200 cm^{-1} and 3700 cm^{-1} is generated from O–H stretching vibration and adsorbed water molecules. Two peaks at 2925 cm^{-1} and 2855 cm^{-1} are assigned to asymmetric and symmetric vibrations of CH_2 groups, respectively. The strong signal at 1738 cm^{-1} in the GO's spectrum refers to the C=O stretching vibration which was significantly weakened after reduction. The peak at 1622 cm^{-1} is attributed to the C = C stretching vibration. There are carbonyl stretching regions (1681 – 1764

cm^{-1}), CH_2 deformations (1380 – 1500 cm^{-1}), and aromatic stretches from the hard segment (1617 cm^{-1}), and amide II mixed band (1540 cm^{-1}).

6.2.4 Raman analysis of spun fibres

Raman spectroscopy is widely used to characterise crystal structure, disorder and defects in graphene-based materials. Structural changes during the oxidation and reduction processes was monitored. Raman spectra are characterised by the changes in the relative intensity of two main peaks: D and G. Raman spectroscopy are employed to evaluate the hybridisation of state in carbon, and the two reflections peak change from pristine graphite to its derivatives. As shown in Figure 6.12, a strong band at 1600 cm^{-1} (G band) and a relatively weak band at 1352 cm^{-1} (D band) appear in the Raman spectra of pristine graphite, which stem from the vibration of the sp^2-hybridised graphitic domain, and sp^3-hybridized carbon or structural defects, respectively. The low I_D/I_G value (0.20) indicating the graphitic domains is primarily intact for pristine graphite. It was mainly induced by the n-type effect on the GO which forms the sp^2 carbon modification to sp^3 which is why the intensity ratio of D band and G band decreased.

Comparing the Raman spectra before and after pyrolysis, it has been revealed that there has been a clear change of crystal structure from pristine GO to GO-composite, indicating the reduction of GO into graphene (reduced graphene). The reduction of functional groups onto the surface of GO were also verified by the decrease in intensity of GO after pyrolysis (Figure 6.13).

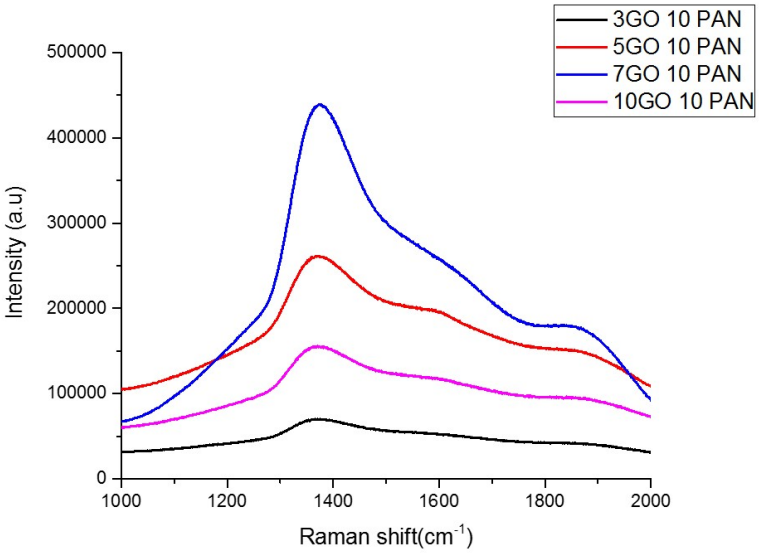

Figure 6.12 Raman spectroscopy of as spun GO PAN solutions

6.2.5 Raman spectroscopy for the analysis of composites after pyrolysis

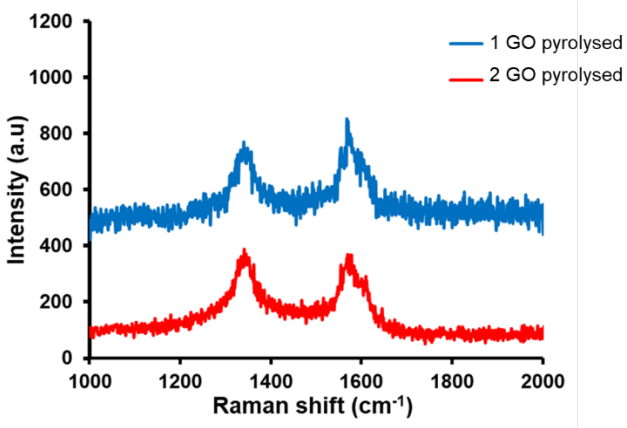

Figure 6.13 Raman spectroscopy of pyrolysed 10 GO 1 and 2 wt% PAN

It was observed in Figure 6.29 that there is a broad Raman peak centred at 1552 cm^{-1}. The broadness of the Raman band suggests that PAN fibres represent disordered arrangements of PAN molecules. The sharpness of this peak was

observed with increasing concentration of GO in the composite revealing the ordered arrangement of GO within composites. Two characteristic peaks at 1340 and 1552 cm^{-1} were observed in composites. These peaks correspond to the D and G bands from defect structure of sp^3-carbon and the plane vibration of the sp^2-carbon atoms in two-dimensional lattice of the GO-PAN composite (Hassan et al., 2015; Tabish et al., 2019). Raman spectral signatures confirm that the cyclization of PAN is associated with graphitization. This feature was observed in all the composites after pressurised gyration in Figure 6.28.

6.2.6 SEM and FIB of GO-PAN fibres and PAN fibres (control) after pyrolysis

To achieve optimal graphene fibre properties, the heating rate of 1 °C/min and a treating time of 30 min was used. After carbonization to 900 °C, graphene fibres were obtained. A PAN-based precursor containing carboxylic acid groups and acrylamide units were used for increasing the stabilization rate and sulphate/sulfonic groups for controlling the denseness of the precursor fibres (Park & Heo, 2015). Residues from the spinning solution can also behave as an initiator for nucleophilic cyclization reactions to reduce stabilization time (Huang, 2009).

The fibre diameter is reduced with the removal of the non-carbon elements. At the early stages of carbonization, crosslinking reactions take place in the oxidized PAN. The cyclized structure starts to link up in the lateral direction by dehydration and denitrogenation. A planar structure can be formed with the basal planes oriented along the fibre axis.

These fibres are generally called “high strength” fibres (X. Huang, 2009). The strength of a carbon fibre is observed to increase with the carbonization temperature and the maximum strength is observed at around 1,500 °C. Too fast a carbonization rate introduces defects in carbon fibres, while low carbonization rate causes the loss of too much nitrogen at the early stages of carbonization (Huang, 2009).

Increasing GO in the fibres showed that less polymeric carbon precursor of PAN fibre as shown in Figure 6.14. It also can be found that voids reduced further with the increase of GO.

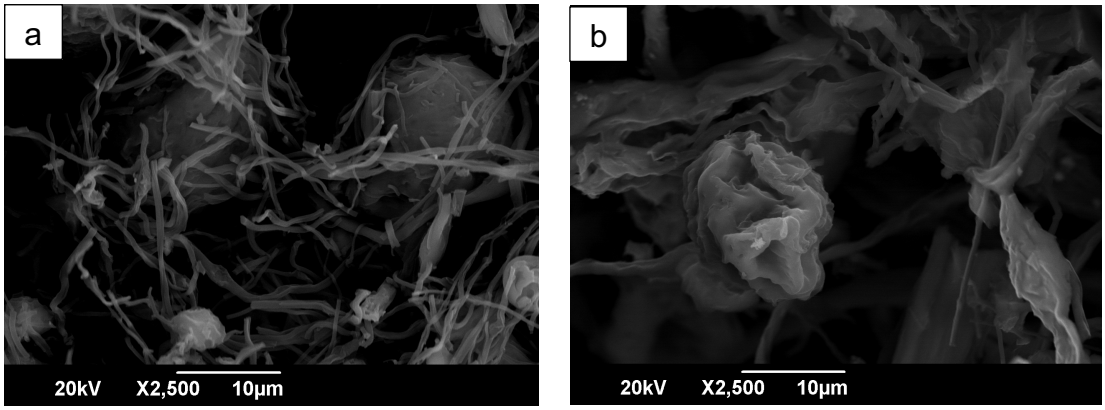

Figure 6.14 (a) Pyrolyzed 7GO 8PAN (b)Pyrolyzed 10GO 8PAN

To verify the graphene in the pyrolyzed fibres, the FIB-SEM in Figure 6.31 of 3wt% GO with 10wt% PAN fibres pyrolysed and used as received. For the control sample, 10% PAN fibres were pyrolysed without GO and used as received.

Increasing the GO, the surface of the fibres became rougher and up to 3 wt% GO (Figure 6.15d), the fibres started to break. This support the findings in Section 6.2.7 where only up to 2 wt% GO that conducts electric. This might be

due to the graphene fibres became brittle due to high percentage of carbon structure including the PAN as carbon precursor which form carbon structure during thermal pyrolysis.

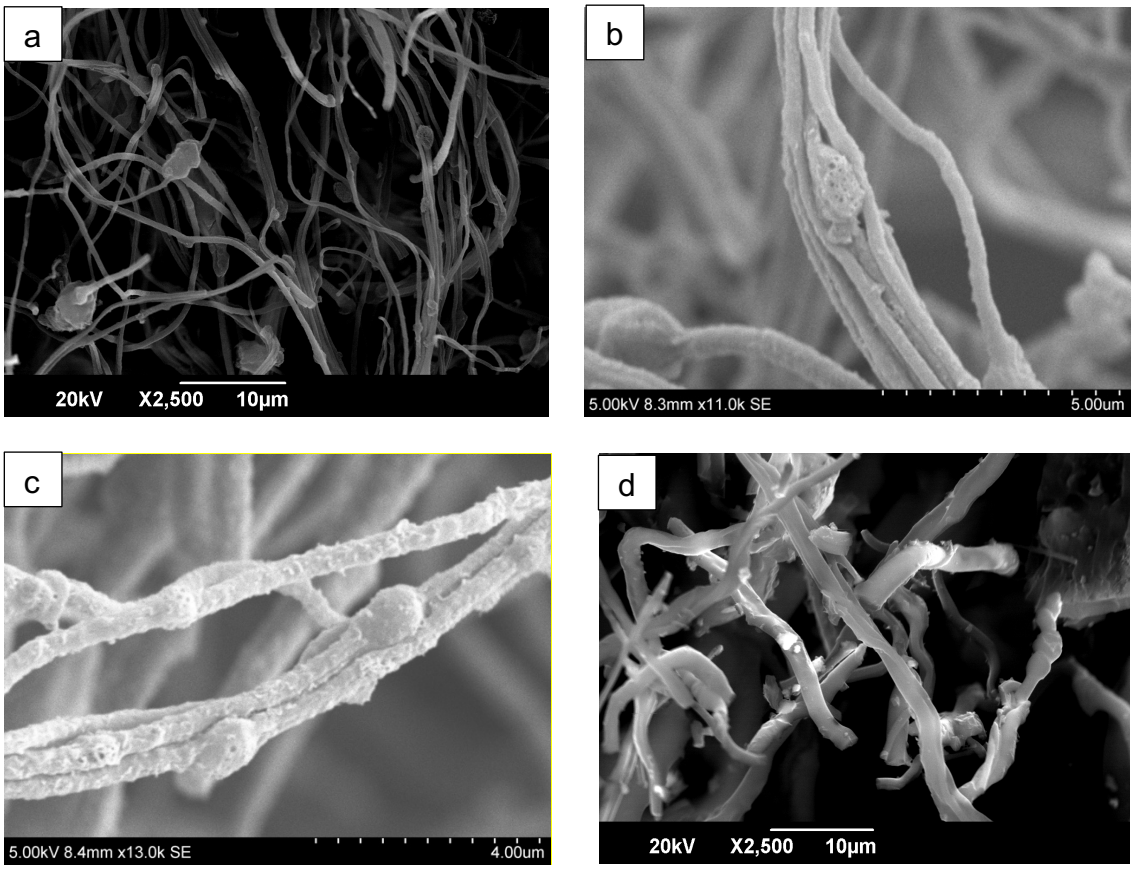

Figure 6.15 SEM of pyrolyzed 10 GO 1-3 wt% PAN (a) Pyrolyzed 10PAN – controlled (b) Pyrolyzed 1GO 10PAN (c) Pyrolyzed 2GO 10PAN (d) Pyrolyzed 3GO 10PAN

Before SEM and FIB, a 15 nm coating of platinum at 45 s of spattering was prepared. Pyrolysed 3wt% GO with 10wt% PAN fibres show distinct granular, grainy internal morphology, whereas the control, (pyrolysed 10wt% PAN fibres) show a smooth, porous internal structure.

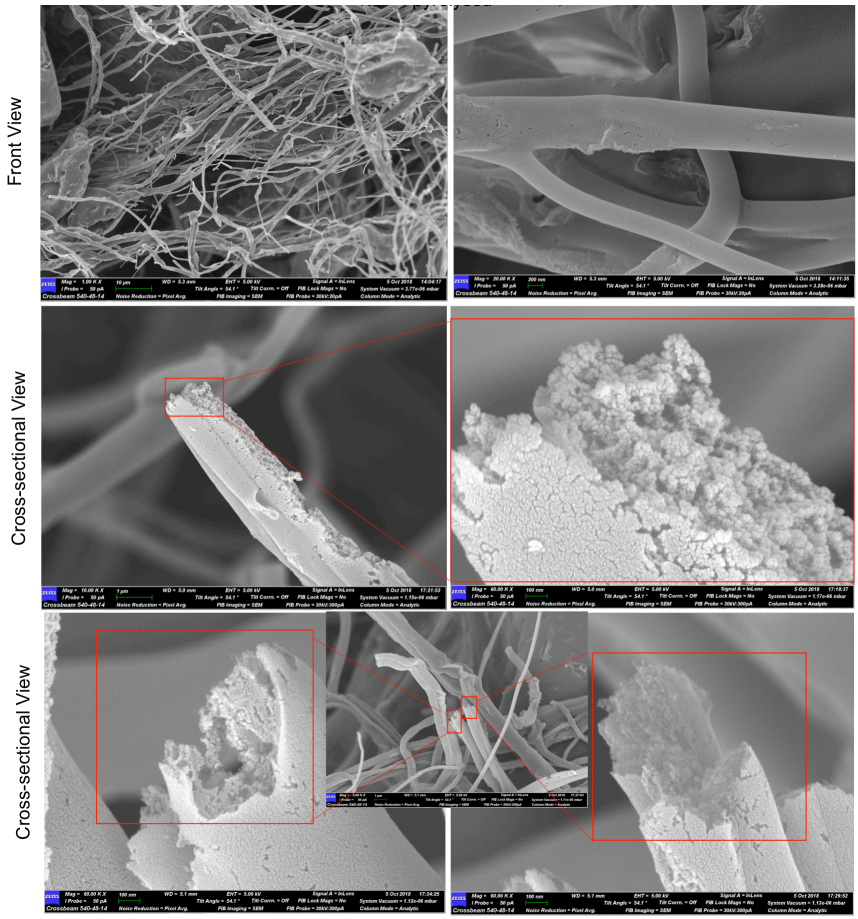

Figure 6.16 FIB-SEM 3 wt% GO in 10 wt% PAN

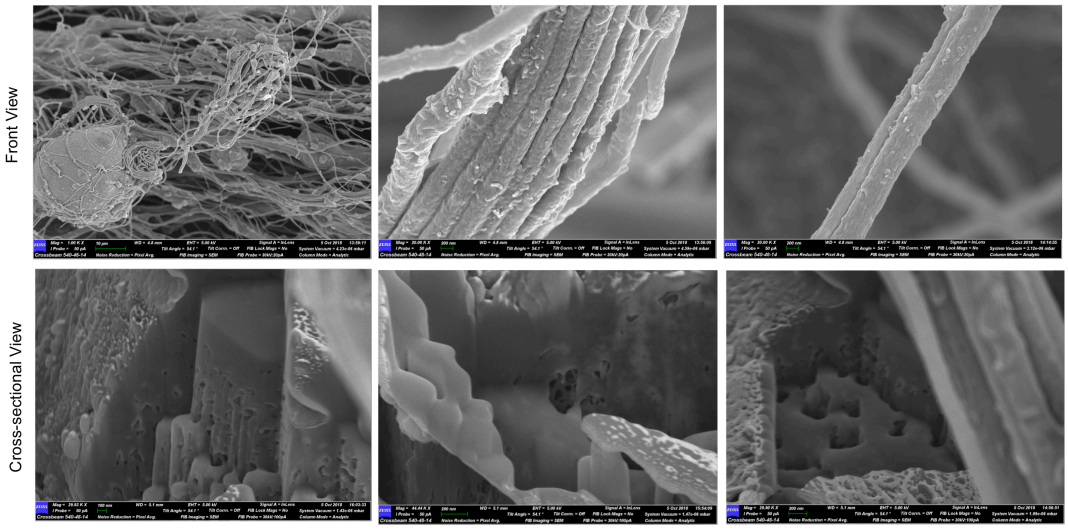

Figure 6.17 FIB-SEM of 10 wt% PAN

6.2.7 Conductivity test

Electrical conductivity tests showed that after pyrolysis only 1 wt% GO 10 wt% PAN and 2 wt% GO 10 wt% PAN with value of 973 Ω and 459 Ω respectively. There was no electrical conductivity for as spun fibres as GO reacts as an insulator before pyrolysis. At high percentages of GO, there is no conductivity because it tends to stack and form as graphite rather than graphene. As discussed in section 2.3, graphene in 2D has electrical conductivity. Compared to the raman spectra in Section 6.2.5, it showed that the G band stronger at 1 wt% GO than 2 wt% GO.

6.3 Conclusions

The processability of GO-PAN was shown at 10 wt% PAN compared to lower concentrations of 8 wt%. At lower concentrations of GO (1 - 2 wt%), there is conductivity at 10 wt% PAN. FIB of pyrolyzed fibres showed granular morphology while the controlled sample without GO had a smooth surface. However, it is a great challenge to directly assemble 2D GO sheets into 1D fibres without any polymer or surfactant, due to the lack of scalable assembly methods (Park & Ruoff, 2009) the size and irregular shape of chemically derived graphenes, and the movable layer-by-layer stacking of graphenes (Dong et al., 2012)Therefore, for integration of the remarkable properties of individual graphene sheet or its derivatives into advanced, macroscopic, and functional structures for practical applications, an effective assembly strategy in a well-controlled way has to be developed (Tian et al., 2013).

Chapter 7 **Conclusions and for future works**

7.1 Conclusions

Graphene fibres have promising applications in several fields. Due to limitations and challenges of processability, the most practical route of processing the fibres has been simplified. Graphene fibre composite using pressurised gyration technique were developed. Fibres were fabricated using various speed as well as pressure. Various polymers were used to develop the fibre composites. Therefore, new formulations and parameters would be a significant contribution towards the discovering of graphene fibres potential applications. The following conclusions are drawn from this study.

7.1.1 Thermoplastic polyurethane (TPU) and Phenolic resins (PR) loaded graphene nanoparticles (GNP)

Graphene loaded TPU fibres were successfully formed using a pressurised gyration process. The process makes use of simultaneous centrifugal force and dynamic fluid flow to jet the fibres before evaporation of the solvents to form the composite fibres. The fibre diameter generated was in the range of 800–6000 nm. The forming process conditions such as vessel rotating speed, working pressure and the polymer concentration used, had a significant effect on fibre diameter. The fibre diameter increased with increasing weight percentage of phenolic resin and TPU polymer. The use of higher working pressures resulted in reduced fibre diameters. However, for the highest rotational speed there is no fibre produced. FTIR and Raman spectroscopy analysis confirmed the various bonding characteristics of the hybrid composite fibre structures. Focussed ion

beam milling and etching verified the effective incorporation of graphene nanoparticles into the fibre composites.

7.1.2 Polyvinylpyrrolidone (PVP) loaded graphene nanoparticles (GNP)

Graphene loaded PVP fibres were successfully formed using a pressurised gyration process. The process makes use of simultaneous centrifugal force and dynamic fluid flow to jet the fibres before evaporation of the solvents to form the composite fibre. All curves showed non-Newtonian behaviour and the viscosity increased with increasing polymer concentration. Raman spectroscopy analysis confirmed the various bonding characteristics of the hybrid composite fibre structures.

7.1.3 Generating polyacrylonitrile-loaded graphene nanoparticle

Carbon nanofibres were obtained by utilising pressurised gyration and high temperature processing. The fibre diameter and distribution is controlled by the key forming parameters of rotating speed, working pressure and the loading concentration of the graphene nanoplatelets. The pyrolysis and the spark plasma temperature influenced the microstructures of the carbon nanofibres. A heat treatment temperature of 2400 °C in SPS produced nanofibres with a high degree of graphitization with properties superior to those of commercial carbon fibres. These nanofibres are useful in advanced engineering applications.

7.1.4 Generating polyacrylonitrile-loaded graphene oxide

The processability of GO-PAN was shown at 10 wt% PAN compared to the lower concentration of 8 wt%. At lower concentrations of GO (1 - 2 wt%), there is conductivity at 10 wt% PAN. FIB of pyrolyzed fibres showed granular morphology while the control sample without GO had a smooth surface.

7.2 Future work

The findings from this project are subjected to certain limitations. For instance, the TPU loaded GNP was limited by vortex mixing which took a very long time to fully dissolve. Hence, it would be of particular interest to continue the present study by further investigating on graphene precursor systems. The potential of using graphene oxide as a precursor as the chemical structure of sp^3 carbon clusters enables better performance and combination to achieve a stable phase. The graphene precursor such as graphite sulphate, PAN and graphene oxide have opened up the possibility of studying graphene fibres using similar approaches. However, it should be noted that future work should not only include an improved graphene fibre, but also needs to demonstrate how to improve its capacitance and antimicrobial activity.

7.2.1 Graphene Oxide and conductive polymers (PAN/polypyrrole)

Graphene oxide (GO), a two-dimensional nanosheet of covalently bonded carbon atoms bearing various oxygen functional groups (e.g. hydroxyl, epoxide and carbonyl groups) on their basal planes and edges, is a rapidly growing

research interest. The graphene–polyaniline (G–PAN) composite material has recently been used for energy applications. A supercapacitor was fabricated using G–PAN in N-Methyl-2-pyrrolidone (NMP) to optimize their components and packaging towards a qualification for portable systems applications (Gómez et al., 2011). In GO-PAN composite, it is observed that the sensing property is better and more reproducible than pure PAN (Konwer, Guha, & Dolui, 2013). Highly conductive lightweight graphene fibres are good candidates for wires and cables to carry heavy current (Xu & Gao, 2011). Therefore GO-PAN and GO-PAN-NMP fibres will be suitable candidates for this project.

7.2.2 Graphene Oxide and natural cellulose (chitosan) for antimicrobial applications

The excellent water solubility of graphene oxide (GO) imparts its feasibility as a new filler for reinforcing hydrophilic biopolymers such as PVP, PVA, PEG, PEO, PMMA and more. Graphene oxide (GO), which is one of the graphene derivatives, has gained considerable attention as a significant adsorbent. There are plenty of oxygen atoms on the graphitic backbone of GO in the forms of epoxy, hydroxyl, and carboxyl groups, which protrude from its layers. These groups can bind to metal ions well. In addition, the huge surface area of GO gives it a large adsorption capacity which is similar to carbon nanotube adsorption (Tzeng et al., 2011). Since chitosan is a polysaccharide, like cellulose, the possibility of producing carbon fibres from chitosan seemed quite high. Chitosan may have some advantages over cellulose in the production of carbon fibres, such as higher yield and better mechanical properties, due to its structural differences from cellulose (Bengisu & Yilmaz, 2002). Chitosan and graphene

oxide could mix with each other homogeneously and the mechanical properties of the as-prepared films were improved significantly over that of the pure chitosan film, especially in wet state (Han et al., 2011). The presence of GO in PAN/GO composite increases the sensitivity towards methanol as compared with the pure PAN (Konwer et al., 2013; Mohamadzadeh et al., 2014). Nanocomposites showed semiconducting nature as PAN did, with improved properties for EMI shielding. The EMI shielding effectiveness (SE) of nanocomposites was found to be increased with increasing GN content and it was found to be absorption dominated, indicating PAN/Graphene nanocomposites can be used as lightweight EMI shielding materials to protect electronic devices and components from electromagnetic radiation (Modak, Kondawar, & Nandanwar, 2015).

7.2.3 Graphene Oxide and Ag nanoparticles – antimicrobial applications

Most carbon-based nano-materials are cytotoxic to bacteria. Fabricated graphene oxide (GO) nanosheets impregnated with silver nanoparticles (Ag-NPs) exhibit stronger antibacterial activity against Escherichia coli and Staphylococcus aureus (Bao, Zhang, & Qi, 2011). The low cost of GO, the relative simplicity of its manufacturing procedure, and its effective antibacterial properties, makes it reasonable to anticipate the great applications of this composite in water treatment, purification processes and the production of antimicrobial nanocomposites. AgNPs are widely known because of their outstanding antimicrobial toxicity (Shao et al., 2015). The incorporation of Ag NPs into GO does not influence external features such as color, but inhibits the

agglomeration of both GO nanosheets and Ag NPs. Enhanced antibacterial performance was observed for the Ag NP/GO composites (Bao et al., 2011). Methicillin-resistant Staphylococcus aureus (MRSA) has been responsible for serious hospital infections worldwide. GO-Ag nanocomposites interact with MRSA cells, indicating that GO-Ag nanocomposites are promising antibacterial agents. These nanocomposites may possibly be used as a platform for the development of novel materials that are able to mitigate microbial proliferation in biomedical devices and hospital facilities (de Moraes et al., 2015). GO-based silver nanoparticle-containing composite hydrogel matrix acts as a potential catalyst for removing organic dye pollutants for organic dye removal and wastewater treatment from an aqueous environment (Jiao et al., 2015).

7.2.4 Charged solutions poly(3,4-ethylenedioxythiophene) polystyrene sulfonate (PEDOT:PSS) with graphene to align the orientation

PEDOT:PSS exhibits low cost and low thermal conductivity as well as high electrical conductivity. It's composite thin films were developed by Soltani et.al. (Soltani-Kordshuli, Zabihi, & Eslamian, 2016) using substrate vibration-assisted ultrasonic spray coating (SVASC) solution containing graphene. Graphene sheets were broken by sonication and were uniformly dispersed and stabilized in PEDOT:PSS aqueous solution. While Kim (Kim et al., 2018) developed PEDOT:PSS (PP)/GNP (PPG) composite that maintains the catalytic performance of GNPs with enhanced adhesion to the substrate via a conductive PEDOT matrix to replace expensive Platinum (Pt) solar cells. Du et al. (Du et al.,

2018) discovered reasonable enhancement in the thermoelectric performance of PEDOT:PSS by constructing unique composite films with graphene quantum dots.

7.2.5 Carbon filters

Carbon filters can be used to filter the smoke from factories and domestic exhaust. Built with carbon fibres and natural gelatine to trap the carbon oxide and release oxygen, has create green environments and improved sustainability. The carbon can be used again or refined as recycled carbon to be used in further processes.

References

Acik, M., Lee, G., Mattevi, C., Pirkle, A., Wallace, R. M., Chhowalla, M., Chabal, Y. (2011). The Role of Oxygen during Thermal Reduction of Graphene Oxide Studied by Infrared Absorption Spectroscopy. *The Journal of Physical Chemistry C*, *115*(40), 19761–19781. https://doi.org/10.1021/jp2052618

Araby, S., Zaman, I., Meng, Q., Kawashima, N., Michelmore, A., Kuan, H.-C., Zhang, L. (2013). Melt compounding with graphene to develop functional, high-performance elastomers. *Nanotechnology*, *24*(16), 165601. https://doi.org/10.1088/0957-4484/24/16/165601

Badamshina, E., Estrin, Y., & Gafurova, M. (2013). Nanocomposites based on polyurethanes and carbon nanoparticles: preparation, properties and application. *Journal of Materials Chemistry A*, *1*(22), 6509. https://doi.org/10.1039/c3ta10204a

Badrossamay, M. R., McIlwee, H. A., Goss, J. A., & Parker, K. K. (2010). Nanofiber assembly by rotary jet-spinning. *Nano Letters*, *10*(6), 2257–2261. https://doi.org/10.1021/nl101355x

Bai, H., Walsh, F., Gludovatz, B., Delattre, B., Huang, C., Chen, Y., Ritchie, R. O. (2016). Bioinspired Hydroxyapatite/Poly(methyl methacrylate) Composite with a Nacre-Mimetic Architecture by a Bidirectional Freezing Method. *Advanced Materials*, *28*(1), 50–56. https://doi.org/10.1002/adma.201504313

Bai, Y., Huang, Z.-H., & Kang, F. (2013). Synthesis of reduced graphene oxide/phenolic resin-based carbon composite ultrafine fibers and their adsorption performance for volatile organic compounds and water. *Journal of Materials Chemistry A*, *1*, 9536–9543. https://doi.org/10.1039/C3TA10545H

Banhart, F. (2004). Formation and transformation of carbon nanoparticles under electron irradiation. *Phil. Trans. R. Soc. Lond. A* 362, 2205–2222 https://doi.org/10.1098/rsta.2004.1436

Bao, Q., Zhang, D., & Qi, P. (2011). Synthesis and characterization of silver nanoparticle and graphene oxide nanosheet composites as a bactericidal agent for water disinfection. *Journal of Colloid and Interface Science*, *360*(2), 463–470. https://doi.org/10.1016/j.jcis.2011.05.009

Barick, A. K., & Tripathy, D. K. (2010). Effect of nanofiber on material properties of vapor-grown carbon nanofiber reinforced thermoplastic polyurethane (TPU/CNF) nanocomposites prepared by melt compounding. *Composites Part A: Applied Science and Manufacturing*, *41*(10), 1471–1482. https://doi.org/10.1016/j.compositesa.2010.06.009

Bello, A., Barzegar, F., Momodu, D., Dangbegnon, J., Taghizadeh, F., & Manyala, N. (2015). Symmetric supercapacitors based on porous 3D interconnected carbon framework. *Electrochimica Acta*, *151*, 386–392. https://doi.org/10.1016/j.electacta.2014.11.051

Bengisu, M., & Yilmaz, E. (2002). Oxidation and pyrolysis of chitosan as a route for carbon fiber derivation. *Carbohydrate Polymers*, *50*(2), 165–175. https://doi.org/10.1016/S0144-8617(02)00018-8

Betancourt, S., Cruz, L. J., & Toro, A. (2011). Effect of the addition of carbonaceous fibers on the tribological behavior of a phenolic resin sliding against cast iron. *Wear*, *272*(1), 43–49. https://doi.org/10.1016/j.wear.2011.07.014

Bhardwaj, N., & Kundu, S. C. (2010). Electrospinning: a fascinating fiber fabrication technique. *Biotechnology Advances*, *28*(3), 325–347. https://doi.org/10.1016/j.biotechadv.2010.01.004

Bose, S., Kuila, T., Mishra, A. K., Rajasekar, R., Kim, N. H., & Lee, J. H. (2012).

Carbon-based nanostructured materials and their composites as supercapacitor electrodes. *Journal of Materials Chemistry*, *22*(3), 767–784. https://doi.org/10.1039/c1jm14468e

Brint, S. F., Ostrick, D. M., & Bryan, J. E. (1991). Keratometric cylinder and visual performance following phacoemulsification and implantation with silicone small-incision or poly(methyl methacrylate) intraocular lenses. *Journal of Cataract & Refractive Surgery*, *17*(1), 32–36. https://doi.org/10.1016/S0886-3350(13)80981-9

Butt, H.-J., Graf, K. (Karlheinz), Kappl, M., & John Wiley & Sons. (2003). *Physics and chemistry of interfaces*. Retrieved from https://www.wiley.com/en-gb/Physics+and+Chemistry+of+Interfaces-p-9783527606405

Cai, X., Tong, H., Shen, X., Chen, W., Yan, J., & Hu, J. (2009). Preparation and characterization of homogeneous chitosan–polylactic acid/hydroxyapatite nanocomposite for bone tissue engineering and evaluation of its mechanical properties. *Acta Biomaterialia*, *5*(7), 2693–2703. https://doi.org/10.1016/j.actbio.2009.03.005

Canché-Escamilla, G., Duarte-Aranda, S., & Toledano, M. (2014). Synthesis and characterization of hybrid silica/PMMA nanoparticles and their use as filler in dental composites. *Materials Science & Engineering. C, Materials for Biological Applications*, *42*, 161–167. https://doi.org/10.1016/j.msec.2014.05.016

Caro-Osorio, E., De la Garza-Ramos, R., Martínez-Sánchez, S., & Olazarán-Salinas, F. (2013). Cranioplasty with polymethylmethacrylate prostheses fabricated by hand using original bone flaps: Technical note and surgical outcomes. *Surgical Neurology International*, *4*(1), 136. https://doi.org/10.4103/2152-7806.119535

Cato, A. D., & Edie, D. D. (2003). Flow behavior of mesophase pitch. *Carbon*, *41*(7), 1411–1417. https://doi.org/10.1016/S0008-6223(03)00050-2

Chandra, V., & Kim, K. S. (2011). Highly selective adsorption of Hg^{2+} by a polypyrrole-reduced graphene oxide composite. *Chemical Communications (Cambridge, England)*, *47*(13), 3942–3944. https://doi.org/10.1039/c1cc00005e

Chen, D., Feng, H., & Li, J. (2012). Graphene Oxide: Preparation, Functionalization, and Electrochemical Applications. *Chemical Reviews*, *112*(11), 6027–6053. https://doi.org/10.1021/cr300115g

Chen, G.-H., Wu, D.-J., Weng, W.-G., & Yan, W.-L. (2001). Dispersion of graphite nanosheets in a polymer matrix and the conducting property of the nanocomposites. *Polymer Engineering & Science*, *41*(12), 2148–2154. https://doi.org/10.1002/pen.10909

Chen, G., Chen, X., Wang, H., & Wu, D. (2007). Dispersion of graphite nanosheets in polymer resins via masterbatch technique. *Journal of Applied Polymer Science*, *103*(6), 3470–3475. https://doi.org/10.1002/app.24431

Chen, L., He, Y., Chai, S., Qiang, H., Chen, F., & Fu, Q. (2013). Toward high performance graphene fibers. *Nanoscale*, *5*, 5809–5815. https://doi.org/10.1039/c3nr01083j

Chen, Z., Yu, D., Xiong, W., Liu, P., Liu, Y., & Dai, L. (2014). Graphene-based nanowire supercapacitors. *Langmuir : The ACS Journal of Surfaces and Colloids*, *30*(12), 3567–3571. https://doi.org/10.1021/la500299s

Cheng, H., Hu, Y., Zhao, F., Dong, Z., Wang, Y., Chen, N., Qu, L. (2014). Moisture-activated torsional graphene-fiber motor. *Advanced Materials (Deerfield Beach, Fla.)*, *26*(18), 2909–2913. https://doi.org/10.1002/adma.201305708

Cheng, H., Liu, J., Zhao, Y., Hu, C., Zhang, Z., Chen, N., Qu, L. (2013). Graphene Fibers with Predetermined Deformation as Moisture-Triggered Actuators and Robots. *Angewandte Chemie International Edition*, *52*(40), 10482–10486. https://doi.org/10.1002/anie.201304358

Chung, D. D. L. (2001). Electromagnetic interference shielding effectiveness of carbon materials. *Carbon,* 39(2), 279-285. https://doi.org/10.1016/S0008-6223(00)00184-6

Chunhui, S., Mu, P., & Runzhang, Y. (2008). The effect of particle size gradation of conductive fillers on the conductivity and the flexural strength of composite bipolar plate. *International Journal of Hydrogen Energy*, *33*(3), 1035–1039. https://doi.org/10.1016/j.ijhydene.2007.11.013

Comins, D. L., & Joseph, S. P. (2001). *N,N* -Dimethylformamide. In *Encyclopedia of Reagents for Organic Synthesis*. https://doi.org/10.1002/047084289X.rd335

Cooper, C. A., & Young, R. J. (2000). Investigation into the deformation of carbon nanotubes and their composites through the use of Raman spectroscopy. in *SPIE 4098, Optical Devices and Diagnostics in Materials Science* (Vol. 4098, p. 172). https://doi.org/10.1117/12.401626

Dai, H., Wong, E. W., Lu, Y. Z., Fan, S., & Lieber, C. M. (1995). Synthesis and characterization of carbide nanorods. *Nature*, *375*(6534), 769–772. https://doi.org/10.1038/375769a0

de Moraes, A. C. M., Lima, B. A., de Faria, A. F., Brocchi, M., & Alves, O. L. (2015). Graphene oxide-silver nanocomposite as a promising biocidal agent against methicillin-resistant Staphylococcus aureus. *International Journal of Nanomedicine*, *10*, 6847–6861. https://doi.org/10.2147/IJN.S90660

Deng, L., Eichhorn, S. J., Kao, C.-C., & Young, R. J. (2011). The Effective

Young's Modulus of Carbon Nanotubes in Composites. *ACS Applied Materials & Interfaces*, *3*(2), 433–440. https://doi.org/10.1021/am1010145

Deng, L., Lewandowska, A. E., Young, R. J., Zhang, G., Sun, R., & Eichhorn, S. J. (2014). Catalytic graphitization of electrospun cellulose nanofibres using silica nanoparticles. *Reactive and Functional Polymers*, *85*, 235–238. https://doi.org/10.1016/J.REACTFUNCTPOLYM.2014.09.001

Deng, R., Liu, S., Liang, F., Wang, K., Zhu, J., & Yang, Z. (2014). Polymeric Janus Particles with Hierarchical Structures. *Macromolecules*, *47*(11), 3701–3707. https://doi.org/10.1021/ma500331w

Deravi, L. F., Sinatra, N. R., Chantre, C. O., Nesmith, A. P., Yuan, H., Deravi, S. K., Parker, K. K. (2017). Design and Fabrication of Fibrous Nanomaterials Using Pull Spinning. *Macromolecular Materials and Engineering*, *302*(3), 1600404. https://doi.org/10.1002/mame.201600404

Dillon, A. C., Yudasaka, M., & Dresselhaus, M. S. (2004). Employing Raman spectroscopy to qualitatively evaluate the purity of carbon single-wall nanotube materials. *Journal of Nanoscience and Nanotechnology*, *4*(7), 691–703. Retrieved from http://www.ncbi.nlm.nih.gov/pubmed/15570946

Dong, X., Wang, P., Fang, W., Su, C.-Y., Chen, Y.-H., Li, L.-J., Chen, P. (2011). Growth of large-sized graphene thin-films by liquid precursor-based chemical vapor deposition under atmospheric pressure. *Carbon*, *49*(11), 3672–3678. https://doi.org/10.1016/j.carbon.2011.04.069

Dong, Z., Jiang, C., Cheng, H., Zhao, Y., Shi, G., Jiang, L., & Qu, L. (2012). Facile Fabrication of Light, Flexible and Multifunctional Graphene Fibers. *Advanced Materials*, *24*(14), 1856–1861. https://doi.org/10.1002/adma.201200170

Dresselhaus, M. S., Dresselhaus, G., Jorio, A., Souza Filho, A. G., & Saito, R. (2002). Raman spectroscopy on isolated single wall carbon nanotubes.

Carbon, *40*(12), 2043–2061. https://doi.org/10.1016/S0008-6223(02)00066-0

Dreyer, D. R., Park, S., Bielawski, C. W., & Ruoff, R. S. (2009). The chemistry of graphene oxide. *Chemical Society Reviews,* 2010, 39, 228–240 https://doi.org/10.1039/b917103g

Du, F.-P., Cao, N.-N., Zhang, Y.-F., Fu, P., Wu, Y.-G., Lin, Z.-D., Cheng, C. (2018). PEDOT:PSS/graphene quantum dots films with enhanced thermoelectric properties via strong interfacial interaction and phase separation. *Scientific Reports*, *8*(1), 6441. https://doi.org/10.1038/s41598-018-24632-4

Eda, G., Ball, J., Mattevi, C., Acik, M., Artiglia, L., Granozzi, G., Chhowalla, M. (2011). Partially oxidized graphene as a precursor to graphene. *Journal of Materials Chemistry*, *21*(30), 11217. https://doi.org/10.1039/c1jm11266j

Eigler, S. (2015). Graphite sulphate – a precursor to graphene. *Chemical Communications (Cambridge, England)*, *51*(15), 3162–3165. https://doi.org/10.1039/c4cc09381j

Ellison, C. J., Phatak, A., Giles, D. W., Macosko, C. W., & Bates, F. S. (2007). Melt blown nanofibers: Fiber diameter distributions and onset of fiber breakup. *Polymer*, *48*(11), 3306–3316. https://doi.org/10.1016/j.polymer.2007.04.005

Fernandes, S. C. M., Freire, C. S. R., Silvestre, A. J. D., Pascoal Neto, C., Gandini, A., Berglund, L. A., & Salmén, L. (2010). Transparent chitosan films reinforced with a high content of nanofibrillated cellulose. *Carbohydrate Polymers*, *81*(2), 394–401. https://doi.org/10.1016/j.carbpol.2010.02.037

Fong, H., Chun, I., & Reneker, D. (1999). Beaded nanofibers formed during electrospinning. *Polymer*, *40*(16), 4585–4592.

https://doi.org/10.1016/S0032-3861(99)00068-3

Frackowiak, E., Khomenko, V., Jurewicz, K., Lota, K., & Béguin, F. (2006). Supercapacitors based on conducting polymers/nanotubes composites. *Journal of Power Sources*, *153*(2), 413–418. https://doi.org/10.1016/j.jpowsour.2005.05.030

Frank, I. W., Tanenbaum, D. M., van der Zande, A. M., & McEuen, P. L. (2007). Mechanical properties of suspended graphene sheets. *Journal of Vacuum Science & Technology B: Microelectronics and Nanometer Structures*, *25*(6), 2558. https://doi.org/10.1116/1.2789446

Fukutake, N., Miyoshi, N., Takasawa, Y., Urakawa, T., Gowa, T., Okamoto, K., Washio, M. (2010). Micro- and Nano-Scale Fabrication of Fluorinated Polymers by Direct Etching Using Focused Ion Beam. *Japanese Journal of Applied Physics*, *49*(6), 065201. https://doi.org/10.1143/JJAP.49.065201

Gómez, H., Ram, M. K., Alvi, F., Villalba, P., Stefanakos, E. (Lee), & Kumar, A. (2011). Graphene-conducting polymer nanocomposite as novel electrode for supercapacitors. *Journal of Power Sources*, *196*(8), 4102–4108. https://doi.org/10.1016/j.jpowsour.2010.11.002

Gupta, P., Elkins, C., Long, T. E., & Wilkes, G. L. (2005). Electrospinning of linear homopolymers of poly(methyl methacrylate): exploring relationships between fiber formation, viscosity, molecular weight and concentration in a good solvent. *Polymer*, *46*(13), 4799–4810. https://doi.org/10.1016/j.polymer.2005.04.021

Gurunathan, S., Han, J. W., Dayem, A. A., Eppakayala, V., & Kim, J.-H. (2012). Oxidative stress-mediated antibacterial activity of graphene oxide and reduced graphene oxide in Pseudomonas aeruginosa. *International Journal of Nanomedicine*, *7*, 5901–5914.

https://doi.org/10.2147/IJN.S37397

Han, D., Yan, L., Chen, W., & Li, W. (2011). Preparation of chitosan/graphene oxide composite film with enhanced mechanical strength in the wet state. *Carbohydrate Polymers*, *83*(2), 653–658. https://doi.org/10.1016/j.carbpol.2010.08.038

Han, Z. J., Rider, A. E., Fisher, C., van der Laan, T., Kumar, S., Levchenko, I., & Ostrikov, K. (Ken). (2014). Carbon Nanotubes and Graphene. In *Carbon Nanotubes and Graphene*. https://doi.org/10.1016/B978-0-08-098232-8.00012-7

Hassan, F. M., Batmaz, R., Li, J., Wang, X., Xiao, X., Yu, A., & Chen, Z. (2015). Evidence of covalent synergy in silicon–sulfur–graphene yielding highly efficient and long-life lithium-ion batteries. *Nature Communications*, *6*(1), 8597. https://doi.org/10.1038/ncomms9597

He, H., Li, X., Wang, J., Qiu, T., Fang, Y., Song, Q., Zhi, L. (2013). Reduced graphene oxide nanoribbon networks: a novel approach towards scalable fabrication of transparent conductive films. *Small (Weinheim an Der Bergstrasse, Germany)*, *9*(6), 820–824. https://doi.org/10.1002/smll.201201918

Hong, X., Mahalingam, S., Edirisinghe, M., (2017). *Simultaneous Application of Pressure-Infusion-Gyration to Generate Polymeric Nanofibers*. https://doi.org/10.1002/mame.201600564

Huang, J., Cao, Y., Huang, Z., Imbraguglio, S. A., Wang, Z., Peng, X., & Guo, Z. (2016). Comparatively Thermal and Crystalline Study of Poly(methyl-methacrylate)/Polyacrylonitrile Hybrids: Core-Shell Hollow Fibers, Porous Fibers, and Thin Films. *Macromolecular Materials and Engineering*, *301*(11), 1327–1336. https://doi.org/10.1002/mame.201600172

Huang, X. (2009). Fabrication and Properties of Carbon Fibers. *Materials*, *2*(4),

2369–2403. https://doi.org/10.3390/ma2042369

Huang, Z. M., Zhang, Y. Z., Kotaki, M., & Ramakrishna, S. (2003). A review on polymer nanofibers by electrospinning and their applications in nanocomposites. *Composites Science and Technology*, *63*, 2223–2253. https://doi.org/10.1016/S0266-3538(03)00178-7

Iijima, S. (1991). Helical microtubules of graphitic carbon. *Nature*, *354*(6348), 56–58. https://doi.org/10.1038/354056a0

Illangakoon, U. E., Mahalingam, S., Colombo, P., & Edirisinghe, M. (2016). Tailoring the surface of polymeric nanofibres generated by pressurised gyration. *Surface Innovations*, *4*(3), 167–178. https://doi.org/10.1680/jsuin.16.00007

Illangakoon, U., Mahalingam, S., Matharu, R., Edirisinghe, M., (2017). Evolution of Surface Nanopores in Pressurised Gyrospun Polymeric Microfibers. *Polymers*, *9*(12), 508. https://doi.org/10.3390/polym9100508

Jang, J. (2006). Emissive Materials Nanomaterials. In *Advances in Polymer Science*. https://doi.org/10.1007/11611967

Jayasinghe, S. N., & Suter, N. (2010). Pressure driven spinning: A multifaceted approach for preparing nanoscaled functionalized fibers, scaffolds, and membranes with advanced materials. *Biomicrofluidics*, *4*(1), 14106. https://doi.org/10.1063/1.3328092

Jesus de La Fuente. (2013). Graphene Applications & Uses – Graphenea. Retrieved November 29, 2018, from https://www.azonano.com/article.aspx?ArticleID=3492 website: https://www.graphenea.com/pages/graphene-uses-applications#.W_8MwC2ca8p

Jiao, T., Guo, H., Zhang, Q., Peng, Q., Tang, Y., Yan, X., Munstedt, H. (2015).

Reduced Graphene Oxide-Based Silver Nanoparticle-Containing Composite Hydrogel as Highly Efficient Dye Catalysts for Wastewater Treatment. *Scientific Reports*, *5*, 11873. https://doi.org/10.1038/srep11873

Jing, X., Mi, H.-Y., Salick, M. R., Peng, X.-F., & Turng, L.-S. (2014). Preparation of thermoplastic polyurethane/graphene oxide composite scaffolds by thermally induced phase separation. *Polymer Composites*, *35*(7), 1408–1417. https://doi.org/10.1002/pc.22793

Jung, I., Field, D. A., Clark, N. J., Zhu, Y., Yang, D., Piner, R. D., Ruoff, R. S. (2009). Reduction Kinetics of Graphene Oxide Determined by Electrical Transport Measurements and Temperature Programmed Desorption. *The Journal of Physical Chemistry C*, *113*(43), 18480–18486. https://doi.org/10.1021/jp904396j

Kamibayashi, M., Ogura, H., & Otsubo, Y. (2006). Rheological behavior of suspensions of silica nanoparticles in associating polymer solutions. *Industrial and Engineering Chemistry Research*, *45*(21), 6899–6905. https://doi.org/10.1021/ie0512486

Kanamori, Y., Obata, S., & Saiki, K. (2011). *Conductive Atomic Force Microscopy of Chemically Synthesized Graphene Oxide and Interlayer Conduction*. https://doi.org/10.1246/cl.2011.255

Khudyakov, I. V., Zopf, D. R., & Turro, N. J. (2009). Polyurethane Nanocomposites. *Designed Monomers and Polymers*, *12*(4), 279–290. https://doi.org/10.1163/156855509X448253

Kim, B.-H., Yang, K. S., & Ferraris, J. P. (2012). Highly conductive, mesoporous carbon nanofiber web as electrode material for high-performance supercapacitors. *Electrochimica Acta*, *75*, 325–331. https://doi.org/10.1016/j.electacta.2012.05.004

Kim, J. C., Rahman, M. M., Ju, M. J., & Lee, J.-J. (2018). *Highly conductive and stable graphene/PEDOT:PSS composite as a metal free cathode for organic dye-sensitized solar cells*. https://doi.org/10.1039/c8ra02668h

Knight, D. S., & White, W. B. (1989). Characterization of diamond films by Raman spectroscopy. *Journal of Materials Research*, *4*(02), 385–393. https://doi.org/10.1557/JMR.1989.0385

Kong, K., Deng, L., Kinloch, I. A., Young, R. J., & Eichhorn, S. J. (2012). Production of carbon fibres from a pyrolysed and graphitised liquid crystalline cellulose fibre precursor. *Journal of Materials Science*, *47*(14), 5402–5410. https://doi.org/10.1007/s10853-012-6426-y

Konwer, S., Guha, A. K., & Dolui, S. K. (2013). Graphene oxide-filled conducting polyaniline composites as methanol-sensing materials. *Journal of Materials Science*, *48*(4), 1729–1739. https://doi.org/10.1007/s10853-012-6931-z

Kralchevskyt, P. A., & Nagayama', K. (1994). Capillary Forces between Colloidal Particles. In *Langmuir* (Vol. 10). Retrieved from https://www.dce.uni-sofia.bg/files/publications/1994/1994-04-PK.pdf

Kudin, K. N., Ozbas, B., Schniepp, H. C., Prud'homme, R. K., Aksay, I. A., & Car, R. (2008). Raman spectra of graphite oxide and functionalized graphene sheets. *Nano Letters*, *8*(1), 36–41. https://doi.org/10.1021/nl071822y

Lee, J., Yoon, S., Hyeon, T., Oh, S. M., & Kim, K. B. (1999). Synthesis of a new mesoporous carbon and its application to electrochemical double-layer capacitors. *Chem. Commun.,* 2177-2178. https://doi.org/10.1039/A906872D

Li, M., Song, H., Chen, X., Zhou, J., & Ma, Z. (2015). Phenolic resin-grafted reduced graphene oxide as a highly stable anode material for lithium ion

batteries. *Physical Chemistry Chemical Physics : PCCP*, *17*(5), 3250–3260. https://doi.org/10.1039/c4cp04556d

Li, X., Liu, Z., Wang, B., Yang, J., Ma, Y., Feng, X., Gu, M. (2013). Chemical vapor deposition of amorphous graphene on ZnO film. *Synthetic Metals*, *174*, 50–53. https://doi.org/10.1016/j.synthmet.2013.04.020

Lin, L.-C., & Grossman, J. C. (2015). Atomistic understandings of reduced graphene oxide as an ultrathin-film nanoporous membrane for separations. *Nature Communications*, *6*, 8335. https://doi.org/10.1038/ncomms9335

Liu, F., Qin, B., He, L., & Song, R. (2009). Novel starch/chitosan blending membrane: Antibacterial, permeable and mechanical properties. *Carbohydrate Polymers*, *78*(1), 146–150. https://doi.org/10.1016/j.carbpol.2009.03.021

Liu, S., Zeng, T. H., Hofmann, M., Burcombe, E., Wei, J., Jiang, R., Chen, Y. (2011). Antibacterial activity of graphite, graphite oxide, graphene oxide, and reduced graphene oxide: membrane and oxidative stress. *ACS Nano*, *5*(9), 6971–6980. https://doi.org/10.1021/nn202451x

Liu, Y.-L., Chen, W.-H., & Chang, Y.-H. (2009). Preparation and properties of chitosan/carbon nanotube nanocomposites using poly(styrene sulfonic acid)-modified CNTs. *Carbohydrate Polymers*, *76*(2), 232–238. https://doi.org/10.1016/j.carbpol.2008.10.021

Lu, B., Li, T., Zhao, H., Li, X., Gao, C., Zhang, S., & Xie, E. (2012). Graphene-based composite materials beneficial to wound healing. *Nanoscale*, *4*(9), 2978. https://doi.org/10.1039/c2nr11958g

Luo, C. J., Nangrejo, M., & Edirisinghe, M. (2010). A novel method of selecting solvents for polymer electrospinning. *Polymer*, *51*(7), 1654–1662. https://doi.org/10.1016/j.polymer.2010.01.031

Luo, C. J., Stride, E., Stoyanov, S., Pelan, E., & Edirisinghe, M. (2011). Electrospinning short polymer micro-fibres with average aspect ratios in the range of 10–200. *Journal of Polymer Research*, *18*(6), 2515–2522. https://doi.org/10.1007/s10965-011-9667-6

Mahalingam, S., & Edirisinghe, M. (2013). Forming of polymer nanofibers by a pressurised gyration process. *Macromolecular Rapid Communications*, *34*(14), 1134–1139. https://doi.org/10.1002/marc.201300339

Mahalingam, S., Raimi-Abraham, B. T., Craig, D. Q. M., & Edirisinghe, M. (2015a). Formation of protein and protein-gold nanoparticle stabilized microbubbles by pressurized gyration. *Langmuir : The ACS Journal of Surfaces and Colloids*, *31*(2), 659–666. https://doi.org/10.1021/la502181g

Mahalingam, S., Raimi-Abraham, B. T., Craig, D. Q. M., & Edirisinghe, M. (2015b). Solubility–spinnability map and model for the preparation of fibres of polyethylene (terephthalate) using gyration and pressure. *Chemical Engineering Journal*, *280*, 344–353. https://doi.org/10.1016/j.cej.2015.05.114

Mahalingam, S., Ren, G. G., & Edirisinghe, M. J. (2014). Rheology and pressurised gyration of starch and starch-loaded poly(ethylene oxide). *Carbohydrate Polymers*, *114*, 279–287. https://doi.org/10.1016/j.carbpol.2014.08.007

Mallet-Ladeira, P., Puech, P., Toulouse, C., Cazayous, M., Ratel-Ramond, N., Weisbecker, P., Monthioux, M. (2014). A Raman study to obtain crystallite size of carbon materials: A better alternative to the Tuinstra–Koenig law. *Carbon*, *80*, 629–639. https://doi.org/10.1016/j.carbon.2014.09.006

Manickam, S. S., Karra, U., Huang, L., Bui, N.-N., Li, B., & Mccutcheon, J. R. (2013). *Activated carbon nanofiber anodes for microbial fuel cells*. https://doi.org/10.1016/j.carbon.2012.10.009

Martinez, U., Dumont, J. H., Holby, E. F., Artyushkova, K., Purdy, G. M., Singh, A., Gupta, G. (2016). Critical role of intercalated water for electrocatalytically active nitrogen-doped graphitic systems. *Science Advances*, *2*(3), e1501178. https://doi.org/10.1126/sciadv.1501178

Matharu, R. K., Porwal, H., Ciric, L., & Edirisinghe, M. (2018). The effect of graphene–poly(methyl methacrylate) fibres on microbial growth. *Interface Focus*, *8*(3), 20170058. https://doi.org/10.1098/rsfs.2017.0058

Matsumoto, H., Imaizumi, S., Konosu, Y., Ashizawa, M., Minagawa, M., Tanioka, A., Tour, J. M. (2013). Electrospun composite nanofiber yarns containing oriented graphene nanoribbons. *ACS Applied Materials and Interfaces*, *5*, 6225–6231. https://doi.org/10.1021/am401161b

Matsumoto, M., Hashimoto, T., Uchiyama, Y., Murata, K., & Goto, S. (1993). Use of modified carbon whiskers as an electrode in coulometric cells. *Carbon*, *31*(6), 1003–1004. https://doi.org/10.1016/0008-6223(93)90208-R

Mattevi, C., Eda, G., Agnoli, S., Miller, S., Mkhoyan, K. A., Celik, O., Chhowalla, M. (2009). Evolution of Electrical, Chemical, and Structural Properties of Transparent and Conducting Chemically Derived Graphene Thin Films. *Advanced Functional Materials*, *19*(16), 2577–2583. https://doi.org/10.1002/adfm.200900166

Mazumder, M. K., Chang, R. J., & Bond, R. L. (1982). Aerodynamic and Morphological Properties of Carbon-Fiber Aerosols. *Aerosol Science and Technology*, *1*(4), 427–440. https://doi.org/10.1080/02786828208958606

McCann, J. T., Marquez, Manuel, & Xia, Younan. (2006). Highly Porous Fibers by Electrospinning into a Cryogenic Liquid. *J. Am. Chem. Soc.*, 128 (5), pp 1436–1437 https://doi.org/10.1021/JA056810Y

Medeiros, E. S., Glenn, G. M., Klamczynski, A. P., Orts, W. J., & Mattoso, L.

H. C. (2009). Solution blow spinning: A new method to produce micro- and nanofibers from polymer solutions. *Journal of Applied Polymer Science*, *113*(4), 2322–2330. https://doi.org/10.1002/app.30275

Meng, F., Lu, W., Li, Q., Byun, J.-H., Oh, Y., & Chou, T.-W. (2015). Graphene-Based Fibers: A Review. *Advanced Materials*, *27*(35), 5113–5131. https://doi.org/10.1002/adma.201501126

Mingxi, W., Inagaki, M., Kang, F., Huang, Z.-H., & Bai, Y. (2013). Porous Carbon Nanofibers: Preparation and Potential Applications. *Current Organic Chemistry*, *17*(13), 1434–1447. https://doi.org/10.2174/1385272811317130010

Mkhoyan, K. A., Contryman, A. W., Silcox, J., Stewart, D. A., Eda, G., Mattevi, C., Chhowalla, M. (2009). Atomic and Electronic Structure of Graphene-Oxide. *Nano Letters*, *9*(3), 1058–1063. https://doi.org/10.1021/nl8034256

Modak, P., Kondawar, S. B., & Nandanwar, D. V. (2015). Synthesis and Characterization of Conducting Polyaniline/Graphene Nanocomposites for Electromagnetic Interference Shielding. *Procedia Materials Science*, *10*(Cnt 2014), 588–594. https://doi.org/10.1016/j.mspro.2015.06.010

Mohamadzadeh Moghadam, M. H., Sabury, S., Gudarzi, M. M., & Sharif, F. (2014). Graphene oxide-induced polymerization and crystallization to produce highly conductive polyaniline/graphene oxide composite. *Journal of Polymer Science Part A: Polymer Chemistry*, *52*(11), 1545–1554. https://doi.org/10.1002/pola.27147

Morariu, M. D., Voicu, N. E., Schäffer, E., Lin, Z., Russell, T. P., & Steiner, U. (2003). Hierarchical structure formation and pattern replication induced by an electric field. *Nature Materials*, *2*(1), 48–52. https://doi.org/10.1038/nmat789

Munz, M., Giusca, C. E., Myers-Ward, R. L., Gaskill, D. K., & Kazakova, O.

(2015). Thickness-Dependent Hydrophobicity of Epitaxial Graphene. *ACS Nano*, *9*(8), 8401–8411. https://doi.org/10.1021/acsnano.5b03220

Navarro-Pardo, F., Martinez-Hernandez, A. L., & Velasco-Santos, C. (2016). Carbon Nanotube and Graphene Based Polyamide Electrospun Nanocomposites: A Review. *Journal of Nanomaterials*, *2016*, 1–16. https://doi.org/10.1155/2016/3182761

Novoselov, K. S., Fal'ko, V. I., Colombo, L., Gellert, P. R., Schwab, M. G., & Kim, K. (2012). A roadmap for graphene. *Nature*, *490*(7419), 192–200. https://doi.org/10.1038/nature11458

Novoselov, K. S., Geim, A. K., Morozov, S. V, Jiang, D., Zhang, Y., Dubonos, S. V, Firsov, A. A. (2004). Electric field effect in atomically thin carbon films. *Science (New York, N.Y.)*, *306*(5696), 666–669. https://doi.org/10.1126/science.1102896

Padron, S., Fuentes, A., Caruntu, D., & Lozano, K. (2013). Experimental study of nanofiber production through forcespinning. *Journal of Applied Physics*, *113*(2), 024318. https://doi.org/10.1063/1.4769886

Pal, J., Kankariya, N., Sanwaria, S., Nandan, B., & Srivastava, R. K. (2013). Control on molecular weight reduction of poly(ε-caprolactone) during melt spinning--a way to produce high strength biodegradable fibers. *Materials Science & Engineering. C, Materials for Biological Applications*, *33*(7), 4213–4220. https://doi.org/10.1016/j.msec.2013.06.011

Pàmies, P. (2014). Defective yet strong. *Nature Materials*, *13*(3), 223–223. https://doi.org/10.1038/nmat3906

Pandele, A. M., Ionita, M., Lungu, A., Vasile, E., Zaharia, C., & Iovu, H. (2015). Porous chitosan/graphene oxide biocomposites for tissue engineering. *Polymer Composites*, 363–370. https://doi.org/10.1002/pc.23594

Pang, H., Chen, T., Zhang, G., Zeng, B., & Li, Z.-M. (2010). An electrically conducting polymer/graphene composite with a very low percolation threshold. *Materials Letters*, *64*(20), 2226–2229. https://doi.org/10.1016/j.matlet.2010.07.001

Park, S. J., & Heo, G. Y. (2015). Precursors and manufacturing of carbon fibers. *Springer Series in Materials Science*, *210*, 31–66. https://doi.org/10.1007/978-94-017-9478-7_2

Park, S., & Ruoff, R. S. (2009). Chemical methods for the production of graphenes. *Nature Nanotechnology*, *4*(4), 217–224. https://doi.org/10.1038/nnano.2009.58

Pei, S., & Cheng, H.-M. (2012). The reduction of graphene oxide. *Carbon*, *50*(9), 3210–3228. https://doi.org/10.1016/j.carbon.2011.11.010

Peng, S., Shao, H., & Hu, X. (2003). Lyocell fibers as the precursor of carbon fibers. *Journal of Applied Polymer Science*, *90*(7), 1941–1947. https://doi.org/10.1002/app.12879

Pham-Huu, C., Keller, N., Ledoux, M. J., Charbonniere, L. J., & Ziessel, R. (2000). Carbon nanofiber supported palladium catalyst for liquid-phase reactions. An active and selective catalyst for hydrogenation of C=C bonds. *Chemical Communications*, *0*(19), 1871–1872. https://doi.org/10.1039/b005306f

Pluta, M. (2006). Melt compounding of polylactide/organoclay: Structure and properties of nanocomposites. *Journal of Polymer Science Part B: Polymer Physics*, *44*(23), 3392–3405. https://doi.org/10.1002/polb.20957

Porwal, H., Tatarko, P., Saggar, R., Grasso, S., Kumar Mani, M., Dlouhý, I., Reece, M. J. (2014). Tribological properties of silica–graphene nano-platelet composites. *Ceramics International*, *40*(8), 12067–12074. https://doi.org/10.1016/j.ceramint.2014.04.046

Potts, J. R., Dreyer, D. R., Bielawski, C. W., & Ruoff, R. S. (2011). Graphene-based polymer nanocomposites. *Polymer*, *52*(1), 5–25. https://doi.org/10.1016/j.polymer.2010.11.042

Prachi Patel. (2008). Graphene-Polymer Composite. *Intelligent Machines, MIT Technology Review.* Retrieved December 4, 2018, from https://www.technologyreview.com/s/410181/graphene-polymer-composite/

Prado, A. R., Leal-Junior, A. G., Marques, C., Leite, S., de Sena, G. L., Machado, L. C., Pontes, M. J. (2017). Polymethyl methacrylate (PMMA) recycling for the production of optical fiber sensor systems. *Optics Express*, *25*(24), 30051. https://doi.org/10.1364/OE.25.030051

Qi, Z., Yu, H., Chen, Y., & Zhu, M. (2009). Highly porous fibers prepared by electrospinning a ternary system of nonsolvent/solvent/poly(l-lactic acid). *Materials Letters*, *63*(3–4), 415–418. https://doi.org/10.1016/J.MATLET.2008.10.059

Rahaman, M. S. A., Ismail, A. F., & Mustafa, A. (2007). A review of heat treatment on polyacrylonitrile fiber. *Polymer Degradation and Stability*, *92*(8), 1421–1432. https://doi.org/10.1016/j.polymdegradstab.2007.03.023

Ramos, M. E., Bonelli, P. R., Cukierman, A. L., Ribeiro Carrott, M. M. L., & Carrott, P. J. M. (2010). Adsorption of volatile organic compounds onto activated carbon cloths derived from a novel regenerated cellulosic precursor. *Journal of Hazardous Materials*, *177*(1–3), 175–182. https://doi.org/10.1016/j.jhazmat.2009.12.014

Reneker, D. H., Yarin, A. L., Fong, H., & Koombhongse, S. (2000). Bending instability of electrically charged liquid jets of polymer solutions in electrospinning. *Journal of Applied Physics*, *87*(9 I), 4531–4547. Retrieved

from http://www.scopus.com/inward/record.url?eid=2-s2.0-0009774721&partnerID=tZOtx3y1

Rodriguez, N. M. (1993). A review of catalytically grown carbon nanofibers. *Journal of Materials Research*, *8*(12), 3233–3250. https://doi.org/10.1557/JMR.1993.3233

Rubino, S., Akhtar, S., & Leifer, K. (2016). A Simple Transmission Electron Microscopy Method for Fast Thickness Characterization of Suspended Graphene and Graphite Flakes. *Microscopy and Microanalysis*, *22*(01), 250–256. https://doi.org/10.1017/S143192761501569X

Saito, R., Jorio, A., Souza Filho, A. G., Dresselhaus, G., Dresselhaus, M. S., & Pimenta, M. A. (2002). Probing phonon dispersion relations of graphite by double resonance Raman scattering. *Physical Review Letters*, *88*(2), 027401. https://doi.org/10.1103/PhysRevLett.88.027401

Schönfelder, R., Avilés, F., Knupfer, M., Azamar-Barrios, J. A., González-Chi, P. I., & Rümmeli, M. H. (2014). Influence of architecture on the Raman spectra of acid-treated carbon nanostructures. *Journal of Experimental Nanoscience*, *9*(9), 931–941. https://doi.org/10.1080/17458080.2012.750763

Sengupta, R., Bhattacharya, M., Bandyopadhyay, S., & Bhowmick, A. K. (2011). A review on the mechanical and electrical properties of graphite and modified graphite reinforced polymer composites. *Progress in Polymer Science*, *36*(5), 638–670. https://doi.org/10.1016/j.progpolymsci.2010.11.003

Shao, W., Liu, X., Min, H., Dong, G., Feng, Q., & Zuo, S. (2015). Preparation, Characterization, and Antibacterial Activity of Silver Nanoparticle-Decorated Graphene Oxide Nanocomposite. *ACS Applied Materials & Interfaces*, *7*(12), 6966–6973. https://doi.org/10.1021/acsami.5b00937

Soltani-Kordshuli, F., Zabihi, F., & Eslamian, M. (2016). Graphene-doped PEDOT:PSS nanocomposite thin films fabricated by conventional and substrate vibration-assisted spray coating (SVASC). *Engineering Science and Technology, an International Journal*, *19*(3), 1216–1223. https://doi.org/10.1016/J.JESTCH.2016.02.003

Song, P., Cao, Z., Cai, Y., Zhao, L., Fang, Z., & Fu, S. (2011). Fabrication of exfoliated graphene-based polypropylene nanocomposites with enhanced mechanical and thermal properties. *Polymer*, *52*(18), 4001–4010. https://doi.org/10.1016/j.polymer.2011.06.045

Spencer, J. N., & Hovick, J. W. (1988). Solvation of urea and methyl-substituted ureas by water and DMF. *Can. J. Chem* (Vol. 66).

Stankovich, S., Dikin, D. A., Piner, R. D., Kohlhaas, K. A., Kleinhammes, A., Jia, Y., Ruoff, R. S. (2007). Synthesis of graphene-based nanosheets via chemical reduction of exfoliated graphite oxide. *Carbon*, *45*(7), 1558–1565. https://doi.org/10.1016/j.carbon.2007.02.034

Stashak, T. S., Farstvedt, E., & Othic, A. (2004). Update on wound dressings: Indications and best use. *Clinical Techniques in Equine Practice*, *3*(2), 148–163. https://doi.org/10.1053/j.ctep.2004.08.006

Suzuki, K., Matsumoto, H., Minagawa, M., Kimura, M., & Tanioka, A. (2007). Preparation of Carbon Fiber Fabrics from Phenolic Resin by Electrospray Deposition. *Polymer Journal*, *39*(11), 1128–1134. https://doi.org/10.1295/polymj.PJ2007091

Tabish, T., Pranjol, M., Horsell, D., Rahat, A., Whatmore, J., Winyard, P., Zhang, S. (2019). Graphene Oxide-Based Targeting of Extracellular Cathepsin D and Cathepsin L As A Novel Anti-Metastatic Enzyme Cancer Therapy. *Cancers*, *11*(3), 319. https://doi.org/10.3390/cancers11030319

Tang, C., Xiang, L., Su, J., Wang, K., Yang, C., Zhang, Q., & Fu, Q. (2008).

Largely Improved Tensile Properties of Chitosan Film via Unique Synergistic Reinforcing Effect of Carbon Nanotube and Clay. *The Journal of Physical Chemistry B*, *112*(13), 3876–3881. https://doi.org/10.1021/jp709977m

Tian, Z., Xu, C., Li, J., Zhu, G., Shi, Z., & Lin, Y. (2013). Self-Assembled Free-Standing Graphene Oxide Fibers. *ACS Applied Materials & Interfaces*, *5*(4), 1489–1493. https://doi.org/10.1021/am303010j

Tuinstra, F., & Koenig, J. L. (1970). Raman Spectrum of Graphite. *The Journal of Chemical Physics*, *53*(3), 1126–1130. https://doi.org/10.1063/1.1674108

Tzeng, Y.-R., Pai, W. W., Tsao, C.-S., & Yu, M.-S. (2011). Adsorption of Single Platinum Atom on the Graphene Oxide: The Role of the Carbon Lattice. *The Journal of Physical Chemistry C*, *115*(24), 12023–12032. https://doi.org/10.1021/jp200280t

Utracki, L. A., Sepehr, M., & Li, J. (2006). Melt compounding of polymeric nanocomposites. *International Polymer Processing*. https://doi.org/10.3139/217.0093

Wang, J., & Joseph, D. D. (2003). Particle-laden tubeless siphon. *Journal of Fluid Mechanics*, 480, 119-128. https://doi.org/10.1017/S0022112003003793

Wang, L., Zhang, L., & Tian, M. (2012). Improved polyvinylpyrrolidone (PVP)/graphite nanocomposites by solution compounding and spray drying. *Polymers for Advanced Technologies*, *23*(3), 652–659. https://doi.org/10.1002/pat.1940

Weise, B., Völkel, L., Köppe, G., Schriever, S., Mroszczok, J., Köhler, J., Seide, G. (2017). Melt- and Wet-Spinning of Graphene-Polymer Nano-Composite Fibres for Multifunctional Textile Applications. *Materials*

Today: Proceedings, *4*, S135–S145. https://doi.org/10.1016/j.matpr.2017.09.178

Weitz, R. T., Harnau, L., Rauschenbach, S., Burghard, M., & Kern, K. (2008). Polymer nanofibers via nozzle-free centrifugal spinning. *Nano Letters*, *8*(4), 1187–1191. https://doi.org/10.1021/nl080124q

Wu, D., Zhang, F., Liang, H., & Feng, X. (2012). Nanocomposites and macroscopic materials: assembly of chemically modified graphene sheets. *Chemical Society Reviews*, *41*(18), 6160–6177. https://doi.org/10.1039/c2cs35179j

Wu, X., Mahalingam, S., VanOosten, S. K., Wisdom, C., Tamerler, C., & Edirisinghe, M. (2017). New Generation of Tunable Bioactive Shape Memory Mats Integrated with Genetically Engineered Proteins. *Macromolecular Bioscience*, *17*(2), 1600270. https://doi.org/10.1002/mabi.201600270

Xiang, C., Behabtu, N., Liu, Y., Chae, H. G., Young, C. C., Genorio, B., Tour, J. M. (2013). Graphene Nanoribbons as an Advanced Precursor for Making Carbon Fiber. *ACS Nano*, *7*(2), 1628–1637. https://doi.org/10.1021/nn305506s

Xiang, C., Young, C. C., Wang, X., Yan, Z., Hwang, C.-C., Cerioti, G., Tour, J. M. (2013). Large flake graphene oxide fibers with unconventional 100% knot efficiency and highly aligned small flake graphene oxide fibers. *Advanced Materials (Deerfield Beach, Fla.)*, *25*(33), 4592–4597. https://doi.org/10.1002/adma.201301065

Xu, Y., Bai, H., Lu, G., Li, C., & Shi, G. (2008). Flexible graphene films via the filtration of water-soluble noncovalent functionalized graphene sheets. *Journal of the American Chemical Society*, *130*(18), 5856–5857. https://doi.org/10.1021/ja800745y

Xu, Z., & Gao, C. (2011). Graphene chiral liquid crystals and macroscopic assembled fibres. *Nature Communications*, *2*, 571. https://doi.org/10.1038/ncomms1583

Xu, Z., & Gao, C. (2015). Graphene fiber: a new trend in carbon fibers. *Materials Today*, *18*(9), 480–492. https://doi.org/10.1016/J.MATTOD.2015.06.009

Xu, Z., Mahalingam, S., Rohn, J. L., Ren, G., & Edirisinghe, M. (2015). Physio-chemical and antibacterial characteristics of pressure spun nylon nanofibres embedded with functional silver nanoparticles. *Materials Science and Engineering: C*, *56*, 195–204. https://doi.org/10.1016/j.msec.2015.06.003

Xu, Z., Sun, H., Zhao, X., & Gao, C. (2013). Ultrastrong fibers assembled from giant graphene oxide sheets. *Advanced Materials (Deerfield Beach, Fla.)*, *25*(2), 188–193. https://doi.org/10.1002/adma.201203448

Yan, Q.-L., Gozin, M., Zhao, F.-Q., Cohen, A., & Pang, S.-P. (2016). Highly energetic compositions based on functionalized carbon nanomaterials. *Nanoscale*, *8*, 4799. https://doi.org/10.1039/c5nr07855e

Yang, W., Ratinac, K. R., Ringer, S. P., Thordarson, P., Gooding, J. J., & Braet, F. (2010). Carbon nanomaterials in biosensors: should you use nanotubes or graphene? *Angewandte Chemie (International Ed. in English)*, *49*(12), 2114–2138. https://doi.org/10.1002/anie.200903463

Yang, W., Thordarson, P., Gooding, J. J., Ringer, S. P., & Braet, F. (2007). Carbon nanotubes for biological and biomedical applications. *Nanotechnology*, *18*(41), 412001. https://doi.org/10.1088/0957-4484/18/41/412001

Yang, X., Tu, Y., Li, L., Shang, S., & Tao, X. (2010). Well-Dispersed Chitosan/Graphene Oxide Nanocomposites. *ACS Applied Materials &*

Interfaces, *2*(6), 1707–1713. https://doi.org/10.1021/am100222m

Yu, P., Li, Y., Zhao, X., Wu, L., & Zhang, Q. (2014). Graphene-wrapped polyaniline nanowire arrays on nitrogen-doped carbon fabric as novel flexible hybrid electrode materials for high-performance supercapacitor. *Langmuir : The ACS Journal of Surfaces and Colloids*, *30*(18), 5306–5313. https://doi.org/10.1021/la404765z

Yuan, D., Pedrazzoli, D., Pircheraghi, G., & Manas-Zloczower, I. (2017a). Melt Compounding of Thermoplastic Polyurethanes Incorporating 1D and 2D Carbon Nanofillers. *Polymer-Plastics Technology and Engineering*, *56*(7), 732–743. https://doi.org/10.1080/03602559.2016.1233265

Yuan, D., Pedrazzoli, D., Pircheraghi, G., & Manas-Zloczower, I. (2017b). Melt Compounding of Thermoplastic Polyurethanes Incorporating 1D and 2D Carbon Nanofillers. *Polymer-Plastics Technology and Engineering*, *56*(7), 732–743. https://doi.org/10.1080/03602559.2016.1233265

Yuan Gao, Y., & Cranston, R. (2008). Recent Advances in Antimicrobial Treatments of Textiles. *Textile Research Journal*, *78*(1), 60–72. https://doi.org/10.1177/0040517507082332

Yue-Ying Fan, Feng Li, Hui-Ming Cheng, Ge Su, Ying-Da Yu, Z.-H. S. (1998). Preparation, morphology, and microstructure of diameter-controllable vapor-grown carbon nanofibers. *Journal of Materials Research*, *13*(8), 2342–2346.

Zamora-Ledezma, C., Puech, N., Zakri, C., Grelet, E., Moulton, S. E., Wallace, G. G., Poulin, P. (2012). Liquid Crystallinity and Dimensions of Surfactant-Stabilized Sheets of Reduced Graphene Oxide. *The Journal of Physical Chemistry Letters*, *3*(17), 2425–2430. https://doi.org/10.1021/jz3008479

Zander, N. E. (2015). Formation of melt and solution spun polycaprolactone fibers by centrifugal spinning. *Journal of Applied Polymer Science*, *132*(2),

n/a-n/a. https://doi.org/10.1002/app.41269

Zhang, J., & Zhao, X. S. (2012). Conducting Polymers Directly Coated on Reduced Graphene Oxide Sheets as High-Performance Supercapacitor Electrodes. *The Journal of Physical Chemistry C*, *116*(9), 5420–5426. https://doi.org/10.1021/jp211474e

Zhang, S., Karaca, B. T., VanOosten, S. K., Yuca, E., Mahalingam, S., Edirisinghe, M., & Tamerler, C. (2015). Coupling Infusion and Gyration for the Nanoscale Assembly of Functional Polymer Nanofibers Integrated with Genetically Engineered Proteins. *Macromolecular Rapid Communications*, *36*(14), 1322–1328. https://doi.org/10.1002/marc.201500174

Zhang, Y., Li, J., An, G., & He, X. (2010). Highly porous SnO_2 fibers by electrospinning and oxygen plasma etching and its ethanol-sensing properties. *Sensors and Actuators B: Chemical*, *144*(1), 43–48. https://doi.org/10.1016/J.SNB.2009.10.012

Zheng, W., Wong, S.-C., & Sue, H.-J. (2002). Transport behavior of PMMA/expanded graphite nanocomposites. *Polymer*, *43*(25), 6767–6773. https://doi.org/10.1016/S0032-3861(02)00599-2

Zheng Yan, A. R. B. (2014). *Characterization of Graphene by Raman Spectroscopy - Nanomaterials and Nanotechnology - OpenStax CNX*. Retrieved from Andrew R. Barron website: https://cnx.org/contents/e038-LKO@13.5:8GImxcKk@2/Characterization-of-Graphene-by-Raman-Spectroscopy

Zhou, F. L., Gong, R. H., & Porat, I. (2009). Mass production of nanofibre assemblies: By electrostatic spinning. *Polymer International*, *58*(4), 331–342. https://doi.org/10.1002/pi.2521

Zhou, S., Zhang, H., Wang, X., Li, J., & Wang, F. (2013). Sandwich

nanocomposites of polyaniline embedded between graphene layers and multi-walled carbon nanotubes for cycle-stable electrode materials of organic supercapacitors. *RSC Adv.*, *3*(6), 1797–1807. https://doi.org/10.1039/C2RA22323F

Zhu, H., Zhang, C., Tang, Y., Wang, J., Ren, B., & Yin, Y. (2007). Preparation and thermal conductivity of suspensions of graphite nanoparticles. *Carbon*, Vol. 45, pp. 226–228. https://doi.org/10.1016/j.carbon.2006.07.005

Zhuang, X., Yang, X., Shi, L., Cheng, B., Guan, K., & Kang, W. (2012). Solution blowing of submicron-scale cellulose fibers. *Carbohydrate Polymers*, *90*(2), 982–987. https://doi.org/10.1016/j.carbpol.2012.06.031

Zupančič, Š., Sinha-Ray, S., Sinha-Ray, S., Kristl, J., & Yarin, A. L. (2016). Long-Term Sustained Ciprofloxacin Release from PMMA and Hydrophilic Polymer Blended Nanofibers. *Molecular Pharmaceutics*, *13*(1), 295–305. https://doi.org/10.1021/acs.molpharmaceut.5b00804